TU Delft

Delft University of Technology

Gate-based readout of hybrid quantum dot systems

de Jong, D.

DOI
10.4233/uuid:9cd36947-5e27-4436-9bbb-d7fc5daa6047

Publication date
2021

Document Version
Final published version

Citation (APA)
de Jong, D. (2021). *Gate-based readout of hybrid quantum dot systems*. [Dissertation (TU Delft), Delft University of Technology]. https://doi.org/10.4233/uuid:9cd36947-5e27-4436-9bbb-d7fc5daa6047

Important note
To cite this publication, please use the final published version (if applicable).
Please check the document version above.

Copyright
Other than for strictly personal use, it is not permitted to download, forward or distribute the text or part of it, without the consent of the author(s) and/or copyright holder(s), unless the work is under an open content license such as Creative Commons.

Takedown policy
Please contact us and provide details if you believe this document breaches copyrights.
We will remove access to the work immediately and investigate your claim.

This work is downloaded from Delft University of Technology.
For technical reasons the number of authors shown on this cover page is limited to a maximum of 10.

GATE-BASED READOUT OF HYBRID QUANTUM DOT SYSTEMS

GATE-BASED READOUT OF HYBRID QUANTUM DOT SYSTEMS

Proefschrift

ter verkrijging van de graad van doctor
aan de Technische Universiteit Delft,
op gezag van de Rector Magnificus prof. dr. ir. T.H.J.J. van der Hagen,
voorzitter van het College voor Promoties,
in het openbaar te verdedigen op donderdag 25 november 2021 om 15:00 uur

door

Damaz DE JONG

Master of Science in Physics & Climate Science
Universiteit Utrecht, Nederland
geboren te Veldhoven, Nederland

Dit proefschrift is goedgekeurd door de promotoren

Samenstelling promotiecommissie:

Rector Magnificus	voorzitter
Prof. dr. ir. L. P. Kouwenhoven	Technische Universiteit Delft, promotor
Prof. dr. ir. L. M. K. Vandersypen	Technische Universiteit Delft, promotor
Onafhankelijke leden:	
Prof. dr. T. Kontos	École Normale Supérieure, Paris
Prof. dr. S. Gröblacher	Technische Universiteit Delft
Dr. M. Blaauboer	Technische Universiteit Delft
Prof. dr. G. A. Steele	Technische Universiteit Delft
Overige leden:	
Dr. W. Pfaff	University of Illinois at Urbana-Champaign

Copyright © 2021 by Damaz de Jong

Casimir PhD Series, Delft-Leiden 2021-34

ISBN 978-90-8593-499-8

An electronic version of this dissertation is available at
http://repository.tudelft.nl/.

CONTENTS

Summary ix

Samenvatting xi

1 Introduction 1
- 1.1 Quantum mechanics . . . 1
- 1.2 Quantum computation . . . 2
- 1.3 Topological protection . . . 3
- 1.4 Majorana box qubits . . . 6
- 1.5 Thesis outline . . . 7

2 Theory 9
- 2.1 Quantum dots . . . 9
  - 2.1.1 Introduction . . . 9
  - 2.1.2 Constant interaction model . . . 10
  - 2.1.3 Transport signatures . . . 11
  - 2.1.4 Superconducting Islands . . . 14
  - 2.1.5 Quantum capacitance . . . 16
  - 2.1.6 Simulation of charge stability diagrams . . . 19
- 2.2 Resonators . . . 20
  - 2.2.1 Introduction . . . 20
  - 2.2.2 Input/output theory . . . 21
  - 2.2.3 Quantum dot coupling . . . 23
  - 2.2.4 Resonator response . . . 24
  - 2.2.5 Resonator asymmetry . . . 25

3 Experimental methods 29
- 3.1 Sample Fabrication . . . 29
  - 3.1.1 Resonators . . . 29
  - 3.1.2 Nanowire based quantum dots . . . 31
  - 3.1.3 Electrostatic Discharge Prevention . . . 33
- 3.2 Measurement setup . . . 34
  - 3.2.1 Cryogenic setup . . . 34
  - 3.2.2 Shielding . . . 35
  - 3.2.3 Cryogenic electronics . . . 35
  - 3.2.4 Room temperature electronics . . . 37

4 Rapid detection of coherent tunneling in an InAs DQD 39
- 4.1 Introduction . . . 40
- 4.2 Experimental approach and setup . . . 40

4.3 Results . . . 42
4.3.1 Observation of quantum capacitance and dispersive shift . . . 42
4.3.2 Quantitative model of the dispersive shift . . . 44
4.3.3 SNR for detecting a tunnel amplitude . . . 46
4.4 Conclusions . . . 47

5 Revealing charge-tunneling processes between a QD and a SC island 49
5.1 Introduction . . . 50
5.2 Results . . . 52
5.3 Discussion and conclusion . . . 57
5.4 Supplemental material . . . 57
5.4.1 Resonator characterization . . . 57
5.4.2 Model for the resonator response . . . 58
5.4.3 Additional Coulomb diamond measurements . . . 59
5.4.4 Additional charge stability diagrams device A . . . 60
5.4.5 Simulation of the charge stability diagrams . . . 60

6 Rapid microwave-only characterization and multiplexed readout 63
6.1 Introduction . . . 64
6.2 Experimental setup . . . 64
6.3 High-frequency conductance measurements . . . 65
6.4 Rapid multiplexed reflectometry . . . 69
6.5 Signal to noise . . . 71
6.6 Conclusions . . . 72
6.7 Acknowledgments . . . 72
6.8 Supplemental material . . . 72
6.8.1 Sample fabrication and experimental setup . . . 72
6.8.2 Fitting procedure for resonator response . . . 74
6.8.3 Correspondence between Y and resonator response . . . 74
6.8.4 Derivation of G_{RF} . . . 76
6.8.5 Determination of $\gamma\ell$ and Z_{nw} from experimental data . . . 77
6.8.6 Comparison of G_{DC} and G_{RF} for all pinchoff curves . . . 77
6.8.7 SNR measurement . . . 78
6.8.8 Relation between SNR and amplifier noise temperature . . . 79

7 On-demand splitting of single Cooper pairs in hybrid QD systems 81
7.1 Introduction . . . 82
7.2 Experimental Setup . . . 82
7.3 Triple dot charge stability diagram . . . 83
7.4 Gate induced Cooper pair splitting . . . 85
7.5 Parity sensing in a quadruple quantum dot . . . 86
7.6 Conclusions & outlook . . . 89
7.7 Supplemental information . . . 90

8 Conclusion & Outlook **95**
8.1 Conclusion 95
8.2 Readout for the Majorana box qubit. 96
8.3 Qubit implementation 98
8.4 Outlook 100

A Fabrication details **105**

Bibliography **109**

Acknowledgements **125**

Curriculum Vitæ **129**

List of Publications **131**

SUMMARY

Quantum mechanics yields exciting opportunities for developing novel technologies. In particular, quantum computation enables performing otherwise intractable calculations. However, unwanted disturbances to the quantum bits (qubits) form a formidable challenge for its implementation. Topologically encoding information protects against these disturbances. Qubits based on Majorana zero modes are promising for achieving topological protection and form a model application for the results of this thesis.

This thesis focuses on gate-based sensing, a scalable and high-fidelity readout mechanism for solid-state quantum information processing devices. We investigate semiconductor/superconductor hybrid quantum dot devices implemented in InAs nanowires. Radio frequency (RF) techniques allow rapid and multiplexed measurements of mesoscopic systems without relying on DC-transport. As such, we show that RF measurements provide a vital tool for rapid readout and quick tune-up of semiconductor qubits.

We start by presenting the theoretical foundations of quantum dots and resonators, necessary for describing the subsequent experimental results. Next, we provide relevant details concerning the experiments in this thesis.

The first experiment shows the implementation of dispersive gate sensing (DGS) in a semiconductor double quantum dot (DQD). We show dispersive shifts on the order of the resonator linewidth and study its behavior for different readout powers. These shifts match theoretical expectations and allow differentiating between Coulomb blockade and resonance with a signal-to-noise ratio (SNR) of 2 within 1 µs.

We subsequently apply DGS to a semiconducting quantum dot coupled to a superconducting island and observe spin-dependent tunneling and simultaneous two-particle tunneling involving Cooper pairs. By inhibiting electron tunneling to the outside leads, we bring the system to an otherwise inaccessible regime and show that DGS can probe floating systems.

The third experiment replaces the MHz-resonators with on-chip superconducting coplanar waveguide resonators in the GHz regime. We extract the differential conductance quantitatively without relying on any DC calibration data. Furthermore, we obtain an SNR of 15 in 1 µs distinguishing Coulomb blockade from resonance in a semiconductor DQD.

In the final experiment, we combine the preceding experimental results and investigate a superconducting island between two semiconductor quantum dots. We can split single Cooper pairs on demand with this geometry while retaining the resulting electrons. Secondly, we measure the electron parity using gate-based sensing in a DQD without external charge sensors.

This thesis concludes by discussing the relevance of the obtained experimental results to the Majorana box qubit and suggestions for subsequent experiments. The results of this thesis show that gate-based sensing is a versatile tool in the context of mesoscopic experiments and quantum information processing devices in particular.

SAMENVATTING

Kwantummechanica biedt spannende mogelijkheden voor de ontwikkeling van nieuwe technologieën. Kwantumberekeningen maken het mogelijk om anderzijds ondoenlijke berekeningen uit te voeren. Ongewenste verstoringen van de kwantumbits (*qubits*) vormen echter een enorme uitdaging voor de uitvoering hiervan. Topologische opslag van de informatie biedt bescherming tegen deze verstoringen. *Qubits* die gebaseerd zijn op Majorana-toestanden zijn veelbelovend om deze topologische bescherming te bereiken en vormen een modeltoepassing voor de resultaten van dit proefschrift.

Dit proefschrift richt zich op *gate-based sensing*, een schaalbaar en nauwkeurig uitleesmechanisme voor vastestof kwantuminformatieverwerkingsapparatuur. We onderzoeken halfgeleider/supergeleider hybride kwantumdots die zijn geïmplementeerd in InAs-nanodraden. Radiofrequentie (RF) technieken maken snelle en gemultiplexte metingen van mesoscopische systemen mogelijk zonder afhankelijk te zijn van DC-transport. Daarmee laten we zien dat RF-metingen een essentieel hulpmiddel zijn voor de snelle uitlezing en afregeling van halfgeleider qubits.

Om te beginnen geven we de theoretische grondslag van kwantumdots en resonatoren om de experimentele resultaten te beschrijven. Vervolgens geven we de relevante details van de experimenten in dit proefschrift.

Het eerste experiment toont de implementatie van *dispersive gate sensing* (DGS) in een halfgeleider dubbele kwantumdot (DQD). We laten frequentie verschuivingen zien die vergelijkbaar zijn met lijnbreedte van de resonator en bestuderen het gedrag ervan voor verschillende uitleesvermogens. Deze verschuivingen komen overeen met de theoretische voorspellingen en maken het mogelijk om Coulomb-blokkade en resonantie the onderscheiden met een signaal-ruisverhouding (SNR) van 2 binnen 1 µs.

Vervolgens passen we DGS toe op een halfgeleidende kwantumdot gekoppeld aan een supergeleidend eiland en observeren we spinafhankelijke *tunneling* en gelijktijdige *tunneling* met twee deeltjes waarbij Cooperparen betrokken zijn. Door de *tunneling* van elektronen naar de elektroden te belemmeren, brengen we het systeem naar een anders ontoegankelijk regime en laten we zien dat DGS ongeaarde systemen kan onderzoeken.

In het derde experiment vervangen we de MHz-resonatoren door supergeleidende coplanaire golfgeleiderresonatoren met GHz-bereik. Daarmee wordt de differentiële geleiding kwantitatief gemeten zonder ondersteuning van DC-metingen. Bovendien verkrijgen we een SNR van 15 in 1 µs, bij het onderscheiden tussen Coulomb-blokkade en resonantie in een halfgeleider-DQD.

In het laatste experiment combineren we de voorgaande experimentele resultaten en onderzoeken we een supergeleidend eiland tussen twee halfgeleider kwantumdots. Met deze geometrie kunnen we desgewenst een Cooperpaar splitsen met behoud van de resulterende elektronen. Ten tweede meten we de elektronenpariteit met behulp van *gate-based sensing* in een DQD zonder externe ladingssensoren.

Tot slot bespreken we de relevantie van de verkregen experimentele resultaten voor de *Majorana box qubit* en vervolg experimenten. Kortom, *gate-based sensing* is een veelzijdig hulpmiddel in de context van mesoscopische experimenten en kwantuminformatieverwerkingsapparaten.

1

INTRODUCTION

The world is not magic — and that's the most magical thing about it.

Sean Carroll

1.1. QUANTUM MECHANICS

The behavior of light is ideal for explaining the role of quantum mechanics in modern-day physics. Not only does light reflect many archetypal quantum mechanical facets, but light itself also fulfills a crucial role in this thesis. Before the advent of quantum mechanics, the nature of light was understood in terms of the Maxwell equations, which describe electricity and magnetism. These equations, in the absence of electrical charges and currents, allow solutions that are traveling electromagnetic waves, which were subsequently identified as rays of light. Many observed aspects of light, such as reflection, dispersion, and diffraction, are explained by this wave-like nature. Particularly diffraction, the description of how light interferes with itself upon encountering an obstacle or opening, holds a surprisingly central role in quantum mechanics. When light from a laser passes through a tiny circular aperture, for example, it causes a diffraction pattern of concentric rings. This behavior is a simple exercise to explain using the wave-like nature of light. The success of this model notwithstanding, however, this explanation of light is incomplete, motivating postulating the theory of quantum mechanics.

To understand why a new physical theory is necessary for the description of light, we consider the photoelectric effect. When light irradiates a material, it can cause the material to emit electrons. By placing a charged electrode in a vacuum with the irradiated material, the energy of the emitted electrons can be measured since changing the voltage on this electrode changes the repelling force on the emitted electrons. The energy can be calculated from the amount of voltage needed on the electrode to prevent any electrons from reaching this electrode. From the Maxwell equations, we expect the energy of the electrons to scale with the intensity of the light source. Experimentally, however, we

1

observe that the energy scales with the frequency[1] of the light rather than its intensity [1]. Building on a mathematical idea from Max Planck, Einstein described the photoelectric effect by assuming the light reaches the material in tiny packets or *quanta* of energy, which later became known as photons [2]. Increasing the intensity of the light source increases the number of photons, but their energy only depends on the frequency of the light source. Even though this prediction agrees with the experiment, it relies on describing light as particles rather than waves. Hence, this leaves us with the following crucial question: how can we harmonize these two descriptions of light?

The duality between particles and waves is at the core of the theory of quantum mechanics. Specifically, quantum mechanics describes all matter in terms of wave functions; a wave-like object which encodes the probability to find the particle at different positions upon measurement. Until such measurement is performed, however, the particle behaves as if it were a wave[2]. This means that the aforementioned effects like dispersion and diffraction can also be observed for all matter. Indeed, it was shown experimentally that electrons can interfere with themselves, proving their wave-like nature [3, 4]. Quantum mechanics revolutionized the understanding of atoms and their interactions, including the explanation of the emission lines of hydrogen [5–7].

Quantum mechanics has been shown to be in agreement with experimental observation up to an astonishing degree of accuracy. Even knowing the physical laws governing the individual particles, however, the collective behavior of a large number of particles can lead to surprising results, of which superconductivity is probably the most notable example [8]. When the system under consideration becomes sufficiently large, the behavior of its constituent particles is no longer suitable for describing the behavior of the system as a whole[3]. This idea is summarized in the title of an essay by Anderson: "More Is Different"[9]. To study systems consisting of many particles, we must abstract away from the behavior of individual particles and identify the relevant collective excitations in the system. Systems on this scale are very attractive experimentally, since they can be designed from the ground up, creating artificial quantum systems in parameter regimes not naturally occurring in nature. This field of study is called *condensed matter physics* to which the work in this thesis also belongs.

1.2. QUANTUM COMPUTATION

In the previous section, the underlying concern is figuring out how to describe the world around us, which lead to the discovery of quantum mechanics. We can also pose the following related question; given the laws of quantum mechanics, can we benefit from them and design systems with macroscopic quantum behavior? This leads to many technological possibilities, such as quantum sensing, quantum encryption, and quantum computation. The latter, a computer that exploits the laws of quantum mechanics,

[1] The frequency of light determines its color.

[2] For larger objects we encounter in daily life, the spread in possible positions is sufficiently small such that the wave-like nature is negligible, effectively hiding the laws of quantum mechanics. This obscurity often causes quantum mechanics to be treated with much awe and apprehension but must not be mistaken for lack of understanding.

[3] As an analogy, a thorough understanding of the chemistry of water will show to be of very limited use when trying to understand the propagation of waves in the sea.

would be able to perform calculations that are intractable to perform on a classical computer [10, 11]. The reason for this tremendous speed-up is superposition, the possibility for particles to exist in multiple states at once, a direct consequence of the probabilistic interpretation of the wave function. Whereas a classical bit can only be 0 or 1, its quantum analog, the qubit, can be a combination of 0 and 1 at the same time. This is a rather different statement than the qubit having some value between 0 and 1; instead, it is more similar to playing two notes on a musical instrument at the same time, which will sound very different than playing one note of the average frequency. It is only when the qubit is not being measured that it can maintain the wave-like property of being in a superposition. When the qubit is measured, or read out, its wave function collapses and it will assume either the value 0 or 1 with probabilities given by its wave function. Large collections of N qubits can be brought into a collective superposition state, called *entangling*, spanning not just 2 possibilities, but 2^N, doubling for every qubit. With only three qubits, there are already 8 available states[4], and this number doubles for every extra qubit. The intuitive idea is then clear, instead of a classical computer algorithm trying possible solutions one at a time, a quantum algorithm can test every possible solution at the same time. In practice, it is not quite as simple as this, since the wave function collapses upon readout. This means we can obtain at most one result from a quantum computation. Developing algorithms that exploit the quantum computer is an active field of research.

One of the main obstacles towards realizing a quantum computer is its sensitivity to noise. Any operation (or gate) performed on the qubit only has finite accuracy, introducing an error in the quantum information. Furthermore, any inadvertent measurement of a qubit disturbs the wave-like nature of the system and destroys the quantum information, this process is called *decoherence*. More precisely, any coupling of the system to its environment causes a disturbance and must be reduced as much as possible. On the other hand, the qubit must be coupled to the environment in order to control it. This contradiction makes the realization of a quantum computer very challenging. When the decoherence rate is small enough, many qubits can be operated in tandem to collectively form a single logical qubit with an even lower decoherence rate. This method spreads the quantum information of a single logical qubit over multiple physical qubits [12]. The ability to correct these quantum errors increases the feasibility of constructing a quantum computer, but the noisier the physical qubits are, the more of them are needed to form a logical qubit[5]. Therefore, reducing the decoherence rate of individual qubits is paramount and leads us to investigate how quantum information can be protected using the concept of topology.

1.3. TOPOLOGICAL PROTECTION

Topology is a branch of mathematics that endows structure (called a *topology*) to a set of points, introducing an abstract sense of closeness between these points. Of particular interest to us are topological invariants, quantities that solely depend on this structure. This means that these invariants are preserved under deformations that leave points that

[4] We denote these states by listing each individual qubit state. The 8 states are 000, 001, 010, 011, 100, 101, 110, and 111.

[5] Importantly, the error rate of the individual qubits must be sufficiently low for this method to work.

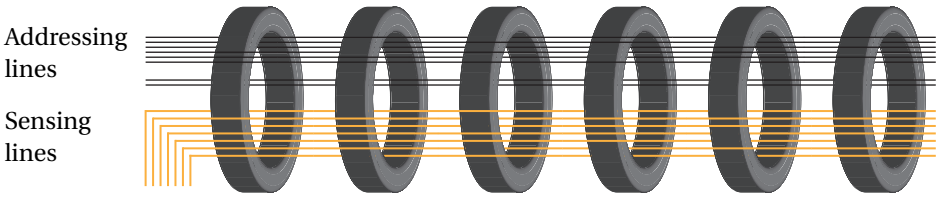


Figure 1.1: **Topological protection of classical computer memory.** A schematic representation of Core rope memory, adapted from Ref. [13]. The sensing lines, shown in yellow, encode a 0 or 1 by either bypassing or threading through the individual core.

were close before the deformation, close together, also called *continuous deformations*. Loosely speaking, topological invariants depend on the global structure rather than local details. For example, the number of holes in a sphere is zero, while a torus has one, no matter how these shapes are deformed continuously, i.e. without gluing or tearing. The idea of topological protection is to encode the information into a topological invariant, rendering it immune to any local (or continuous, to be more precise) perturbation.

Topological protection cannot only be applied to quantum computers, but has already been used successfully in classical computers. In particular, the guidance computers of the Apollo space program provide a fruitful example to illustrate the principle of topological protection. These guidance computers needed a way to permanently store their programs without any possibility for data corruption [13, 14]. Core Rope memory provides a way to topologically encode classical data, as we explain below. Fig. 1.1 shows a schematic representation of Core Rope Memory[6]. Information is encoded by sensing lines (shown in yellow) either threading through a core representing a 1 or bypassing it to represent a 0, encoding one bit of information per core. Using the addressing lines, one core can be made to switch and generate an output pulse on every sensing line that threads it. As such, the information is encoded topologically. Indeed to flip one bit, the wire must pass through the solid edge of a core, which is impossible without cutting and mending the wire, clearly a non-continuous perturbation[7].

In the example discussed above, the concept of topology provides rigidity to the data stored. This is achieved by making it impossible at the physical level to store anything in between 0 and 1. The field of topological quantum computation (TQC) seeks to use topological mechanisms to increase the rigidity of quantum computers [16]. One promising technique is braiding the world-lines[8] of multiple particles into a knot in a very similar fashion to weaving the sensing wires in the example above. In a 3+1 dimensional world, every knot can be untangled without cutting the strings, making it impossible to topologically encode information in it. Untangling the braid makes the operation equivalent to the normal exchange of particles, which is described by bosonic or fermionic exchange statistics and amounts to trivial phase rotations of the wave function only. To allow for non-trivial knots, we must restrict the system to 2+1 dimensions. In-

[6] It is interesting to mention that Braid transformer memory, a variant of Core Rope Memory, has also been proposed [15].

[7] Here we assume the wires are fixed at their endpoints.

[8] A world-line describes the position of a particle through time, forming a line through space-time.

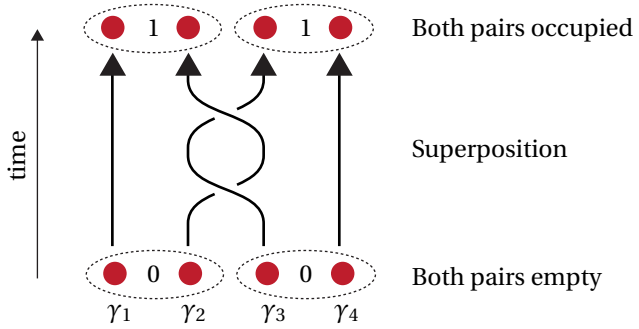


Figure 1.2: **Schematic of a braiding operation in a single topological qubit formed with four Majorana zero modes.** The MZMs are represented by red dots and labeled γ_1 through γ_4. In this schematic, time flows in the upward direction. Exchanging γ_2 and γ_3 twice changes the 0 state of the qubit into the 1 state. Readout of the qubit is performed by fusing γ_1 and γ_2 (or equivalently γ_3 and γ_4) and measuring whether the resulting fermionic state is empty or filled represented by 0 and 1 in the dashed circles.

deed, the particles braided in TQC live in less than 3 spatial dimensions to allow for more exotic exchange statistics. Particles obeying non-trivial exchange statistics are known as non-abelian anyons, making them neither bosons nor fermions. Importantly, we can take advantage of the designability aspect of condensed matter systems and create artificial, low-dimensional geometries to facilitate the existence of non-abelian anyons.

To induce anyons and verify their existence is a challenging experimental endeavor. Theoretically, there are many different types of non-abelian anyons proposed to exist in experimental systems [16]. For this thesis, we focus on one type of these, Majorana zero modes (MZMs), which are predicted to appear at the opposite ends of a 1-dimensional *p*-wave superconducting wire [17]. Two MZMs together combine into a single fermionic mode which can either be occupied or empty, representing the 0 and 1 state, respectively, yielding a single degree of freedom. Whether the total number of occupied fermionic modes is even or odd is called the parity and must be conserved in an isolated system. We therefore need an extra pair of MZMs to absorb an extra fermion whenever the remaining MZMs change their total parity. Hence, we need at least four MZMs to encode a single qubit[9]. The occupation of a pair of MZMs can only be changed or measured by bringing two MZMs close together, a process called *fusion*, or by exchanging their positions, called *braiding* [18]. Consider two MZM pairs, both initialized in the empty state as depicted in Fig. 1.2. Exchanging two MZMs between the pairs brings the system to an exact equal superposition of both pairs being filled and empty. The following three subsequent exchanges leave both pairs filled, in superposition and empty again, respectively. In short, quantum information is stored and manipulated in a precise, topologically protected way.

Unfortunately, there are no known *p*-wave superconducting materials in nature. The necessary ingredients can be engineered however, combining induced s-wave superconductivity in a semiconductor nanowire with spin orbit coupling (e.g. InSb or InAs) and a large magnetic field [19, 20]. Shortly after this mechanism was proposed, the first exper-

[9] MZMs can only be generated in pairs of two.

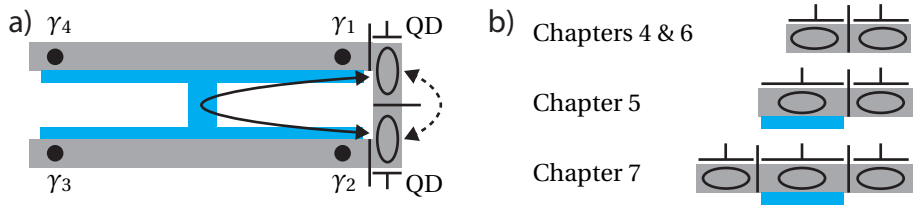


Figure 1.3: **Schematic of the Majorana box qubit** The gray structures represent semiconductor nanowires where the ovals represent quantum dots induced in the wire. Superconductivity is induced in the system with the connected superconducting structures, shown in aqua. Finally, the location of the MZMs are shown by black circles. **a**) A version of the Majorana box qubit containing four MZMs, adapted from Ref. [25]. **b**) The different substructures of the Majorana box qubit studied in this thesis.

imental signatures of MZMs were observed [21]. So far, however, no experiments have been able to probe the non-abelian nature of MZMs. Multiple different proposals have been made for achieving braiding and fusion in a practical experiment [22–26], but have not been implemented successfully. In the next section, we discuss one of these proposals for braiding Majorana zero modes in more detail, as this proposal sparked the initial motivation to investigate gate-based readout of hybrid quantum dot systems, the main topic of this thesis.

1.4. MAJORANA BOX QUBITS

Surprisingly, to expose the non-abelian exchange statistics of MZMs and perform a braiding experiment, the physical location of the MZMs can remain fixed. It is sufficient to consecutively measure different combinations of two MZMs to achieve an effective braiding operation [25–27]. Fig. 1.3a shows the proposal for the Majorana box qubit, as outlined in Ref. [25]. The device consists of two superconducting wires in the topological regime, joined in the middle by a superconducting section. Two MZMs are coupled via a double quantum dot which facilitates the readout procedure by introducing a tunneling component between both dots via these two MZMs. This geometry allows initializing two pairs of MZMs in the empty state such that γ_1 and γ_4 fuse to the vacuum state (and similar for γ_2 and γ_3). Secondly, the combined state of γ_1 and γ_2 can be measured. Hence this geometry allows performing a single MZM exchange or equivalently a fusion experiment [24]. To perform a full braiding experiment using a measurement-based protocol, at least six MZMs are needed and will not be considered further in this thesis, but the geometry shown in Fig. 1.3a can be expanded to a multi-qubit geometry.

Realizing the Majorana box qubit proposal in practice requires solving several experimental difficulties, ranging from inducing MZMs to fabricating the necessary device geometry. Here, we focus on one of these; the mechanism by which a pair of MZMs can be measured. Since the qubit is topologically protected, any local measurement will be unable to retrieve the stored information. Hence, a non-local measurement is needed to circumvent the topological protection. Crucially, the tunneling amplitude between the two quantum dots through the superconductor, represented by the solid arrow in Fig. 1.3a, probes both γ_1 and γ_2 together and is therefore non-local. Depending

on whether this pair of MZMs is filled or empty, the tunnel coupling acquires a 180 degree phase shift. This means it will interfere either constructively or destructively with the trivial tunneling path, represented by the dashed arrow. Therefore, the state of the MZM pair can be obtained by measuring the tunnel coupling between the two quantum dots.

The tunnel coupling between the two quantum dots can be measured using gate-based sensing, the main topic of this thesis. In essence, this method measures how the electron charge in the quantum dots will move around due to the oscillating electric field in the resonator. From the perspective of the resonator, the moving electron acts as a restriction to the resonator oscillation, lowering its resonance frequency. For larger tunnel couplings, the electron distribution between the two quantum dots will be more hybridized, resulting in less movement of charge as a result of this oscillation and therefore a smaller frequency shift. In conclusion, by measuring shifts in the resonance frequency, we can obtain the tunnel coupling and thereby read out the qubit state. It is this resonator-to-quantum-dot coupling that is studied in this thesis.

1.5. THESIS OUTLINE

The inspiration for the experiments performed in this thesis is the Majorana box qubit, described in the previous section. Specifically, we investigate gate-based sensing in the context of quantum dot systems in InAs nanowires. The experimental chapters investigate different quantum dot sequences, summarized in Fig. 1.3b. In doing so, we develop high-frequency measurements as a reliable measurement technique for mesoscopic devices, relevant not only for MZM-physics but a broad scope of quantum information devices.

In Chapter 2, we describe two important topics that are relevant for the experimental chapters contained in this thesis. First, in Sec. 2.1, we provide the theoretical background for quantum dot systems and develop a model we use for comparison with experimental data. Secondly, in Sec. 2.2, we derive a model for the resonators used for gate-based sensing based on Input/Output theory and find equations for the resonator response.

In Chapter 3, we provide details pertaining to sample fabrication used for the samples described in this thesis. We subsequently specify details regarding the experimental setup such as cryogenics, shielding and room-temperature electronics.

In Chapter 4, we experimentally study the quantum capacitance resulting from charge hybridization in a double quantum dot. The quantum capacitance induces a frequency shift in the off-chip resonators which are measured in reflection. The obtained frequency shifts and their dependence on probe power agree well with theoretical prediction.

In Chapter 5, we use a similar experimental approach to the previous chapter, but in this case one of the quantum dots is a superconducting island. Firstly, we observe spin-dependent tunneling amplitudes between the two dots. Secondly, we observe two-electron processes, simultaneously exchanging electrons between two different reservoirs. Using the floating regime, we obtain information on superconducting subgap states, consistent with transport data.

In Chapter 6, we change the type of resonators used for the experiment. Rather than using off-chip resonators, we use on-chip coplanar waveguide resonators in the giga-

hertz regime. First, using these resonators we obtain quantitative values for device conductance without using any DC calibration measurements. We then show the ability to multiplex multiple resonators. Finally, we show that we can distinguish Coulomb blockade from charge degeneracy with a signal-to-noise ratio of 15 within 1 µs in a normal double quantum dot.

In Chapter 7, we use the on-chip resonators in a multi-quantum dot system with one superconducting island. Multiplexing all resonators connected to the different dots, we show the ability to identify the different stable charge regions in the system. We find a transition that corresponds to Cooper pair splitting, where two electrons simultaneously tunnel to two different quantum dots connected to the two ends of the superconducting island. Furthermore, by tuning two quantum dots into a parity sensor, we observe electrons being ejected from the superconducting island by crossing the appropriate charge transitions.

Finally, in Chapter 8, we put the results obtained in the different experimental chapters in the context of the box qubit proposal. Specifically, we discuss the feasibility of dispersive gate sensing for this experiment and discuss a few different implementations. Lastly, we propose experiments that should be completed before realizing the box qubit.

2

THEORY

Als je heel diep over iets nadenkt, dan kom je altijd uit bij iets dat niet klopt.

Herman Finkers

2.1. QUANTUM DOTS

2.1.1. INTRODUCTION

The first theme of this chapter is quantum dots. At its core, a quantum dot is an electron box providing confinement in all three directions, such that there are no spatial degrees of freedom left [28, 29]. Much like atoms, only discrete energy levels are available for electrons in quantum dots, which are therefore also referred to as artificial atoms [30]. The discrete energy spectrum makes them a quintessential quantum system. Importantly, as opposed to regular atoms, the energy spectrum can be tuned by the size of the system and the electrostatic environment. This makes quantum dots an exciting topic of study for many physical phenomena as well as a versatile tool with many applications.

To leverage the quantum properties of quantum dots, the temperature of the system must be smaller than the energy level separation [31, 32]. In general, making the system smaller increases this separation, while cryogenic refrigeration can significantly lower the temperature. Lithographic fabrication methods enable the mesoscopic length scales necessary to realize quantum dots in various material platforms at cryogenic temperatures. These platforms include 2-dimensional electron gasses (2DEGs) [33–36], carbon nanotubes (CNTs) [37, 38], and semiconducting nanowires [39–41].

As far as this thesis is concerned, the most relevant application of quantum dots is in the context of quantum information processing. Firstly, the degrees of freedom in quantum dots can store quantum information. Two prominent examples for the creation of qubits are charge occupation [42] and spin configuration of the confined electrons [43]. Rather than storing quantum information in the dots, they can also function as readout devices. Electrical conduction through a quantum dot depends on the charge in the

environment. This has been exploited to create sensitive charge sensors [44]. Likewise, the electric compressibility of a quantum dot reveals the electron tunneling amplitude, which is of primary interest in this thesis [45]. The compressibility can conveniently be measured through gate sensing using resonators, which is the topic of the second half of this chapter. For the readout of topological systems, both charge sensing and gate sensing have been proposed, making readout with quantum dots an important topic for topological quantum computation [24–26].

In this section, we will present the theory necessary to understand the behavior of quantum dots revealed by the experiments presented in this thesis. First, in Sec. 2.1.2 we describe the electrostatic energy, which is the dominant contribution for understanding the charge configuration in quantum dot systems. The resulting model is used in Sec. 2.1.3 to derive the transport mechanisms through the system. Next, in Sec. 2.1.4 superconductivity is added to the model to study its interplay with the charging physics of the constant interaction model. In contrast to the point of view of electron transport through the device, we focus in Sec. 2.1.5 on signatures that do not require any electron tunneling into the quantum dots, treating it instead as a floating quantum system. In Sec. 2.1.6 we combine the preceding sections into a single framework. This allows us to discuss simulations of charge behavior in quantum dot devices used in the remainder of this thesis.

2.1.2. CONSTANT INTERACTION MODEL

Before the experimental signatures of quantum dot systems are discussed, we will first define a simplified model to describe these systems. In order to arrive at this model, we make two assumptions. Firstly, we assume that the interaction energy between the electrons is given by the electrostatic energy described below. Secondly, we assume the discrete energy levels of the individual electrons are not affected by these interactions [46, 47].

In Fig. 2.1, a schematic of the quantum dot systems under consideration is given[1]. Every quantum dot and voltage gate can be thought of as a node with a definite voltage and charge. The amount of capacitance between these different nodes determines how the different voltages and charges interact. It is convenient to describe all capacitances c_{ij} between nodes i and j by the capacitance matrix, where nodes are sorted into 2 categories; quantum dots, $\mathbf{c}$ and voltage gates, $\mathbf{v}$ [48]:

$$C_{ij} = \begin{pmatrix} C_{\mathbf{cc}} & C_{\mathbf{cv}} \\ C_{\mathbf{vc}} & C_{\mathbf{vv}} \end{pmatrix}_{ij} = \begin{cases} -c_{ij} & i \neq j \\ \sum_{k\neq i} c_{ik} & i = j \end{cases}. \tag{2.1}$$

Given the charges on all the quantum dots, $-|e|\vec{N} = \vec{Q}_{\mathbf{c}}$ and the induced charges by the voltage gates $-|e|\vec{N}_{\mathrm{g}} = C_{\mathbf{cv}}\vec{V}_{\mathbf{v}}$, the voltage $\vec{V}_{\mathbf{c}}$ on every quantum dot is given by:

$$\vec{V}_{\mathbf{c}} = C_{\mathbf{cc}}^{-1}(\vec{Q}_{\mathbf{c}} - C_{\mathbf{cv}}\vec{V}_{\mathbf{v}}). \tag{2.2}$$

[1] In the schematic, only the capacitors between neighboring quantum dots and gates are drawn to increase clarity.

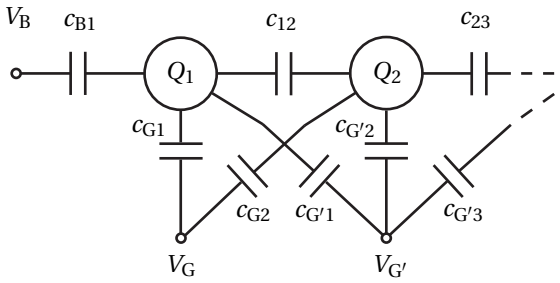


Figure 2.1: Schematic of the capacitance network corresponding to a multi quantum dot system. The quantum dots 1 and 2 are denoted by large circles and form the charge nodes in the system. The smaller circles represent the voltage nodes and tune the electrostatic environment of the quantum dots. The bias node and two gate nodes are labeled by B, G, and G′ respectively.

The model described in this section assumes that all interaction energy between the electrons is given by the electrostatic energy of the capacitors. Specifically, this energy can be obtained by calculating the energy it takes to charge the quantum dots up to their stable charge configuration $\vec{Q}_\mathbf{c}$ while keeping the voltage gates $\vec{V}_\mathbf{v}$ constant, taking into account that the voltage on every quantum dot depends on the current charge occupation of the dots[2]:

$$U_{\text{el}} = \int_{\vec{0}}^{\vec{Q}_\mathbf{c}} \vec{V}_\mathbf{c}(\vec{q}) \cdot \mathrm{d}\vec{q}. \tag{2.3}$$

Defining the charging energy matrix $E_\text{C} = \frac{e^2}{2C_\mathbf{cc}}$ the integral above can be found to yield[3]

$$U_{\text{el}} = (\vec{N} - \vec{N}_\text{g}) E_\text{C} (\vec{N} - \vec{N}_\text{g}). \tag{2.4}$$

To obtain the total energy from the electrostatic energy, according to the second assumption of the constant interaction model, we only have to add the level energy $E_{i,l}$ of every electron l on dot i in the system.

A convenient way to think about the energy of the system for different particle numbers is to consider the electrochemical potential μ, the energy cost of adding a single electron to the system. Concretely, to add an electron to dot i is associated with an energy cost of

$$\mu_i(\vec{N}) = U_{\text{el}}(\vec{N}) - U_{\text{el}}(\vec{N} - \hat{e}_i) + E_{i,N_i}, \tag{2.5}$$

where $\hat{e}_i$ denotes the i-th unit vector of the standard basis.

2.1.3. TRANSPORT SIGNATURES

The model developed in the previous section is sufficient to describe several experimental signatures of quantum dot systems. In this thesis, we are mainly concerned with the

[2] In principle one needs to specify the exact path taken when calculating a line integral. In this case, the result is path independent, and the path notation is omitted.

[3] Here, we neglect an additive constant, which represents the freedom of choosing the starting point $\vec{0}$ in the integral of Eq. (2.3).

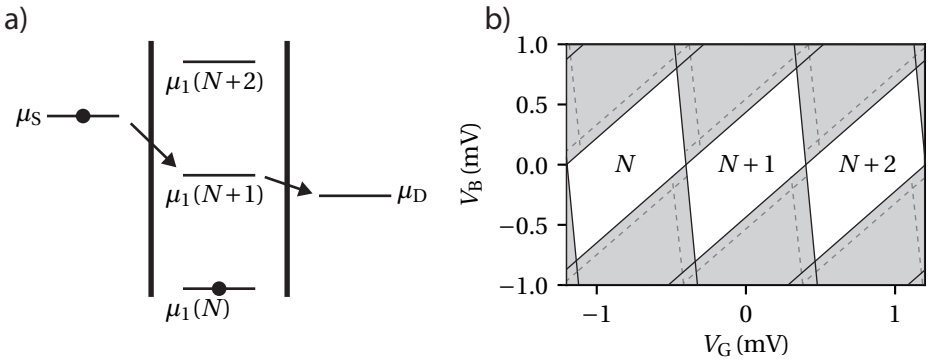


Figure 2.2: **a)** Chemical potential levels for a single quantum dot. There is a single charge state in the bias window between μ_D and μ_S contributing to transport through the system. **b)** Schematic showing the Coulomb blockade regions in a single quantum dot. The bias voltage is applied to the source electrode, keeping the drain voltage fixed. Transport is blocked in the white, diamond-shaped regions. Excited states cause additional transport channels, represented by dashed lines.

electrical properties of these systems. First, in this section, we will describe the conductance resulting from electron transport through a network of quantum dots. Subsequently, in Sec. 2.1.5, we will describe the effect of local changes in the electron density on the gate capacitance.

By weakly coupling a source and drain reservoir to the quantum dot in the form of leads, electrons can flow between these two reservoirs. This flow results in a finite electrical conductance, which can be measured experimentally. In general, the flow of electrons is inhibited as there is an energy cost associated with changing the charge configuration in the quantum dot. Current can only flow through the system when a cycle of energetically favorable transitions exists, starting with an excess electron in the source electrode and ending with an excess electron in the drain electrode, or vice versa.

For a single quantum dot between a source and a drain, the different transport mechanisms are visualized in Fig. 2.2a. Whenever there exists a charge exchange process in the bias window (i.e. in between the chemical potential of the source, μ_S and drain, μ_D), one electron can be loaded onto the dot from the source and unloaded to the drain consecutively. This allows for current to flow, one electron at a time. If no levels are available in the bias window, no current can flow, and the system is said to be in Coulomb blockade. This means that, without bias voltage, current can only flow when the quantum dot level is on resonance with the source and drain, known as a Coulomb peak.

The amount of bias voltage needed to enable transport depends on the detuning between the relevant quantum dot level and the chemical potential of the drain. The interplay of bias voltage and gate voltage[4] is shown in Fig. 2.2b, where we assume $\mu_D = 0\,V$. Given the shape of the configurations without conductance, the Coulomb blockade regions are called Coulomb diamonds. When the bias window is large enough, electrons

[4] We assume a finite value for c_{B1}, which causes cross-coupling between the source and gate electrode. This results in a small extra slope in the lines of Fig. 2.2b.

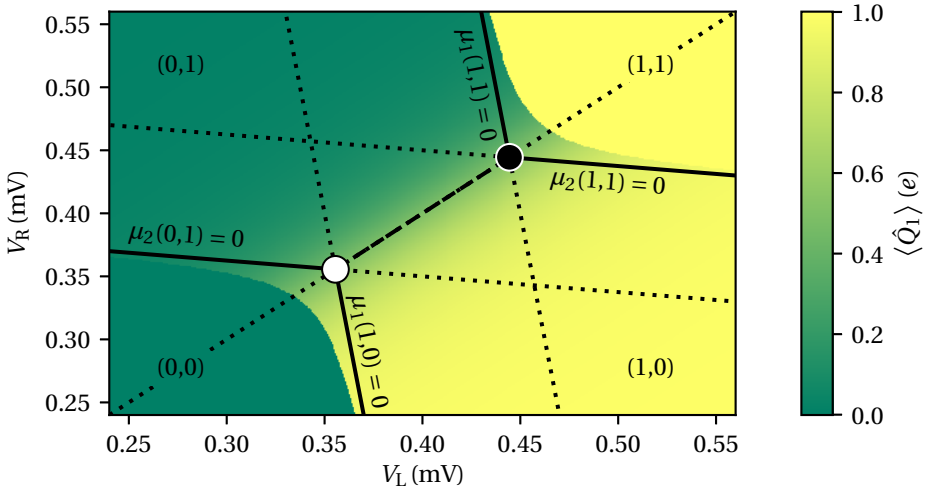


Figure 2.3: Charge stability diagram of a double quantum dot as a function of left and right gate voltage. The lines denote when specific charge transitions are on resonance with the source and drain chemical potentials, $\mu_S = \mu_D = 0$ V. When the charge transition does not involve the ground state, it is drawn as a dotted line instead to signify that the transition will only contribute to transport if the quantum dot is in an excited charge state. The lowest charge state in the four quadrants is denoted with brackets in the figure. Circular markers denote the triple points, occurring at the crossing of three solid lines. Figure adapted from Ref. [48]. The color scale denotes the expectation value of charge on the first quantum dot, solved with the model of Sec. 2.1.6.

can not only tunnel through the groundstate level $E_{i,l} = E^0_{i,l}$, but also through some excited state level energy $E^1_{i,l}$. This allows for a higher conductance, shown in Fig. 2.2b by dashed lines.

The case of a double quantum dot is slightly more interesting, as an electron in one of the two dots might prevent electrons tunneling to the other dot. As such, there are two cycles that can contribute to transport at zero bias. The condition for these processes to happen is $\mu_S = \mu_1(N_1 + 1, N_2) = \mu_2(N_1, N_2 + 1) = \mu_D$ for the first cycle and $\mu_S = \mu_1(N_1 + 1, N_2 + 1) = \mu_2(N_1 + 1, N_2 + 1) = \mu_D$ for the second cycle. These conditions are shown in Fig. 2.3 by the white and black marker, respectively. In other words, for these processes to occur, three charge states must be degenerate; hence the gate configurations where transport happens are known as triple points.

When only two of the three charge states are degenerate, transport is inhibited as one state needed to complete the cycle is energetically inaccessible. Quantum mechanics allows this missing state to be occupied virtually however, allowing the transport cycle to occur as a co-tunneling process [49]. The locations in the charge stability diagram where these co-tunneling processes occur are marked with the solid lines in Fig. 2.3. The strength of these transitions not only depends on the tunnel barriers in the system but also on the detuning between the leads and the virtual state.

2.1.4. SUPERCONDUCTING ISLANDS

The interaction between quantum dots and superconductivity forms a central part of this thesis, which is motivated by the crucial role of superconductivity in the formation of Majorana zero modes. Before describing this relationship, however, it is important to first discuss the details of superconductivity.

Historically, interest in superconductors was sparked by their ability to conduct electricity without dissipation [8]. Equally striking is the fact that a superconductor expels all magnetic field lines from its interior, which is known as the Meissner effect [50]. These phenomena were first explained by the London equations, which postulate a supercurrent density and use the Maxwell equations to predict the Meissner effect [51]. Understanding of superconductivity increased with Ginzburg-Landau theory [52], a phenomenological model based on Landau theory of phase transitions using a complex order parameter to describe the superconducting state.

To describe the microscopic behavior of the system, we must go beyond the aforementioned models to the BCS theory of superconductivity [53, 54]. The crucial ingredient for BCS theory is an attractive interaction dominating over the Coulomb repulsion between electrons close to the Fermi energy. The attraction between electrons can intuitively be explained by the electrons deforming the ionic lattice through Coulomb interaction [55–57]. Critically, the deformation left behind by an electron relaxes on a longer time scale than the electron moving through the lattice. Hence electrons leave a positively charged region behind, attracting other electrons, generating correlated movement of electrons in the superconductor. In short, the interaction is mediated by lattice vibrations, i.e. phonons. Denoting the interaction by $V_{\mathbf{kl}}$ leads to the reduced BCS Hamiltonian:

$$H = \sum_{\mathbf{k}\sigma} \xi_{\mathbf{k}} c^\dagger_{\mathbf{k}\sigma} c_{\mathbf{k}\sigma} - \sum_{\mathbf{kl}} V_{\mathbf{kl}} c^\dagger_{\mathbf{k}\uparrow} c^\dagger_{-\mathbf{k}\downarrow} c_{-\mathbf{l}\downarrow} c_{\mathbf{l}\uparrow}. \tag{2.6}$$

Here, $c^\dagger_{\mathbf{k}\sigma}$ and $c_{\mathbf{k}\sigma}$ are the creation and annihilation operator for an electron with momentum $\mathbf{k}$ and spin σ. Finally, $\xi_{\mathbf{k}}$ denotes the kinetic energy relative to the Fermi energy.

The attractive interaction causes an energetic preference towards the formation of bound states, in which electrons pair up into Cooper pairs [58]. The spatial separation between the constituent electrons of a Cooper pair is given by the superconducting coherence length, generally exceeding the inter-particle distance [59]. Even though Cooper pairs cannot be interpreted as localized particles, they obey Bosonic rather than Fermionic particle statistics, allowing them to condense into a single quantum state. Assuming a macroscopic occupation of Cooper pairs states in the groundstate means that fluctuations of $c_{-\mathbf{q}\downarrow} c_{\mathbf{q}\uparrow}$ around its expectation value $\langle c_{-\mathbf{q}\downarrow} c_{\mathbf{q}\uparrow} \rangle$ are small. Hence we can use the mean field approximation[5]:

$$H = \sum_{\mathbf{k}\sigma} \xi_{\mathbf{k}} c^\dagger_{\mathbf{k}\sigma} c_{\mathbf{k}\sigma} - \sum_{\mathbf{k}} \left(\Delta_{\mathbf{k}} c^\dagger_{\mathbf{k}\uparrow} c^\dagger_{-\mathbf{k}\downarrow} + \overline{\Delta}_{\mathbf{k}} c_{-\mathbf{k}\downarrow} c_{\mathbf{k}\uparrow} \right) \text{ with } \Delta_{\mathbf{k}} = \sum_{\mathbf{q}} V_{\mathbf{kq}} \left\langle c_{-\mathbf{q}\downarrow} c_{\mathbf{q}\uparrow} \right\rangle. \tag{2.7}$$

The pairing represented by $\Delta_{\mathbf{k}}$ ensures a slight energy gain filling the available phase-space in pairs rather than individual electrons. Indeed, the ground state of the system $|\Omega_s\rangle$ only contains paired electrons. Therefore, when adding one additional electron to

[5] Here we drop constant terms and terms proportional to $(c_{-\mathbf{l}\downarrow} c_{\mathbf{l}\uparrow} - \langle c_{-\mathbf{l}\downarrow} c_{\mathbf{l}\uparrow} \rangle)(c^\dagger_{\mathbf{k}\uparrow} c^\dagger_{-\mathbf{k}\downarrow} - \langle c^\dagger_{\mathbf{k}\uparrow} c^\dagger_{-\mathbf{k}\downarrow} \rangle)$

the superconductor, it can no longer remain in its ground state. Instead the system is left in an eigenstate of the form[6] $(u_{\mathbf{k}}^* c_{\mathbf{k}\uparrow}^\dagger - v_{\mathbf{k}}^* c_{-\mathbf{k}\downarrow})|\Omega_S\rangle$ corresponding to an energy increase of $\sqrt{\xi_{\mathbf{k}}^2 + |\Delta_{\mathbf{k}}|^2}$ relative to the ground state energy[7]. Disregarding the $\mathbf{k}$ dependence, this means that an odd particle state will have an excess energy of at least $\Delta = |\Delta_{\mathbf{k}}|$. In other words, the excitation spectrum of the Hamiltonian in Eq. (2.7) is gapped with the density of states shown in Fig. 2.4a, where an excess electron can only exist in the superconductor as a quasi-particle excitation above this gap. It is possible for isolated states to be available inside the superconducting gap with an energy $E_0 < \Delta$. There are multiple explanations for the appearance of such states [61–65], but we will use the term *subgap state* regardless of the microscopic origin.

To analyze the behavior of superconductivity in quantum dot systems, we combine the theory of superconductivity with the charging physics of Sec. 2.1.2. The assumptions of the constant interaction model are not met, however, since the electrostatic energy is no longer sufficient to describe the interactions between the electrons, which must now also include the attractive potential represented by Δ in Eq. (2.7). To simplify the system, we will assume that at most one particle resides above the gap in the superconductor while all other electrons remain paired up in Cooper pairs. Hence, under this assumption, the parity of the superconductor is sufficient to include superconductivity in the interaction energy. Specifically, the odd parity states incur an energy penalty of Δ or E_0 relative to the even parity state.

Consider the charge occupation of a single superconducting dot. When $\Delta > E_C$, it is never energetically favorable for the superconductor to contain an odd number of particles. This changes for $\Delta < E_C$, where the ground state parity will be odd for some gate regions; these regions will be smaller than the even parity regions. The transition energies corresponding to the lowest few charge states is shown in Fig. 2.4b. Conductance can happen when the lowest energy levels are degenerate, which causes $2e$ periodic Coulomb peaks when $\Delta > E_C$. In contrast, when $\Delta < E_C$ peaks show even and odd spacing. The even and odd regions have a length of $\delta n^{e/o} = 1 \pm E_0/E_C$ where we define $E_0 = \Delta$ whenever no subgap states are present.

Motivated by applications relating to topological quantum computation, we now consider coupling normal quantum dots to superconducting quantum dots. This kind of dot configuration constitutes an ideal platform to study superconducting properties in detail. The quantum dots not only allow the superconductor to be studied locally, see Sec. 2.1.5, but can also be used to control its charge occupation, see Chapter 5 and Chapter 7. The gate regime where the superconductor will be loaded with an extra quasiparticle, i.e. the odd parity state, is now determined by all charging energies in the system. Calculation of the boundaries of these different charge configurations is conveniently done with computer simulations, described in detail in Sec. 2.1.6.

[6] In the case of a spin-up excitation.

[7] Indeed, it can be confirmed that $H(u_{\mathbf{k}}^* c_{\mathbf{k}\uparrow}^\dagger - v_{\mathbf{k}}^* c_{-\mathbf{k}\downarrow})|\Omega_S\rangle = (u_{\mathbf{k}}^* c_{\mathbf{k}\uparrow}^\dagger - v_{\mathbf{k}}^* c_{-\mathbf{k}\downarrow})(H + \sqrt{\xi_{\mathbf{k}}^2 + |\Delta_{\mathbf{k}}|^2})|\Omega_S\rangle$ for appropriate values for the coherence factors $u_{\mathbf{k}}^*$ and $v_{\mathbf{k}}^*$ [60].

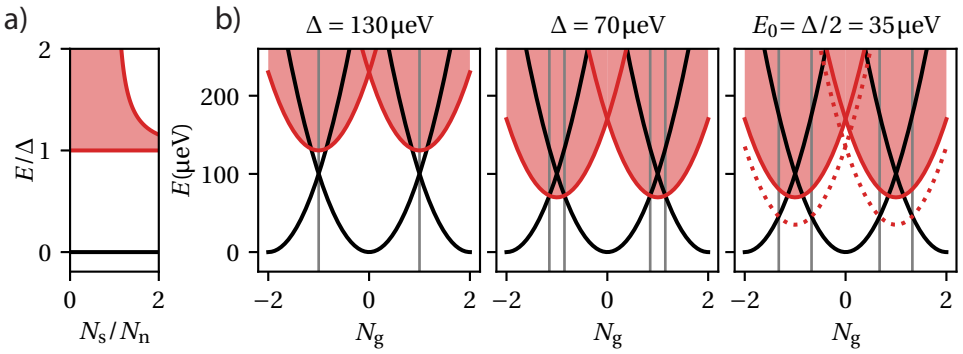


Figure 2.4: **a)** The density of states $N_s/N_n = |E|/\sqrt{E^2-\Delta^2}$ of excited states in the superconductor relative to the Fermi energy. Within the superconducting gap, i.e. for energies smaller than Δ, the density of states is zero. **b)** Transition energies in a single superconducting island without supgap state for $\Delta = 130\,\mu$eV (left) and $\Delta = 70\,\mu$eV (middle) and with a subgap state at $E_0 = 35\,\mu$eV (right). The charging energy is taken as $E_C = 100\,\mu$eV for all three cases.

2.1.5. QUANTUM CAPACITANCE

In Sec. 2.1.3 we investigated transport phenomena which can be observed through measuring the differential conductance. In contrast, in this section, we will focus on the dependence of electron density on gate voltage which gives rise to a differential capacitance. Specifically, we are interested in the effective capacitance from gate electrode to ground C_{eff}, see Fig. 2.1. To calculate this capacitance it is not enough to replace all capacitors in the quantum dot network with the equivalent capacitance since the effect of electrons hopping to and from the different quantum dots must also be taken into account.

Concretely, the differential capacitance can be found using the model described in Sec. 2.1.2 and calculating

$$C_{\text{eff}} = \frac{\partial Q_G}{\partial V_G}, \tag{2.8}$$

where Q_G and V_G denote the charge and voltage on the gate electrode respectively. To proceed, assume that the gate electrode only couples to a single quantum dot i with voltage $\vec{V}_{\mathbf{c},i}$, total capacitance C_Σ and total charge Q_i which we promote to a quantum mechanical observable with expectation value $\langle\hat{Q}_i\rangle$. Hence we find $Q_G = C_G(V_G - \vec{V}_{\mathbf{c},i})$ and using Eq. (2.2) we obtain[8]

$$C_{\text{eff}} = \underbrace{(1-\alpha)C_G}_{C_{\text{geom}}} - \underbrace{\alpha\frac{\partial\langle\hat{Q}_i\rangle}{\partial V_G}}_{C_p}, \tag{2.9}$$

where we introduce the lever arm $\alpha = C_G/C_\Sigma$. In the limiting case that no electrons can jump between the quantum dots, i.e. $\partial Q_i/\partial V_G = 0$, this formula reduces to the usual addition formula of two capacitors in series, $C_{\text{geom}} = [C_G^{-1} + (C_\Sigma - C_G)^{-1}]^{-1}$.

[8] In this calculation, all off-diagonal elements of E_C have been neglected.

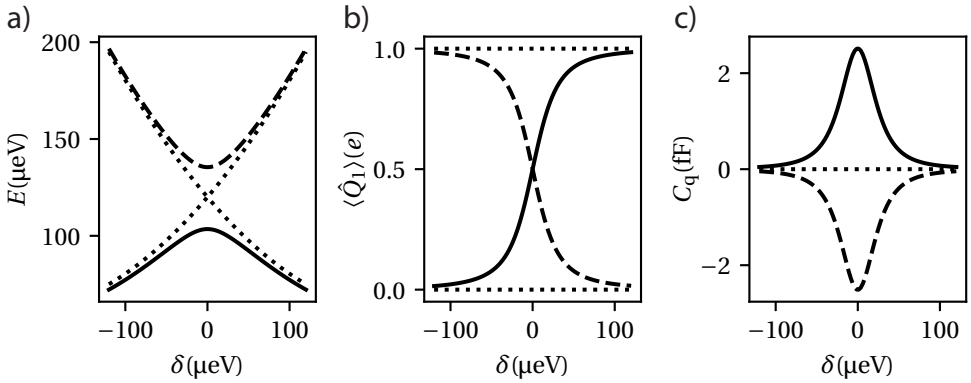


Figure 2.5: Calculation of the **a)** eigenenergies **b)** expectation value of charge and **c)** quantum capacitance as a function of detuning for the interdot transition of the double quantum. The ground and excited state are represented by a solid and dashed line, respectively, while the dotted line shows the case without tunnel coupling. For the calculations we assume $E_C = 120\,\mu\text{eV}$, $t_c = 16\,\mu\text{eV}$ and $\alpha = 1$.

Electron tunneling hence causes a correction to the geometric capacitance which is called the *parametric capacitance* C_p [66]. The electrostatic energy, specified in Eq. (2.4) is not enough to describe this behavior. In addition, electron tunneling must be taken into account explicitly since it causes charge hybridization between the different quantum dots. Its contribution to the Hamiltonian takes the form

$$\left(H_{\text{tun}}\right)_{ij} = t_c \left(|\vec{N} + \hat{e}_j\rangle \langle \vec{N} - \hat{e}_i| + \text{h.c.}\right). \tag{2.10}$$

It is this coupling that allows $\langle \hat{Q}_i \rangle$ to take nonquantized values.

For the double quantum dot, introduced in Sec. 2.1.3 the ground state expectation value $\langle \hat{Q}_1 \rangle$ is shown in Fig. 2.3. This expectation value changes smoothly when moving an electron between the quantum dots, known as the interdot transition, which is marked by the dashed line between the black and white marker in the same figure. In this system, the parametric capacitance can be calculated analytically by restricting the available charge states to the states $|(0,1)\rangle$ and $|(1,0)\rangle$ such that the Hamiltonian becomes two dimensional. The detuning $\delta = \mu_1((1,0)) - \mu_2((0,1))$ between the two quantum dots completely parametrizes the gate configuration of this transition. Writing the Hamiltonian in terms of the Pauli matrices σ_i yields

$$H = t_c \sigma_x + \frac{\delta}{2}\sigma_z \text{ and } H = \frac{\sigma_z}{2}\sqrt{4t_c^2 + \delta^2} = \frac{\Omega}{2}\sigma_z, \tag{2.11}$$

in the charge basis $\{|(0,1)\rangle, |(1,0)\rangle\}$ and eigenbasis $\{|-\rangle, |+\rangle\}$ respectively. The eigenbasis implicitly defines the energy splitting Ω. The eigenstates corresponding to the interdot transition are shown in Fig. 2.5a.

It is important to distinguish between two different contributions to the parametric capacitance. Firstly, the charge occupation of the quantum dot can change when the occupation probabilities of the ground and the excited state change, by phonon absorption or emission, for example. This leads to a contribution in the parametric capacitance

called *tunneling capacitance*. The main focus of this thesis, however, is the second contribution which is called the *quantum capacitance*. This results from a detuning dependent change in charge distribution in the eigenstates of the system, see Fig. 2.5b. For the ground state of a double quantum dot at zero detuning, the quantum capacitance can be calculated to be:

$$C_q = -\alpha \frac{\partial \delta}{\partial V_G} \frac{\partial}{\partial \delta} \langle -|\hat{Q}|-\rangle \Big|_{\delta=0} = \frac{\alpha^2 e^2}{4 t_c}. \tag{2.12}$$

An analogous calculation for the excited state yields the same result with the opposite sign. The quantum capacitance as a function of detuning is shown in Fig. 2.5c for both the ground state and the excited state. In conclusion, quantum capacitance is expected to take non-zero values when electrons tunnel between different quantum dots.

A convenient way to measure the parameteric capacitance is by coupling an *LC* resonator to the gate electrode. Its resonance frequency, ω will shift due to the additional contribution of the parameteric capacitance to the resonator capacitance C and can be approximated as[9]

$$\delta\omega = \frac{1}{\sqrt{L(C+C_p)}} - \frac{1}{\sqrt{LC}} \approx -\omega_0 \frac{C_p}{2C}. \tag{2.13}$$

The response of the resonator will be discussed in more detail in Sec. 2.2.

One of the major advantages of quantum capacitance measurements over transport measurements is that it allows measuring local properties in the sample. With transport measurements, only a complete cycle of tunneling events can be measured, see Sec. 2.1.3. In contrast, the quantum capacitance effect allows an isolated tunneling transition to be probed without involvement from the rest of the system. This also means, by extension, that we can use quantum capacitance to probe systems that do not have galvanically connected leads or where the leads are pinched off from the quantum dots. It can be a significant advantage to measure in this floating regime since it allows the probing of transitions which would be precluded by external electrons tunneling into the system. For example, in the case of a floating double quantum dot, only interdot transitions are possible, leading to a simplified charge stability diagram.

Using an RF excitation to measure the parametric capacitance can drive the quantum dot system from the ground state to the excited state. Since the excited state has the opposite quantum capacitance compared to the ground state, the resulting mixed state will have a smaller average quantum capacitance. The correction factor to Eq. (2.12) is $P_{|-\rangle} - P_{|+\rangle} = 1 - 2P_{|+\rangle}$ to compensate for the excited state probability $P_{|+\rangle}$. To estimate this probability, the oscillating potential on the gate is added to the Hamiltonian,

$$\delta \rightarrow \delta + 2\Omega_d \cos(\omega t) \text{ with } \Omega_d = \frac{\alpha e V_{RF}}{2\hbar}. \tag{2.14}$$

When the driving frequency ω is not much faster than the internal dynamics of the system like Ω, it cannot be transformed out of the problem by a rotating wave approximation. Instead, we can overestimate the excited state probability by assuming that the steady-state occupation is determined when the drive assumes its maximal value, i.e. $|\cos(\omega t)| = 1$. The idea being, that for the snapshots in time where $|\cos(\omega t)| < 1$, the

[9] Since C_{geom} and is constant, it can be included in the resonator capacitance C.

drive is too small to change the excited state probability significantly. With this approximation, the original ground state is no longer an eigenstate of the driven system, but evolves over time as $|\psi(t)\rangle = e^{\frac{-i}{\hbar}Ht}|-\rangle$ with $H = t_c\sigma_x + \Omega_d\sigma_z$ where we assume $\delta = 0$. The probability for the system to be in the excited state can then be calculated as

$$P_{|+\rangle} = \left|\langle +|\psi(t)\rangle\right|^2 = \frac{\Omega_d^2}{t_c^2+\Omega_d^2}\sin\left(\frac{t_c^2+\Omega_d^2}{\hbar}t\right)^2. \tag{2.15}$$

The time dependence of this equation is not accessible experimentally since it evolves on a timescale that is much faster than the readout. Therefore the relevant parameter for the experiment is the time-averaged value of $P_{|+\rangle}$ which takes the form

$$P_{|+\rangle} = \frac{1}{2}\frac{\Omega_d^2}{t_c^2+\Omega_d^2}. \tag{2.16}$$

2.1.6. SIMULATION OF CHARGE STABILITY DIAGRAMS

To predict the shape of charge stability diagrams from the underlying sample parameters, it is often more convenient to rely on numerical simulations rather than analytical derivations. As the goal is to aid experimental intuition, it is advantageous to minimize simulation times which means working with a model that is as simple as possible. Some parameters in the model are phenomenological and lack a microscopic derivation. As such, these simulations are a valuable tool to understand the structure of charge stability diagrams, but we do not expect all phenomena to be captured.

The systems considered in this section consist of an arbitrary number of quantum dots, interconnected by coupling terms between them. To write down a Hamiltonian for these systems, we must first define its basis vectors. The most convenient choice is the charge basis in which every charge configuration $\vec{N}$ defines a basis vector $|\vec{N}\rangle$.

The diagonal components of the Hamiltonian contain the contributions from the electrostatic energy and the effect of superconductivity. The electrostatic energy U_{el} was already found in Sec. 2.1.2. For these simulations, we will neglect the level energy $E_{i,l}$ however. Regarding superconductivity, in Sec. 2.1.4 we found an additional energy cost when the charge occupation of a superconducting quantum dot is odd. We will not concern ourselves with whether this state resides in the gap edge of the superconductor or in a subgap state below the gap edge. As such, we will denote the energy cost for an odd number of particles in dot j as Δ_j. This notation allows us to succinctly write the diagonal components of the Hamiltonian as:

$$H_{\vec{N}\vec{N}} = (\vec{N}-\vec{N}_g)E_C(\vec{N}-\vec{N}_g) + \sum_i \frac{1-(-1)^{\vec{N}_i}}{2}\Delta_i. \tag{2.17}$$

As we saw in Sec. 2.1.5, tunnel coupling is an essential ingredient for quantum capacitance. To model the resonator response, we must add tunnel coupling terms to the Hamiltonian, where it shows up as off-diagonal elements. We investigate both $1e$ and $2e$ coupling terms which for any two quantum dots i and j leads to the terms

$$t_{ij}^{1e}|\vec{N}+\hat{e}_i\rangle\langle\vec{N}-\hat{e}_j| \text{ and } t_{ij}^{2e}|\vec{N}+2\hat{e}_i\rangle\langle\vec{N}-2\hat{e}_j| \text{ for all } \vec{N}. \tag{2.18}$$

For most simulations in this thesis, only $1e$ tunneling is used, and $2e$ tunneling is further discussed in Chapter 5. The tunnel coupling terms also change the charge plateaus in the charge stability diagram. This effect can clearly be observed in Fig. 2.3 —calculated using the methods described in this section— where the expectation value of charge does not align with the lines resulting from electrostatical calculations.

Given the Hamiltonian, all quantities of interest can be calculated by finding the corresponding eigenenergies and eigenstates. To numerically diagonalize the Hamiltonian, we explicitly calculate its components given by Eq. (2.17) and Eq. (2.18) for a definite set of charge states. The expansion of the Hamiltonian over the relevant charge states can conveniently be done using Kwant [67].

Since diagonalizing matrices is computationally expensive for larger matrices, the number of charge states must be restricted as much as possible. Typically only a few charge states contribute significantly to the lowest energy solution of the Hamiltonian. The specific charge configuration for the relevant charge states depends on the gate configuration of the quantum dots. For different points in the charge stability diagram, different charge states must be taken into account. Rather than including all relevant charge states in the Hamiltonian, it is more efficient to recalculate the relevant charge states for every gate configuration. In practice, the charge state $|\vec{N}^*\rangle$ that minimizes Eq. (2.17) can be found efficiently. The Hamiltonian is subsequently expanded over all states that differ only a few electrons from $|\vec{N}^*\rangle$.

Given all eigenenergies E_k and eigenstates $|\psi_k\rangle$, we can calculate all quantities of interest. First, we calculate the quantities we have seen so far in this chapter. Specifically we find the energy splitting $\Omega = E_1 - E_0$ and expectation value of charge $\langle \hat{Q}_i \rangle = e\langle\psi_0|\hat{N}_i|\psi_0\rangle$ where the operator $\hat{N}_i$ is diagonal since we are working in the charge basis. In Sec. 2.2.3 we will also find it convenient to calculate quantum dot coupling to the resonator from the numerical results. Specifically, we will need the matrix elements $\langle\psi_k|\hat{N}_i|\psi_l\rangle$.

A big advantage of the simulations described above is the ability to tune parameters that are inaccessible in experiments. Although parameters like the charging energy can change slightly over the course of an experiment due to the electrostatic environment, tuning charging energy independently is only possible in theory. Secondly, the simplified model with few charge states provides fast feedback between setting the parameter regime and simulation result. Therefore the work described in this section has proven to be indispensable for identifying charge transitions and guiding experimental measurements, especially for Chapter 5 and Chapter 7.

2.2. RESONATORS

2.2.1. INTRODUCTION

High-frequency measurements, and resonators in particular, form the second theme of this theory chapter. Together with the discussion on quantum dots in Sec. 2.1, the theory explicated in this section forms the central framework in which the core results of this thesis are interpreted. Indeed, most of the experimental results contained in this thesis involve high-frequency resonators coupled to quantum dot systems. The practicality of resonators was already alluded to in Sec. 2.1.5, where the resonance frequency of a

resonator is shown to depend on changes in electron occupation in the quantum dot system. In this section, we wish to expand on this description to obtain a more quantitative understanding of the resonator response.

Describing the resonance shift by parametric capacitance effectively treats the resonator and quantum dots as separate subsystems. Whenever the detuning between the resonator and the excitation frequency becomes small, however, the two systems will hybridize, precluding such separation. Therefore we will treat the resonator together with the quantum dots as a single quantum mechanical system. To achieve this goal, we will first describe the resonator in the quantum mechanical framework of input/output theory in Sec. 2.2.2. Subsequently, in Sec. 2.2.3, we describe how the coupling to a quantum dot system can be described in this framework. The combination of these two descriptions yields an explicit formula for the resonator response measured in reflectometry, detailed in Sec. 2.2.4. There, we also show how this formula can be adapted for resonators coupled to a central feedline.

Finally, experimentally, the frequency-dependent response of the resonator is often observed to be very asymmetric with respect to the resonance frequency. The input/output model itself does not predict any asymmetric line shapes. Hence, we conclude by explaining how these asymmetries can result from impedance mismatches in the measurement circuit.

There already exists a vast amount of literature on the subjects treated in this section which therefore merely serves to combine the relevant derivations in one place. As such, many details will be glossed over to keep this section as concise as possible, while still providing the necessary details for understanding resonator measurements.

2.2.2. INPUT/OUTPUT THEORY

The study of the interaction between light and an atom in a cavity is called cavity quantum electrodynamics (CQED). Input/output theory conveniently describes the interaction of open systems to a thermal bath, including these optical systems. This theory lends itself well to the study of artificial atoms —such as quantum dots— in one-dimensional resonator cavities, which is then called circuit quantum electrodynamics (cQED). Here, we will follow Refs. [68–71] to derive the behavior of the resonators used in this thesis.

Rather than stating the full Hamiltonian of the system, we first consider a resonator with bare resonator frequency ω_0, which for a single mode is described by the Hamiltonian:

$$H_{\text{res}} = \hbar\omega_0 \left(a^\dagger a + \frac{1}{2} \right). \tag{2.19}$$

Here, the operators $a^\dagger$ and a create and annihilate a photonic excitation in the resonator, respectively. The behavior of a cavity is most easily understood in the Heisenberg picture of quantum mechanics, where the operators rather than the states are time-dependent. The dynamics of the photon annihilation operator $a(t)$ is determined by Heisenberg's form for the equation of motion [72]:

$$\partial_t a(t) = -\frac{\imath}{\hbar}[a(t), H_{\text{res}}] = -\imath\omega_0 a(t). \tag{2.20}$$

In the remainder of this chapter, we will often suppress the explicit time dependence for brevity. We will also perform Fourier transforms of the operators as needed, denoting the Fourier transform of the operator $c(t)$ by $\tilde{c}(\omega)$ to avoid confusion.

In reality, the system will always be coupled to a continuum of states that live outside of the resonator, resulting in more interesting behavior than exhibited by the isolated system. Firstly, to drive the resonator and probe its response, the resonator is coupled to an input line, capable of supporting photonic modes with any frequency. Photonic excitations in the cavity can also be lost to the environment, which adds a similar contribution to the Hamiltonian. We will study these additive contributions to Eq. (2.19) independently from the contributions added by the quantum dot system described in the next section.

To describe the bath of states that couples to the resonator, we introduce the operator $b_\omega^\dagger$ to create an excitation with energy $\hbar\omega$ in the bath system. The resonator couples to each of these modes individually, with a coupling strength κ, which we assume to be frequency independent. This is called the Markov approximation and is accurate in the relevant bandwidth of the problem. The additive contribution to the Hamiltonian in Eq. (2.19) is then given by

$$H_{\text{bath}} = \int_{-\infty}^{\infty} \mathrm{d}\omega \left[\hbar\omega b_\omega^\dagger b_\omega + \hbar\sqrt{\frac{\kappa}{2\pi}} \left(b_\omega^\dagger a + a^\dagger b_\omega \right) \right]. \tag{2.21}$$

Before determining the contribution of this Hamiltonian to the time evolution of a, we must first calculate the time evolution of b_ω. To this end, we can derive the following differential equation for the time evolution of b_ω as[10]

$$\partial_t \left(b_\omega e^{\imath\omega t} \right) = -\imath \sqrt{\frac{\kappa}{2\pi}} a e^{\imath\omega t}. \tag{2.22}$$

The solution for b_ω is now given by straightforward integration of both sides of the equation over time[11], together with a boundary condition for the differential equation. Two different boundary conditions can be formulated for this differential equation, either specifying the initial or final configuration of b_ω. Specifically, we can either take the input frequency spectrum $\imath b_\omega(t_0) = \tilde{a}_{\text{in}}(\omega)$ with $t_0 < t$, before any interaction takes place, as the boundary condition. On the other hand, we can use the output frequency spectrum as boundary condition, $\imath b_\omega(t_1) = \tilde{a}_{\text{out}}(\omega)$ with $t < t_1$. The differential equation together with either of the boundary conditions yields the full solution for b_ω. This solution allows us to write the contribution of the bath states to the time evolution of a (Eq. (2.20)) as[12]

$$-\frac{\imath}{\hbar}[a, H_{\text{bath}}] = -\sqrt{\kappa} a_{\text{in}}(t) - \frac{\kappa}{2} a = -\sqrt{\kappa} a_{\text{out}}(t) + \frac{\kappa}{2} a. \tag{2.23}$$

[10] This equation can be verified by performing the time derivative on the left-hand side, keeping in mind that $\partial_t b_\omega = -\frac{\imath}{\hbar}[b_\omega, H_{\text{bath}}]$, similar to eq. (2.20).

[11] Note that to obtain an expression for b_ω, we only need to solve the integral on the left-hand side explicitly for now. This is easily accomplished since the left-hand side is already written as a derivative to time.

[12] The equation follows by substituting the solution of b_ω into the commutator $[a, H_{\text{bath}}]$ and subsequently calculating the remaining integrals.

As mentioned before, this derivation serves to describe two distinct contributions. First, to describe the relation between the input and output field of the resonator, but also to account for excitations lost from the cavity into the environment. These lost excitations are not accessible by any measurement on the output field, or equivalently, a_{out} is not known. However, by assuming that no excitations from the environment enter into the cavity, i.e. $a_{\text{in}} = 0$, we can take this loss effect into account. The explicit form of the contribution to the time evolution of a is given by $\frac{\kappa_{\text{d}}}{2} a$, where κ_{d} denotes the coupling strength to the environmental loss modes.

The response of a bare resonator can be found by calculating $\tilde{a}_{\text{out}}/\tilde{a}_{\text{in}}$. Before doing this in practice in Sec. 2.2.4, we will first study the contribution of a quantum dot in the next section.

2.2.3. QUANTUM DOT COUPLING

The oscillating voltage in a resonator interacts with the charge in the quantum dot it is coupled to. The Hamiltonian corresponding to this interaction is given by the combination of the electrostatic energy, given in Eq. (2.4) and the tunneling Hamiltonian given in Eq. (2.10). The oscillating gate voltage can be included by replacing $V_{\text{G}} \mapsto V_{\text{rms}}(a^\dagger + a)$ [73]. Many different energy levels can contribute to the resonator response simultaneously, but here we will only consider the case of a single transition between two discrete energy levels. The Hamiltonian coupling the quantum dots to the resonator can be written as

$$H_{\text{q}} = \frac{\hbar\Omega}{2}\sigma_z + 2\hat{N}_i E_{\text{C}} \frac{C_{\text{G}}}{e} V_{\text{rms}}(a^\dagger + a), \tag{2.24}$$

assuming E_{C} is a diagonal matrix and that the resonator only couples to dot i with a capacitance of C_{G}. We expand $\hat{N}_i$ in the eigenbasis, see Sec. 2.1.5, to obtain

$$H_{\text{q}} = \frac{\hbar\Omega}{2}\sigma_z + \hbar\left(g_{\text{eff}}\sigma_- a^\dagger + g_{\text{eff}}^*\sigma_+ a\right) \tag{2.25}$$

with $g_{\text{eff}} = \frac{\alpha e}{\hbar} V_{\text{rms}} \langle - | \hat{N}_i | + \rangle$. In this derivation, we have dropped terms that do not conserve energy, $\sigma_+ a^\dagger$ and $\sigma_- a$, where σ_+ and σ_- denote the raising and lowering operators of the quantum dot in its eigenbasis.

Similar to adding the bath modes to the system, we must solve the time evolution of the quantum dot system before we can calculate the contribution to the time evolution of a. We are again interested in the time evolution of the relevant annihilation operator, in this case of an excitation in the quantum dot system, σ_-. Excitations in the quantum dot can also be lost to the environment, so before solving for σ_-, we couple the quantum dot excitations to environmental modes with coupling γ. The Heisenberg equation of motion for σ_- is then given by

$$\partial_t \sigma_- = -\imath\Omega\sigma_- + \imath g_{\text{eff}}^* \sigma_z a + \sigma_z \frac{\gamma}{2}\sigma_-. \tag{2.26}$$

We assume that the excited state occupation is fully determined by thermal excitations and does not depend on the probe tone. As such we can replace $\sigma_z \mapsto \langle\sigma_z\rangle = p_+ - p_-$ where the thermal probabilities are given by

$$p_i = \frac{e^{-\hbar\omega_i/k_{\text{B}}T}}{\sum_n e^{-\hbar\omega_n/k_{\text{B}}T}} \text{ s.t. } \langle\sigma_z\rangle = \tanh\left(\frac{\hbar\Omega}{2k_{\text{B}}T}\right). \tag{2.27}$$

The factor $\langle\sigma_z\rangle$ does not depend on time, by the same assumption. This means Eq. (2.26) can be solved for $\tilde{\sigma}_-(\omega)$ yielding

$$\tilde{\sigma}_-(\omega) = \chi(\omega)\tilde{a}(\omega) \text{ with } \chi(\omega) = \frac{g_{\text{eff}}^*\langle\sigma_z\rangle}{\Omega - \omega + \langle\sigma_z\rangle\imath\frac{\gamma}{2}}. \tag{2.28}$$

Now that the behavior of the quantum dot is fully determined in terms of a, its contribution to the time evolution of a can be calculated in the usual way

$$-\frac{\imath}{\hbar}[a, H_{\text{q}}] = -\imath g_{\text{eff}}\sigma_-. \tag{2.29}$$

For a double quantum dot, the off-diagonal elements of $\hat{N}$ can be calculated explicitly. Using the notation from Eq.(2.11) we find

$$g_{\text{eff}} = \frac{\alpha e t_{\text{c}}}{\hbar\Omega} V_{\text{rms}}. \tag{2.30}$$

For more complicated quantum dot geometries, it is also possible to use the simulations detailed in Sec. 2.1.6 to find the appropriate value for g_{eff} using the matrix elements $\langle\psi_k|\hat{N}_i|\psi_l\rangle$.

2.2.4. RESONATOR RESPONSE

The response of the resonator is encoded in the relation between the input and output field, a_{in} and a_{out}. This relation is conveniently represented by Eq. (2.23) which can be rewritten as the input-output relation:

$$a_{\text{out}} - a_{\text{in}} = \sqrt{\kappa}a. \tag{2.31}$$

Indeed, this equation predicts $\tilde{a}_{\text{out}}/\tilde{a}_{\text{in}} = 1$ when there is no coupling to a cavity. For finite coupling κ, the output field $\tilde{a}_{\text{out}}$ can be calculated by combining all contributions to $\partial_t a = -\frac{\imath}{\hbar}[a, H]$ and solving for $\tilde{a}_{\text{out}}$. The exact form of the resulting Hamiltonian depends on the resonator architecture, where we distinguish between reflectometry and resonators hanging of a central feedline.

The first case we calculate here is a single resonator measured in reflection. This means the components in the Hamiltonian include coupling from the cavity to the input and output fields with coupling strength κ, a coupling to an environmental loss bath with coupling strength κ_{d} and coupling to a quantum dot. Finally, the quantum dot system itself can also decay into the environment with coupling strength γ. All components to the Hamiltonian are schematically represented in Fig. 2.6a and leads to the following equation for $\tilde{a}_{\text{out}}$:

$$\sqrt{\kappa}\tilde{a}_{\text{out}}(\omega) = \imath\omega\tilde{a}(\omega) - \imath\omega_0\tilde{a}(\omega) + \frac{\kappa}{2}\tilde{a}(\omega) - \frac{\kappa_{\text{d}}}{2}\tilde{a}(\omega) - \imath g_{\text{eff}}\chi(\omega)\tilde{a}(\omega). \tag{2.32}$$

Together with Eq. (2.31), this yields our final result for the resonator response measured in reflection

$$\frac{\tilde{a}_{\text{out}}}{\tilde{a}_{\text{in}}} = 1 + \frac{\kappa}{\imath(\omega - \omega_0) - \frac{\kappa+\kappa_{\text{d}}}{2} - \imath g_{\text{eff}}\chi(\omega)}. \tag{2.33}$$

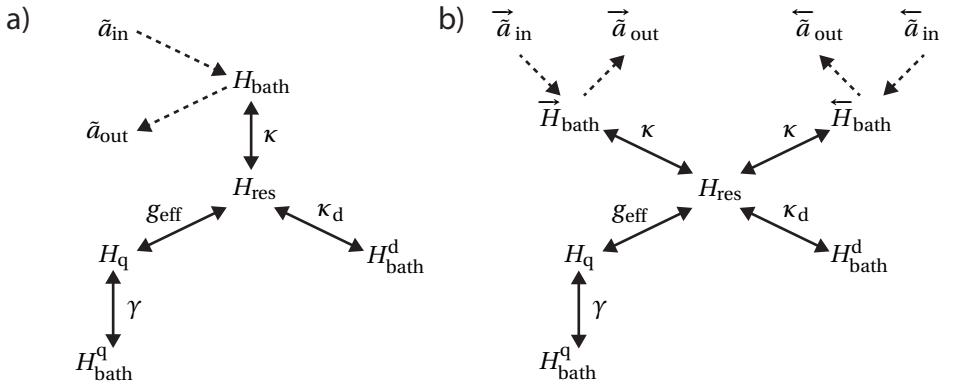


Figure 2.6: Schematic representation of the Hamiltonian describing the resonator response **a**) in reflection and **b**) in the hanger geometry. The bath Hamiltonians have been given different indices to signify they represent distinct environmental modes. Solid arrows represent coupling between different parts of the Hamiltonian, while the dashed arrows represent the relevant input and output modes.

The second geometry we consider is that of a central feedline, with resonators hanging off the feedline, shown schematically in Fig. 2.7b. This means that photons coming from the resonator can either go left or right in the feedline, such that half of the output information will be lost. We incorporate this into the input/output theory by representing the feedline as two separate baths of environmental modes. The first bath, $\overleftarrow{H}_{\text{bath}}$ describes photons moving left, while the second, $\overrightarrow{H}_{\text{bath}}$ describes photons moving right. The remainder of the geometry is the same as for the reflectometry case, where we also assume the input field of photons moving in the reverse direction is negligible. This case is schematically represented in Fig. 2.6b. The resulting contributions can be calculated directly from $[a, H]$, but the derivation is analogous to the derivation of Eq. (2.33). Therefore, we can obtain our result in the hanger geometry by making two substitutions to Eq. (2.33). First, since photons moving in the reverse direction in the feedline will not contribute to $\overrightarrow{\tilde{a}}_{\text{out}}$ —analogous to the environmental modes represented by κ_{d}— we can take this loss into account by substituting $\kappa_{\text{d}} \mapsto \kappa_{\text{d}} + \kappa$. Second, because the resonator couples to two output baths, we relabel $\kappa \mapsto \frac{1}{2}\kappa_{\text{ext}}$ to obtain

$$\frac{\overrightarrow{\tilde{a}}_{\text{out}}}{\overrightarrow{\tilde{a}}_{\text{in}}} = 1 + \frac{1}{2}\frac{\kappa_{\text{ext}}}{\imath(\omega - \omega_0) - \frac{\kappa_{\text{ext}}+\kappa_{\text{d}}}{2} - \imath g_{\text{eff}}\chi(\omega)}. \tag{2.34}$$

2.2.5. RESONATOR ASYMMETRY

In this section, we focus on the response of the bare resonator without any coupling to the quantum dot system. Within input/output theory, this is accomplished by removing the $\imath g_{\text{eff}}\chi(\omega)$ term. Tuning the quantum dots into Coulomb blockade approximates the same effect in an experimental setting. In this regime, all transitions are far detuned from the resonator frequency, such that $\Omega \to \infty$ and $\chi \to 0$. The line shape of the bare resonator response $|\tilde{a}_{\text{out}}/\tilde{a}_{\text{in}}|$, as calculated from Eq. (2.33) and Eq. (2.34), is symmetric with respect to $\omega - \omega_0$. This is not the case, however, in many experimental measurements of

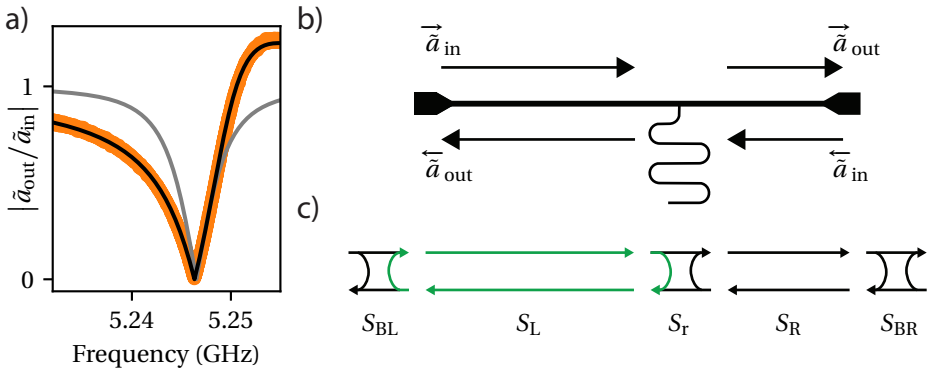


Figure 2.7: **a**) Experimental measurement of an asymmetric resonator response in the hanger geometry. A fit with Eq. (2.34) is shown by the gray line. The black line shows a fit that allows complex-valued coupling factors to reflect impedance mismatches in the feedline, $\kappa_{ext}/(2\pi) = (8-5\imath)$ MHz. **b**) Schematic of a resonator in the hanger geometry. As indicated in the figure, the left and right moving photons are represented by separate input and output fields. **c**) Schematic of the S-matrices describing the signal flow through the feedline. The reflections caused by the resonator and bondwires, represented by the S matrices S_r, S_{BL} and S_{BR} respectively, cause standing waves between them. One such possible cycle of reflections is highlighted in green.

this line shape. An archetypical example of this effect is shown in Fig. 2.7a.

Many experiments described in this thesis depend on quantifying the resonator response by fitting them with Eq. (2.33) or Eq. (2.34). Therefore, our model must be corrected to account for the asymmetric resonator line shapes. Non-idealities in the measurement circuit such as reflection at the bondwires and induction in the feedline can explain the observed asymmetry [74, 75]. Here, we investigate the first explanation: the impedance mismatch in the RF lines, in detail following [76]. The feedline on the sample is bonded to the PCB (see Fig. 3.1c and Fig. 3.1e), which is in turn connected to the RF lines in the cryostat. It is very likely, however, that these bondwires are not completely impedance matched, which will cause reflections in the RF circuit. We model the result of such impedance mismatches in the remainder of this section.

Since there are multiple reflection points in the RF circuit, standing waves can form in between them, which is schematically depicted in Fig. 2.7c. These standing waves influence the response of the circuit as a whole. To make this more explicit, whenever combining two scattering-matrices, S' and S'' into S, every possible path must be taken into account, including an arbitrary number of bounces between the two S-matrices. For S_{21} the contributions add up to

$$S_{21} = \sum_{n=0}^{\infty} S''_{21}(S'_{22}S''_{11})^n S'_{21} = \frac{S''_{21}S'_{21}}{1 - S'_{22}S''_{11}}. \tag{2.35}$$

The other elements can be calculated similarly.

To model the situation of impedance mismatches resulting from the bondwires, we define five S-matrices, see Fig. 2.7c. The frequency range of interest is small compared to the resonance frequency and length scales of the sample. Therefore we assume that only the S-matrix for the resonator hanging of the feedline depends on frequency. It takes the

form[13]:

$$S_\mathrm{r} = \begin{pmatrix} \Gamma_\mathrm{r} & 1+\Gamma_\mathrm{r} \\ 1+\Gamma_\mathrm{r} & \Gamma_\mathrm{r} \end{pmatrix} \text{ with } \Gamma_\mathrm{r} = \frac{1}{2} \frac{\kappa_\mathrm{ext}}{\imath(\omega-\omega_0) - \frac{\kappa_\mathrm{ext}+\kappa_\mathrm{d}}{2}}. \tag{2.36}$$

We represent the S-matrices for the two bondwires by S_BL and S_BR whose elements remain unspecified but constant. The feedline elements left and right of the resonator cause the signal to rotate in the complex plane over an angle ϕ_L and ϕ_R respectively, which can be written as

$$S_{L/R} = \begin{pmatrix} 0 & e^{\imath\phi_\mathrm{L/R}} \\ e^{\imath\phi_\mathrm{L/R}} & 0 \end{pmatrix}. \tag{2.37}$$

Using either the viewpoint of multiple reflections, S_{21} of the combined system can now calculated to be

$$S_{21} = v \frac{1+\Gamma_\mathrm{r}}{1+u\Gamma_\mathrm{r}}. \tag{2.38}$$

The complex constants u and v depend on the phase delays ϕ_L and ϕ_R and the components of S_BL and S_BR. We are not interested in the constant v since it enters as a constant scaling of the RF signal. After using the definition of Γ_r from Eq. (2.36) the result can be written as

$$S_{21} = 1 + \frac{1}{2} \frac{(1-u)\kappa_\mathrm{ext}}{\imath(\omega-\omega_0) - \frac{(1-u)\kappa_\mathrm{ext}+\kappa_\mathrm{d}}{2}}. \tag{2.39}$$

In other words, the asymmetric resonator line shapes can be represented by letting κ_ext range over the complex numbers instead of restricting it to the real numbers. This allows fitting the experimental resonator response faithfully, as shown in Fig. 2.7a.

[13] Strictly speaking we have not derived the S_{11} component, but the calculation is analogous to that of Eq. (2.34). The components S_{12} and S_{22} follow from symmetry.

3

EXPERIMENTAL METHODS

In physics, you don't have to go around making trouble for yourself —
nature does it for you.

Frank Wilczek [77]

The quality of experimental data depends on the performance of two equally important elements, sample fabrication and the measurement setup. In both cases, details are of vital importance and this chapter aims to describe them.

3.1. SAMPLE FABRICATION

3.1.1. RESONATORS

Since resonators are a crucial component for gate-based sensing, we begin by describing the two different types of resonators that are used in this thesis. First, the resonators used in Chapter 4 and Chapter 5 are fabricated on separate resonator chips. These resonator chips consist of inductors ranging from 40 nH to 420 nH and are provided by the group of David Reilly [78]. Each inductor is connected to an individual RF contact via a coupling capacitor. The individual addressability enables the multiplexing of the different resonators, allowing for reflection based readout. An individual bias-T per resonator allows the application of DC voltages to the connected gate electrodes. This connection between the multiplexing circuits and the gate electrode is established via a wire bond, as shown in Fig. 3.1a and Fig. 3.1d. The resonator chip is glued on top of the sample circumventing the need for dicing the sample[1], see Sec 3.1.3.

Parasitic capacitance together with the inductors constitute *LC* resonators. The exact value for the parasitic capacitance is not fixed but depends on specifics such as the capacitance between the bondwire and ground. In practice, the value is approximately

[1] The current size of the quantum dot chip can be processed without any special measures like carrier chips.

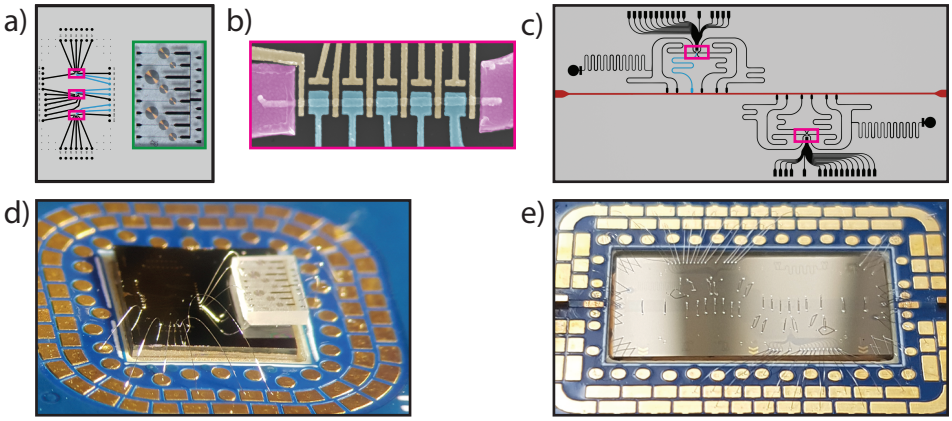


Figure 3.1: **a**) Representative chip design for the UHF experiments. The leads connecting to the dispersive sensing gates are shown in blue and have their bond pads in the middle of the chip. This enables bonding them to the separate resonator chip outlined in green. **b**) A representative SEM image of a quantum dot device. The source and drain electrodes are shown in purple while the side gates and tunnel gates are shown in yellow. The gates used for dispersive sensing are shown in blue. **c**) Schematic chip design for the SHF experiments. The feedline is shown in red and one of the resonators is shown in blue. **d**), **e**) Photo showing bonds from the chip to the PCB corresponding to the designs in **a**) and **c**).

$C \approx 0.3\,\mathrm{pF}$. The LC resonators have a resonance frequency given by

$$2\pi f_\mathrm{r} = \frac{1}{\sqrt{LC}} \tag{3.1}$$

which yields frequencies between 400 MHz and 1500 MHz in our implementation. Radio frequencies in this regime are known as *ultra high frequency* (UHF).

In contrast, the samples described in Chapter 6 and Chapter 7 use resonators that are fabricated on the sample chip itself, see Fig. 3.1c. On-chip fabrication prohibits reusing the resonators, but it enables a bespoke resonator design for every application. This is an advantage for dispersive gate sensing where the optimal resonator design depends on the quantum dot system it is coupled to. For example, the optimal coupling factor of the resonator to the feedline, κ_ext, depends on $\delta\omega$, the expected frequency shift[2].

The resonators are implemented using a half-wavelength superconducting coplanar waveguide (CPW). One end is connected to the feedline with a coupling capacitor determining κ_ext. The other end of the CPW is connected to the quantum dot system to either a gate electrode or source contact. Compared to the off-chip resonators, these resonators are designed to operate at a higher frequency, between 3 GHz and 7 GHz. This frequency regime is known as the *super high frequency* (SHF) regime.

The quantum dot samples are fabricated on an intrinsic silicon wafer covered with a 20 nm LPCVD SiN_x layer. Fabrication then starts by sputtering a 20 nm NbTiN layer. The

[2] Specifically, the value is given by $\kappa_\mathrm{ext} = \sqrt[3]{4\delta\omega^2\kappa_\mathrm{d}}$, where κ_d denotes the internal cavity decay rate. This expression is obtained by maximizing the difference between Eq. (2.34) on resonance and for large detuning. We assume that κ_d is small. Furthermore, we neglect $\mathrm{Im}(g_\mathrm{eff}\chi)$, which is (only) a good approximation in the dispersive regime.

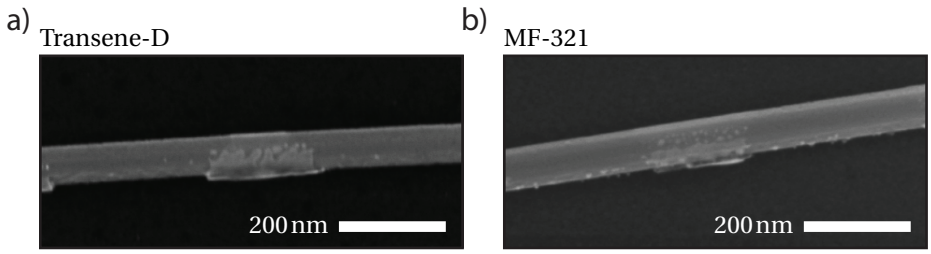


Figure 3.2: **a**) Result of etching with Transene-D. **b**) Etching with MF-321 leaves clear residu on the etched part of the nanowire which is assumed to be AlO_x.

resonator design is patterned with electron beam lithography (EBL). To ensure magnetic field compatibility of the resonators, holes are simultaneously patterned in the ground plane and CPW structures to pin any vortices created by the magnetic field [79]. This pattern is subsequently etched by reactive ion etching (RIE) in an SF_6/O_2 atmosphere. Finally, before continuing to the nanowire fabrication, the sample is diced to 14.5 mm × 6.5 mm, which precisely fits the sample cavity of the printed circuit board (PCB) which connects the sample to the measurement setup, see Fig. 3.1e. It is essential to perform the dicing step before nanowire deposition to prevent damage related to electrostatic discharge (ESD), see Sec. 3.1.3.

3.1.2. NANOWIRE BASED QUANTUM DOTS

At the core of every sample described in this thesis is a semiconductor InAs nanowire grown with Molecular beam epitaxy (MBE). The nanowires are provided by the group of Peter Krogstrup [80]. The superconducting Al shell, relevant for Chapter 5 and Chapter 7, is subsequently evaporated in situ on two facets of the nanowire. This results in a clean and epitaxial interface between the InAs and the Al. More details on the fabrication recipe are given in Appendix A.

Before depositing nanowires on the sample, its surface is cleaned in acetone using an ultrasound bath. Even though we only need limited precision for the initial placement of the nanowire, it is essential that the nanowire sticks to ensure alignment between the different fabrication steps. An additional a plasma descum can improve nanowire adherence and prevent it moving after deposition on the sample surface. However, the O_2 plasma makes the SiN_x surface of the sample hydrophilic and can create problems with resist adhesion which is especially important when etching the superconducting shell [81]. Due to this downside, the descum is only applied in Chapter 6 and device B described in Chapter 7.

After the surface is prepared, a single nanowire is picked up from their growth chip and transferred to the sample using a micro-manipulator. Since there are no fine features to align the nanowire to, it is not necessary to move the nanowire once it is on the sample, preventing any damage to the wire. The remainder of the sample design is based on optical microscope images of the nanowire. Optical images provide sufficient detail to accurately determine the nanowire position without resorting to scanning electron microscope (SEM) techniques (see Sec. 3.1.3).

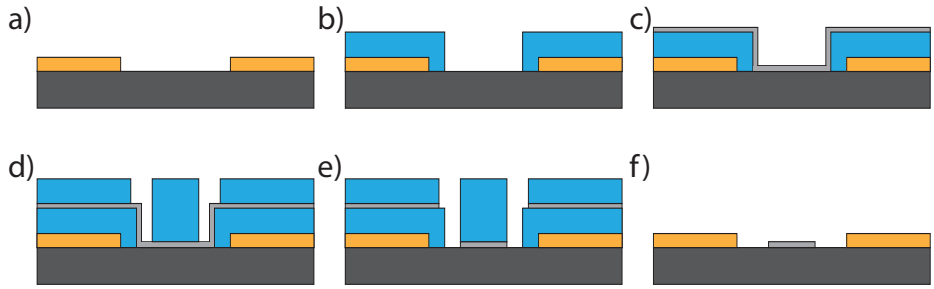


Figure 3.3: Schematic illustration of the fabrication of a local gate dielectric. **a**) Substrate in dark gray with resonators in orange. **b**) A liftoff resist mask (blue) is patterned. **c**) The dielectric is deposited (light gray). **d**) A second resist mask (blue) is put on top and patterned. **e**) The exposed dielectric is etched. **f**) All resist is removed from the sample.

Now, an etch mask can be created on the sample to etch away the Al shell to define regions of the wire without induced superconductivity. The wet etch is performed with either Transene-D or MF-321. The advantage of the former is a more complete etch of the Al, but in SEM images, damage to the underlaying nanowire can be observed. In contrast, the room temperature MF-321 etching rate is significantly slower than Transene-D and leaves small droplets of AlO_x behind. However, no damage to the semiconducting wire was observed, see Fig. 3.2. To prevent etchant creeping under the resist mask that causes overetching, an adhesion promotor like HDMS is used for all samples subjected to the plasma descum. It is of vital importance to remove the etch mask immediately after the etching process to prevent significant overetching[3].

Next, ohmic contacts to the nanowire are made. We remove the native oxide of the InAs using 30 s of Argon milling. Without breaking vacuum, we deposit a sticking layer of 10 nm Ti followed by a 150 nm Au layer.

To obtain a large quantum capacitance, a large lever arm (viz. capacitance) from the gate structure to the nanowire is essential. For that reason, fabricating a thin dielectric with high dielectric constant is beneficial. Therefore we deposit AlO_x via atomic layer deposition (ALD) at 105 °C to form a dielectric layer of approximately 10 nm. For samples using off-chip resonators, this dielectric layer is sufficiently thin that it can be punctured reliably during the bonding process. This allows for a global deposition of the dielectric, covering the pads that later will be bonded to. For on-chip resonators however, care must be taken to allow connecting the top gates to the resonators, unobstructed by the ALD layer. Hence, we deposit the dielectric locally on the sample which has the added benefit that the resonators will not come into contact with the dielectric. The liftoff process of an ALD layer can result in large standing edges in the dielectric since the ALD layer does not tear easily at the liftoff mask. Instead we follow the process schematically depicted in Fig. 3.3. Crucially, a second layer of resist is applied on top of the ALD layer, and an etch mask is exposed along the liftoff mask, where the AlO_x is etched away using 4 minutes of MF-321 etch. Subsequently, both resist layers are removed which results in a sharply

[3] Tiny amounts of etchant can remain behind after transferring the sample through multiple stages of H_2O. Only by removing the entire etch mask can all etchant be removed.

defined ALD pattern at the cost of an additional lithography step.

The final step in the sample fabrication is the deposition of top gates. Similar to the ohmic contacts, we evaporate a 10 nm/150 nm Ti/Au layer. This time, however, the total thickness of the layer is critical and must be on the order of the nanowire thickness. When the deposited layer is too thin, the gates over the wire will not be continuous which drastically reduces the lever arms of the gates. On the other hand, if the layers reach the same height as the resist thickness, the different gates can short together and inhibit the liftoff process. A representative SEM image of the finished quantum dot fabrication is shown in Fig. 3.1b. More margin for the thickness can be obtained by using multiple angle evaporation [82], thereby allowing thinner gate structures, but this is not pursued in this thesis.

3.1.3. ELECTROSTATIC DISCHARGE PREVENTION

The fabricated nanowire devices are very sensitive to electrostatic discharge (ESD). ESD causes a large current to flow through the device, similar to lightning, which can destroy the nanowire, or break down the dielectric between the nanowire and the gate structure. A destroyed nanowire is usually easy to identify with an SEM, as it either shows up as lack of uniformity or even total disintegration. A breakdown of the dielectric is less visible but often results in a short circuit between one of the gates and the ohmic contacts[4]. The latter mechanism was the most prevalent when fabricating samples similar to those described in this thesis, which we therefore describe in more detail.

The voltage difference at which a dielectric becomes conducting is known as the breakdown voltage. Exceeding the breakdown voltage can create a permanently conductive channel in the dielectric rendering the device unusable. Even when no short is created, the electric field can create charge traps in the dielectric which in turn deteriorate the stability of the gate dielectric [83]. Initial characterization of the device does not reveal the presence of these charge traps. Charge traps are however linked to hysteresis in the pinch-off measurements of the nanowire. The exact voltage at which the dielectric breaks down depends on the exact details of the ALD process such as temperature and thickness. For the devices described in this thesis we expect the dielectric to break down between 4 V and 7 V [84, 85].

To protect the sample from ESD related damage, charge accumulation must be prevented as well as safely discharging any remaining accumulated charge. Here, we focus on preventing charge accumulation, a good starting point for which is given in Ref. [86]. Firstly, we have not found a reliable way to dice our samples without causing shorted gates. Depositing a thin metal layer on top of the dicing resist, shorting all device leads nor fabricating metal barriers surrounding the device showed any beneficial effects. Furthermore, substituting dicing for cleaving did not noticeably improve the amount of shorted gates. Dicing the samples before nanowire deposition made a stark difference however, which is why we do not dice any of our samples after nanowires have been deposited.

The samples are always transported in antistatic bags, also in the cleanroom. As much as possible, the sample is only taken out of the antistatic bags in ESD-safe environments. Specifically, many flooring materials induce electrostatic charge and should

[4] The resistance of such a 'short' is typically on the order of 1 MΩ.

be avoided. A charge detector helps to identify such ESD unsafe environments.

Unfortunately, the PCB used when bonding samples has no inherent shorting or grounding mechanism for the sample. Rather than transporting the bonded sample in a floating PCB, the PCB is first mounted on the fridge puck. Shorting the electrodes together is especially important after the electrodes are extended by the bonds, since electric field gradients induce more charge accumulation for longer electrodes. The puck as a whole is then transported in an ESD bag.

Finally, for some samples we have found that the quality of the gate dielectric deteriorated after SEM imaging [87]. Since optical microscopy shows the location of the nanowire to sufficient precision, SEM is not used for samples intended for cooldown.

3.2. MEASUREMENT SETUP

3.2.1. CRYOGENIC SETUP

Many experiments in this thesis concern probing the ground state properties of condensed matter systems. To force the system to attain its ground state configuration, temperature-induced excitations must be reduced. Hence the need for a cryogenic setup. This requirement is exemplified by unwanted quasiparticle excitations in superconducting systems. The free energy difference between the even and odd particle states of a superconductor is rapidly reduced by temperature since an unpaired electron can explore a large state space. This effect is further discussed in Chapter. 5.

In short, the limiting temperature is set by the relevant energy scales of the system, i.e. the charging energy and the superconducting gap. By properly designing the experiment we ensure these temperature requirements are compatible with the accessible refrigeration techniques. In our case, we use commercially available dilution refrigerators to reach temperatures on the order of 10 mK.

Two different dilution refrigerators are used for the experiments described in this thesis, one from Leiden Cryogenics and one from Bluefors. Both refrigerators use two pulse tubes to provide ample cooling power at a temperature of 4 K. The coldest stage is cooled down to its base temperature via dilution refrigeration [88]. Cooling power in the millikelvin regime is provided by the mixing chamber which contains both ^{3}He and ^{4}He. This mixture separates into a concentrated and dilute phase of ^{3}He. Circulating ^{3}He through the system, creates a shortage in the mixing chamber of ^{3}He in the dilute phase. This draws ^{3}He across the phase boundary from the concentrated phase, which provides cooling power through the enthalpy of mixing.

Samples for the Leiden Cryogenics system are mounted at the bottom of a probe insert. The insert can be removed from the cryostat without bringing the entire cryostat to room temperature, which speeds up sample exchange significantly. All wiring of the fridge is contained in this insert. Therefore, there is only a limited amount of space available for mounting components. Conversely, in the Bluefors system we use a fast sample exchange mechanism called a *puck* that connects to the wiring in the fridge when inserted. The puck only contains the printed circuit board containing the sample and shielding, hence having a much smaller thermal mass than the Leiden Cryogenics insert. Secondly it allows putting all wiring inside the cryostat rather than on the insert, relieving the space limitations of the Leiden Cryogenics system. Due to these space con-

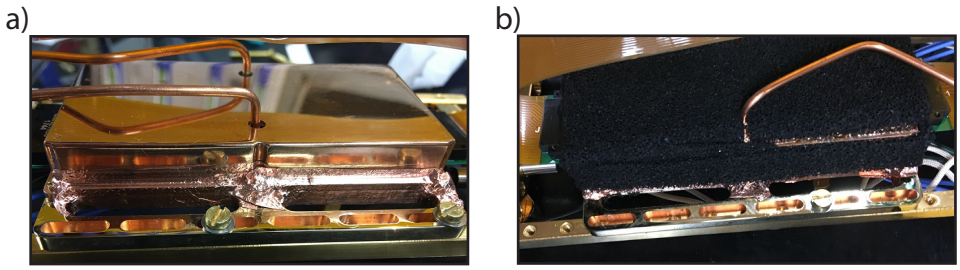


Figure 3.4: **a**) Copper casing enclosing the sample. Holes for the RF lines are not sealed yet. **b**) Eccosorb foam placed around the copper box to absorb any stray radiation in the puck.

siderations, the Leiden Cryogenics system is only used for UHF experiments while the Bluefors system is used for both UHF and SHF experiments.

3.2.2. SHIELDING

Even though the sample is cooled down below the relevant excitation energies, as discussed in the previous section, stray photons can still cause non-equilibrium occupation of excited states. Therefore, it is important to prevent these photons from reaching the sample. In this section, we describe how the sample is shielded inside the puck to dampen and reflect microwave modes around the sample[5]. Unwanted photons in the electrical lines connected to the sample must also be filtered, which will be discussed in the next section.

After the sample is mounted inside the puck it is encapsulated in a copper shield. The inside of this shield is coated with Aeroglaze Z306, which absorbs thermal radiation. All holes for the RF lines and slits where it connects with the puck are sealed with copper tape to create a light-tight enclosure, see Fig. 3.4a.

Next, microwave absorbing Eccosorb foam is applied around the copper box, see Fig. 3.4b. Finally, foil-covered Mylar is wrapped around, over the Eccosorb.

3.2.3. CRYOGENIC ELECTRONICS

Electrical signals in a wide frequency spectrum are used to control experiments and perform measurements. The implementation of the electrical lines carrying these signals depends on the intended signal frequency. We divide them into DC, or low-frequency lines (typically less than 1 kHz) and high-frequency lines (from 100 MHz up to 10 GHz).

The DC lines are used for controlling the electrostatic environment of the quantum dot system. Each tunnel gate and plunger gate is connected to a separate line in the cryostat allowing setting individual DC voltages on each gate on the device. To stabilize the gate voltages, RC low-pass filters remove unwanted high frequencies from the lines. Filters only have a limited frequency bandwidth, therefore Pi filters and copper powder filters[6] are added to filter the lines above the working frequencies of the RC filters.

[5] For the Leiden Cryogenics cryostat it turns out a copper lid coated with Aeroglaze is sufficient to shield the sample.

[6] Copper powder filters are not present in the Bluefors setup

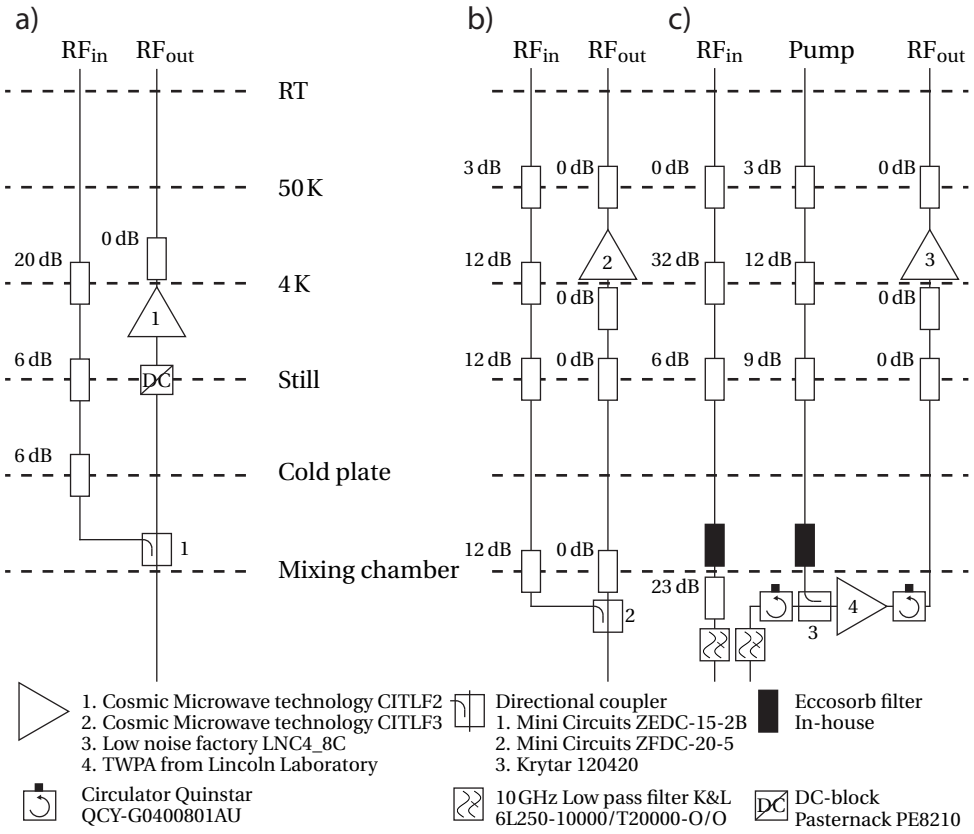


Figure 3.5: **a**) Schematic of the UHF reflectometry setup in the Leiden Cryogenics cryostat. **b**), **c**). Schematic of the UHF and SHF measurement setup in the Bluefors cryostat, respectively.

Similar to the DC lines, the high-frequency lines require filtering to prevent noise from room temperature from reaching the sample and are summarized for both setups in Fig. 3.5. Attenuators, placed in the lines carrying RF signals to the sample, reduce the incident noise. Unfortunately, these attenuators also add thermal noise themselves, dependent on their environmental temperature. Therefore, to reduce the noise most efficiently, attenuators should be distributed over all temperature stages of the cryostat. The attenuators also reduce the signal, which can be compensated by increasing the drive power of the signal generator. For readout lines, carrying signals back to room temperature, this loss of signal cannot be compensated, since signals coming from the sample are limited in power. Hence to maintain the signal to noise ratio (SNR) in the output signals, no attenuators are placed in these lines. Instead, for the SHF setup, circulators are placed in these lines to prevent any signals from the higher temperature stages from reaching the sample.

To further reduce the propagation of noise in the SHF setup, 10 GHz low-pass filters are installed to remove high-frequency photons in the lines. These filters have a limited

operating frequency, so Eccosorb filters are added to filter frequencies above this limit. This combination of low-pass filters turns out to be especially important when the sample is operated in the floating regime. In this case, quasiparticles cannot drain to the ohmic contacts and any excess high-frequency photons irradiating the sample prevent the observation of superconducting effects [7].

Directional couplers play a central role in the UHF reflectometry setups. To preserve the output signal, the main-line loss of the coupler must be minimal. Related, the main-line of the directional coupler must be impedance matched to prevent standing waves in the readout circuit. It is important to note that the directional couplers used in both setups are not rated for cryogenic temperatures[8]. The impedance matching at 4 K can therefore differ substantially compared to room temperature. The couplers used in these setups have been selected for their desirable behavior at 4 K.

The weak signals coming from the sample are amplified by a high electron mobility transistor (HEMT), a cryogenic low-noise amplifier situated on the 4 K plate of the cryostat. Amplifiers also add noise to the measurement signal, which is quantified by the noise temperature of the amplifier. Similarly, the complete readout chain of the setup, interpreted as a single amplifier, has an effective noise temperature. This quantity directly influences the attainable SNR in the measurement setup, making it a central figure of merit of the RF circuitry. Any attenuation between the sample and the first amplifier in the readout chain is detrimental to the effective noise temperature. When the HEMT is the first amplifier in the readout chain, an effective noise temperature of approximately 4 K is achieved. For reflectometry setups, the impedance matching of the amplifier is an important characteristic. Specifically, a low input return loss, S_{11} means that the amplifier behaves like a mirror, causing a standing wave between the sample and the amplifier which hinders high-quality reflectometry measurements.

We only perform transmission type measurements with the SHF setup. This frequency regime together with the additional space available in the Bluefors cryostat allows a traveling wave parametric amplifier (TWPA) to be installed on the mixing chamber plate [89]. A dedicated RF line is combined to the input of the TWPA via a directional coupler to provide the pump tone. The TWPA significantly reduces the effective noise temperature of the setup allowing for high SNR measurements.

3.2.4. ROOM TEMPERATURE ELECTRONICS

The voltages on the DC lines are controlled by an IVVI-rack, an in-house built digital-to-analog (dac) system. To preclude any 50 Hz line noise, the system is isolated from mains electricity, instead relying on batteries for power. External digital multimeters (DMM), arbitrary waveform generators (AWG) and lock-in amplifiers are connected via optical isolation amplifiers to preserve the isolation. An optical fiber connects the dac system to a computer for external control, furthermore no clock signals are generated within the IVVI-rack to minimize interference.

In the remainder of this section, we discuss several methods to measure S_{21} between

[7] Before the addition of these filters in the measurement setup, measurements similar to those shown in Chapter 7 did not show any even/odd behavior in the floating regime. This is unrelated to the lack of superconductivity mentioned in Chapter 6.

[8] Specifically, the quoted minimum operating temperature is −55 °C.

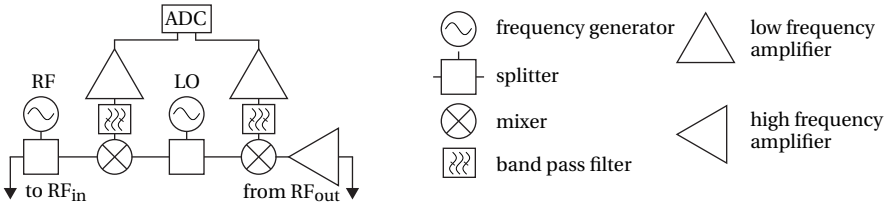


Figure 3.6: Schematic of the room temperature demodulation circuitry. The exact implementation differs slightly for the different experiments in this thesis. For clarity, the repeated circuitry for multiplexing is not shown.

RF_{in} and RF_{out}. The amplitude and phase of this quantity contain the relevant resonator behavior, as described in Sec. 2.2. A convenient way to measure the frequency dependence of S_{21} is by using a vector network analyzer (VNA) since it requires no additional RF setup and works in a broad frequency bandwidth.

When measuring at a fixed frequency, heterodyne detection can be advantageous over a VNA, a schematic which is shown in Fig. 3.6. A frequency generator is connected to RF_{in} and generates the excitation tone with frequency f_{RF}. The signal from RF_{out} is mixed together with the signal from a local oscillator (LO) with frequency f_{LO}, producing all sum and difference frequencies of the two inputs. Bandpass filters allow only the difference frequency ($f_{RF} - f_{LO}$), called the intermediate frequency, to pass through. The intermediate frequency is chosen to be in the range from 1 MHz to 50 MHz allowing digitization with an analog-digital converter (ADC). The digitized signal is demodulated in software to extract its amplitude and phase, reflecting the amplitude and phase of S_{21}.
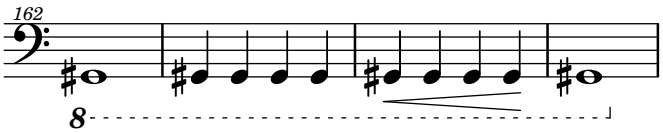
Demodulating the signal in software can quickly lead to bottlenecks in processing power and data transfer bandwidth. A field-programmable gate array (FPGA) can prevent such processing bottleneck by directly demodulating the acquired signal with dedicated hardware. Since only the real and complex part of S_{21} (called I and Q) need to be stored rather than the entire time trace, this resolves the data transfer bottleneck as well. In this way, an FPGA eliminates unnecessary overhead to the measurement time. Hence, the measurement time is now only constrained by the available SNR.

To further speed up measurements, multiple resonators can be read out at the same time. This is achieved by combining multiple probing tones in the RF_{in} port of the cryostat. By demodulating all probe tones separately, simultaneous information of multiple resonators is obtained. A single ADC can digitize multiple different signals as long as every signal has a unique intermediate frequency. Similarly, when the different RF tones all fall within the modulation bandwidth of the AWG, only a single frequency generator is needed as a shared LO for every multiplexed tone.

Instead of using a dedicated frequency generator for the excitation tone, the tone can also be synthesized from the LO using an IQ mixer. This allows using an AWG to change the amplitude, frequency and phase of the excitation tone rapidly, limited by the bandwidth of the AWG. The AWG, ADC and FPGA all must work in conjunction to enable these measurements. Therefore, these elements are increasingly implemented as combined measurement systems, vastly simplifying setting up intricate RF experiments, the multiplexed measurements described in Chapter 7 in particular.

4

RAPID DETECTION OF COHERENT TUNNELING IN AN INAS NANOWIRE QUANTUM DOT THROUGH DISPERSIVE GATE SENSING



Dispersive sensing is a powerful technique that enables scalable and high-fidelity readout of solid-state quantum bits. In particular, gate-based dispersive sensing has been proposed as the readout mechanism for future topological qubits, which can be measured by single electrons tunneling through zero-energy modes. The development of such a readout requires resolving the coherent charge tunneling amplitude from a quantum dot in a Majorana-zero-mode host system faithfully on short time scales. Here, we demonstrate rapid single-shot detection of a coherent single-electron tunneling amplitude between InAs nanowire quantum dots. We have realized a sensitive dispersive detection circuit by connecting a sub-GHz, lumped element microwave resonator to a high-lever arm gate on one of the dots. The resulting large dot-resonator coupling leads to an observed dispersive shift that is of the order of the resonator linewidth at charge degeneracy. This shift enables us to differentiate between Coulomb blockade and resonance – corresponding to the scenarios expected for qubit state readout – with a signal to noise ratio exceeding 2 for an integration time of 1 µs. Our result paves the way for single shot measurements of fermion parity on microsecond timescales in topological qubits.

The work in this chapter has been published as: D. de Jong, J. van Veen, L. Binci, A. Singh, P. Krogstrup, L. P. Kouwenhoven, W. Pfaff, and J. D. Watson, Rapid detection of coherent tunneling in an InAs nanowire quantum dot through dispersive gate sensing, Physical Review Applied **11**, 044061 (2019).

4.1. INTRODUCTION

Dispersive sensing is a promising measurement technique that enables high-fidelity readout of solid-state quantum bits, such as superconducting qubits [73, 90] or spins [91]. Recently, dispersive readout has also been proposed for future topological qubits based on Majorana zero modes (MZMs) [25, 26]. In particular, gate-based dispersive readout can be used to measure an electron tunneling rate in the system which in turn reflects the state of the qubit [92]. As a result of this difference in tunnel coupling, different qubit states can impart a different dispersive shift on a resonator coupled to the gate electrode. This frequency shift can be probed on very fast time scales, using state-of-the-art radio frequency (RF) techniques, and in a quantum nondemolition manner with minimal perturbation [73, 93].

High-fidelity, quantum nondemolition measurements require fast readout with high signal-to-noise ratio (SNR). This is particularly crucial for measurement-based quantum computation, including MZM-based architectures [25–27]. So far, however, the frequency shift of dispersive gate sensors has been fairly small, on the order of a degree [91, 92, 94–96]; correspondingly, the required readout times to resolve a difference in tunnel coupling has been in the range of milliseconds [97–99]. It is thus of great interest to find avenues toward increasing the attainable SNR, and achieve readout on the submicrosecond scale, as available for other solid-state qubit platforms [100].

In this chapter we show rapid dispersive sensing in an InAs nanowire double quantum dot system. InAs nanowires have been studied in the context of spin qubits [71, 101], but have also recently gained significant attention as host systems for MZMs that could enable the realization of topological qubits [102, 103]. We demonstrate a sensitive gate sensor based on a large-lever arm top gate that is connected to an off-chip, lumped-element resonant circuit probed with reflectometry [78]. In particular, we show a dispersive shift close to 1 MHz, which is on the order of the linewidth of the resonator; this results in a detected phase shift that approaches the maximally possible value of π. We study in detail the magnitude of the dispersive shift both as a function of tunnel coupling and readout power; we find, in agreement with theory, that the attainable shift is ultimately set by the magnitude of the tunneling rate and the resonator frequency. The large shift allows us to resolve a difference in tunneling rate with a SNR of up to 2 within 1 µs.

4.2. EXPERIMENTAL APPROACH AND SETUP

The coherent tunneling amplitude t_C, between two single-particle levels in weakly coupled quantum dots can be detected through an arising change in differential capacitance [45, 104]. The coupling affects the expectation value of charge on either island. Since level detuning and coupling is influenced by external gate voltage, the dependence of induced charge on gate voltage, i.e. the differential capacitance $C = \partial Q/\partial V_g$, depends on the coupling. This effect can be described within the framework of circuit quantum electrodynamics (circuit QED) [73] or as a 'quantum capacitance' [105] and measured by monitoring the change in differential capacitance through an external tank circuit. Our aim is to determine how fast the tunneling amplitude can be detected; this maps to the projected readout performance for MZM qubits [25, 26] where the magnitude of the

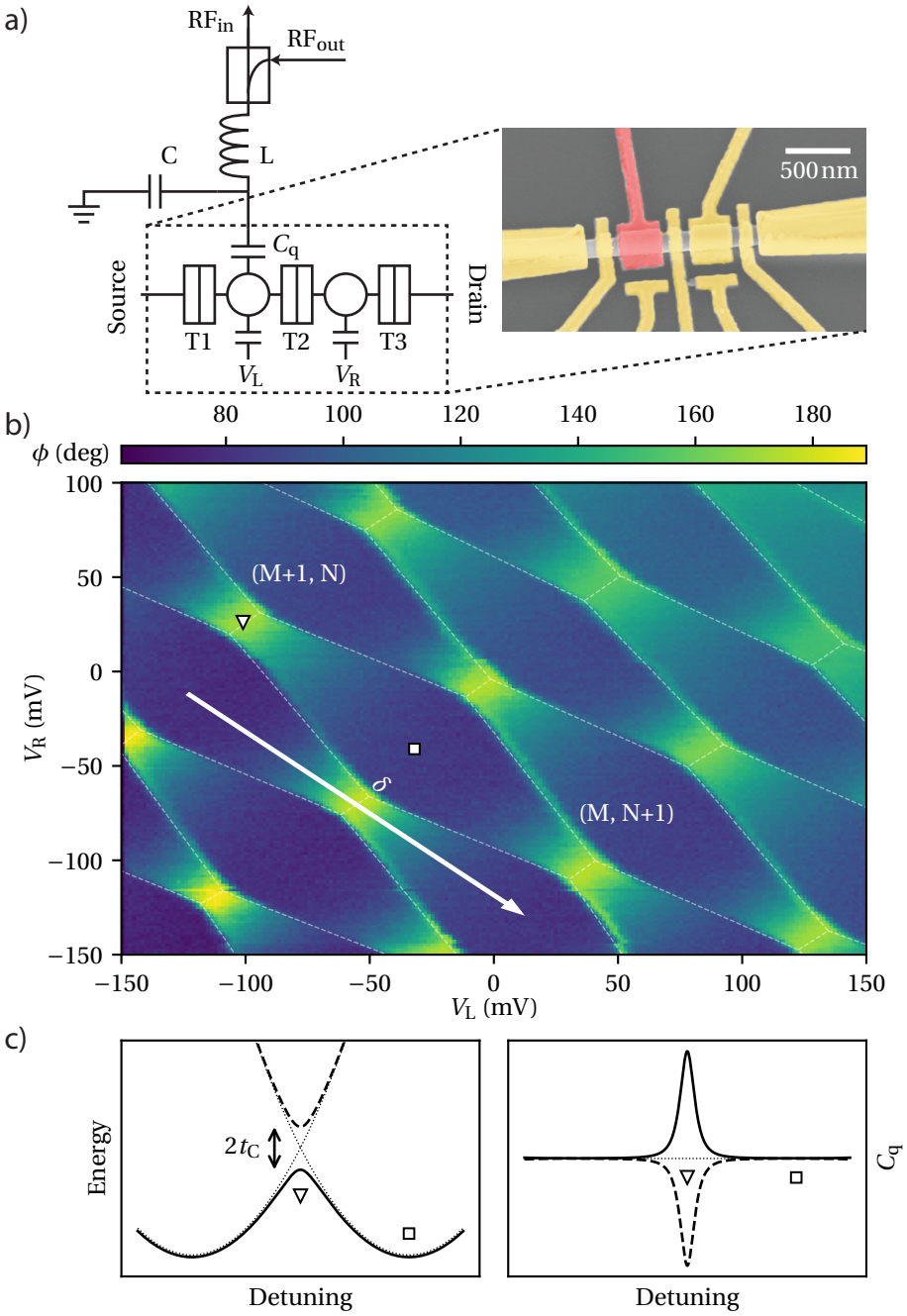


Figure 4.1: **Dispersive sensing on an InAs nanowire double quantum dot. a)** Schematic of the of experiment measurement setup. One of the quantum dots is capacitively coupled to a resonant circuit that is probed in reflectometry. Inset: false-colored electron micrograph of a nominally identical device. The sensing top gate is colored red. **b)** Charge-stability diagram measured with the gate resonator. The dashed lines are guides to the eye. The triangle marker denotes charge degeneracy while the square marker denotes Coulomb blockade. The arrow denotes the detuning from charge degeneracy, δ. **c)** Sketch of the energy levels and resulting quantum capacitance vs detuning. Solid lines, ground state; dashed lines, first excited state; dotted line, case of no interdot tunneling.

tunnel coupling is the qubit readout signal.

Our experiment approach is schematically depicted in Fig. 4.1a. We form two quantum dots in an InAs nanowire where the interdot coupling can be set through a gate voltage. We designate one of the dots as the 'sensor', whereas the other dot is merely used as an auxiliary single-level system, in lieu of MZMs. To achieve a large signal from the interdot coupling, we connect a gate with a large lever arm to a resonant circuit. The goal of the experiment is then to resolve a change in resonance frequency,

$$\delta\omega = \sqrt{LC}^{-1} - \sqrt{L(C+C_q)}^{-1}, \tag{4.1}$$

that arises from the tunneling-dependent quantum capacitance C_q (Fig. 4.1c).

To realize this experiment we fabricate a double quantum dot in an InAs nanowire with a diameter of approximately 140 nm. The nanowire is deterministically deposited using a micromanipulator on an intrinsic silicon substrate with a 20 nm SiNx dielectric layer deposited with LPCVD after removing the native SiO_2. Contacts to the nanowire are made using argon milling followed by evaporating a 10 nm Ti sticking layer and a 150 nm Au layer. A 10 nm AlOx dielectric layer is deposited using atomic layer deposition (ALD) between the nanowire and the top gates. By using a thin dielectric layer, we ensure a large lever arm from the top gates to the underlying quantum dots. The top gates consist of a 10 nm Ti layer and a 150 nm Au layer. A false color SEM image of a similar device is shown in Fig. 4.1a.

Using top gates T1, T2, and T3, a double dot is defined in the nanowire by pinching off the electron coupling to the leads and between the two dots. The top gate of the sensing dot is wire bonded to a lumped-element resonator that is fabricated on a separate chip [78]. The sample is cooled down in a dilution refrigerator with a base temperature of 20 mK. This resonator response is then probed using standard RF heterodyne techniques (Fig. 4.1a).

4.3. RESULTS

4.3.1. OBSERVATION OF QUANTUM CAPACITANCE AND DISPERSIVE SHIFT

We begin by characterizing the change in resonator response resulting from coherent tunneling between the two quantum dots. To this end, we first tune the device to a regime where the dot charge states strongly hybridize on resonance. We then record the phase response of a reflected probe field as a function of the two plunger gates, SP1 and SP2. (Fig. 4.1b). The resulting charge-stability diagram shows a prominent phase shift at charge degeneracy, hinting at a large dispersive shift of the resonator frequency. We attribute the substantial magnitude of the observed phase shift in this regime to the large lever arm of the sensing gate [73, 105]. From independent Coulomb blockade measurements we estimate the lever arm to be $\alpha = C_G/C_\Sigma \approx 0.75$, where C_G is the capacitance of the gate to the sensing dot, and C_Σ is the total capacitance seen by the dot.

The relation between the dispersive shift and the magnitude of the interdot coupling lies at the heart of the C_q detection scheme; we therefore focus next on modeling this relation from our data following earlier work performed on semiconductor dots in cQED environments [71, 95]. Near charge degeneracy the eigenstates of the double dot are superpositions of a charge delocalized between the two dots, with energy splitting

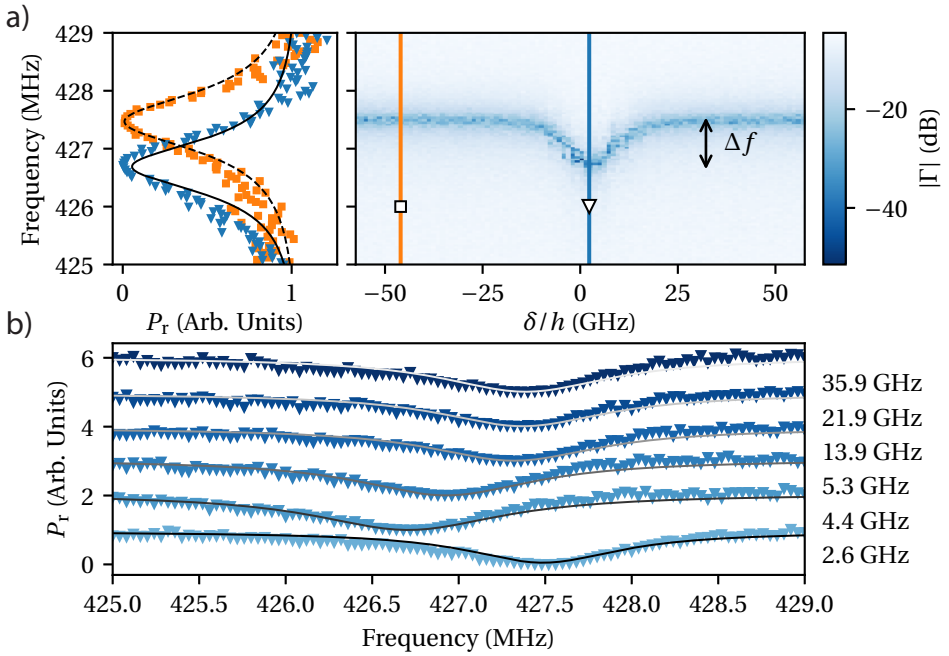


Figure 4.2: **Charge-resonator coupling. a)** Right panel: resonator reflection spectrum measured from the difference between injected (P_{RF}) and reflected RF power (P_r) corrected for estimated attenuation and gain in the setup, as a function of detuning δ. T2-gate voltage is −0.768 V for this data. Left panel: line cuts in blockade (orange; square) and at degeneracy (blue; triangle) together with fits (black) to Eq. (4.2). **b)** Resonator spectroscopy at charge degeneracy for different tunneling rates together with the fit to Eq. (4.2). Traces are offset for clarity. Tunnel rates t_C/h extracted from the fit are indicated on the right.

$\Omega = \sqrt{4t_C^2 + \delta^2}$, where t_C is the tunnel coupling, and δ is the detuning of the two dots (Fig. 4.1c) [48]. To determine the tunnel coupling, we measure the resonator response as a function of δ and the detuning of the drive from the resonance frequency (Fig. 4.2a). The reflected probe signal can be developed in a cQED approach from the input-output relations [71, 73],

$$\frac{a_{out}}{a_{in}} = 1 + \frac{i\kappa_{ext}}{-i\kappa/2 + \Delta\omega + g\chi}. \tag{4.2}$$

Hereby, $a_{in,out}$ are the complex input and output signals; $\kappa = \kappa_{int} + \kappa_{ext}$ is the total resonator damping rate, composed of internal losses κ_{int} and external coupling κ_{ext}; $\Delta\omega$ is the detuning of the drive from resonance; $g = g_0(2t_C/\Omega)$ is the effective coupling strength with g_0 being the Jaynes-Cummings coupling; and χ is the susceptibility of the double quantum dot that depends on the dephasing rate γ and detuning between charge dipole and resonator,

$$\chi = g/(\omega_0 - \Omega + i\gamma/2). \tag{4.3}$$

Figure 4.2a shows the evolution of the dispersive shift as we tune the double dot between Coulomb blockade regime and charge degeneracy, for one particular tunnel gate setting. Fitting this data yields the tunnel coupling, as well as the relevant parameters

characterizing circuit and resonator-dot coupling. In particular, we find $Q = \omega_0/\kappa \approx 350$, and $g_0/2\pi \approx 60\,\mathrm{MHz}$, consistent with the large lever arm. This procedure allows us now to correlate the tunnel coupling and the dispersive shift with the gate voltage on electrode T2 (Fig. 4.2b).

4.3.2. QUANTITATIVE MODEL OF THE DISPERSIVE SHIFT

Having established the means to analyze the resonator response, we now investigate the change in resonator frequency as a function of double dot properties. Figure 4.3a shows the magnitude of the dispersive shift at charge degeneracy as a function of tunnel coupling. This shift can be predicted using the quantum capacitance picture; from determining the expectation value of charge on the sensing dot one expects [105, 106]

$$C_\mathrm{q} = \frac{\alpha^2 e^2}{4 t_\mathrm{C}}, \tag{4.4}$$

where e is the electron charge; this relation straightforwardly yields the frequency shift through Eq. (4.1). We find that this prediction agrees well with our data for tunnel couplings $t_\mathrm{C}/h \gtrsim 4\,\mathrm{GHz}$. The effect of reduced frequency shift with increasing tunnel coupling is reflected also in the familiar geometry of charge-stability diagrams (Fig. 4.3a, inset). For small tunnel couplings we observe a reduction in the shift; this behavior is likely due to noise in the system, such as thermal fluctuations [96] or charge fluctuations on the gates (i.e. fluctuations in δ). This noise would effectively blur out the C_q peak as it narrows with decreasing t_C.

A natural question that arises is in which regimes this simple description holds. In particular, from the quantum capacitance picture one could naively expect that it is always possible to increase the power of the readout tone to increase the SNR. However, this view ignores any internal dynamics of the quantum dot system that can impact the dispersive shift. Most importantly, increasing the AC voltage of the readout drive can induce transitions of the ground state to the excited state of the double dot, resulting in an incoherent mixture. Since the dispersive shift from the excited state is opposite to that of the ground state, excitation would thus lead to a reduction of the measured shift.

In Figure 4.3b we show the evolution of the dispersive shift when increasing the readout-drive amplitude; indeed, the shift disappears entirely at large drive amplitudes. We compare this data to a model in which we compute the excitation of the double dot by assuming that the readout drive acts as a detuned Rabi drive (with detuning $\omega_0 - 2t_\mathrm{C}/h$) and the double dot dephases quickly. We find that the double dot approaches a fully mixed state in the same range in which the disappearance of the shift occurs; the resulting predicted dispersive shift is in very good agreement with the data.

We can therefore conclude that the tunnel coupling has two competing influences on the observed resonator shift: for one, the shift gets larger for decreasing t_C following Eq. (4.4). On the other hand, in the present setup a decreased tunnel coupling results in reduced drive detuning; this in turn increases excited-state population, reducing the shift again.

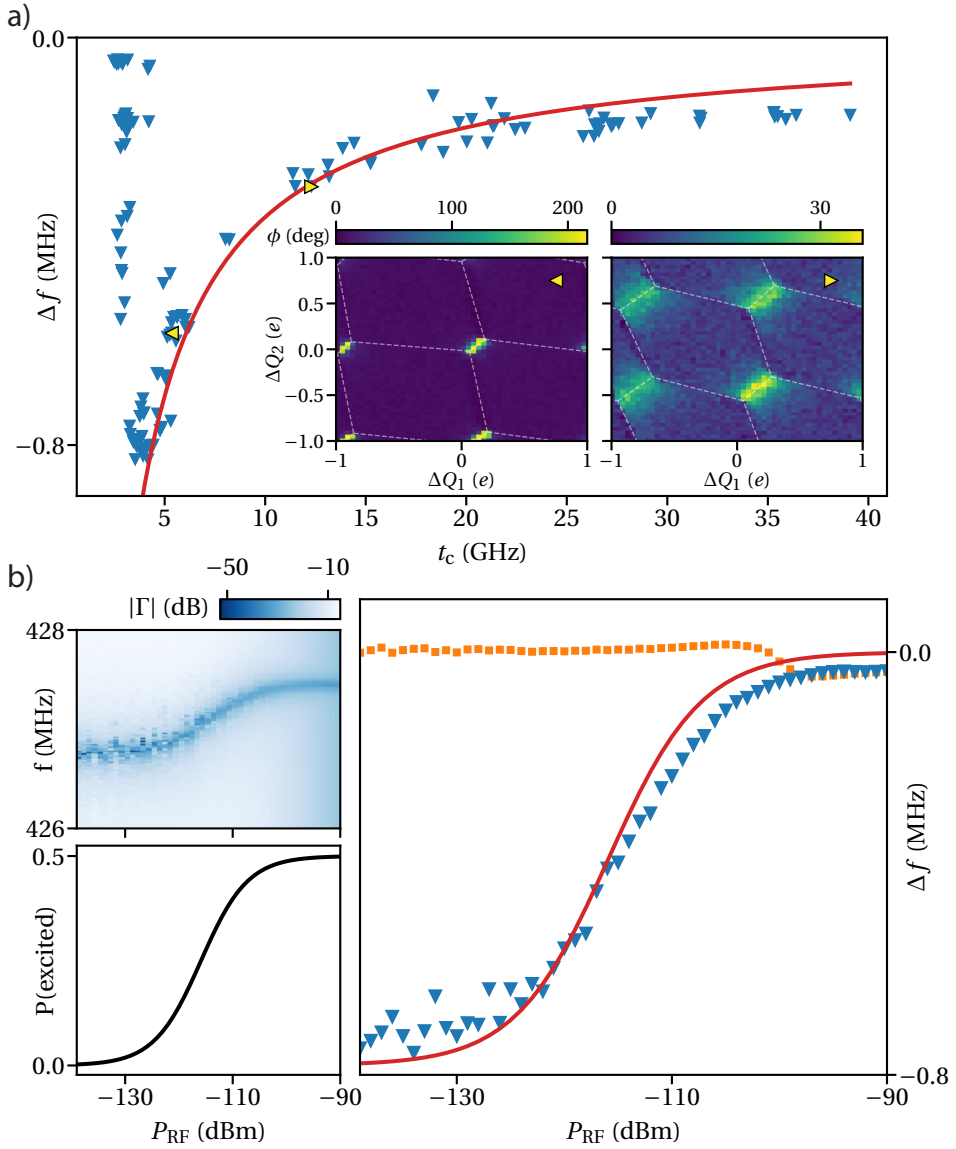


Figure 4.3: **Evolution and modeling of the dispersive shift. a)** Frequency shift as a function of tunneling rate, extracted from fitting spectroscopy data to Eq. (4.2). We estimate an accuracy of 5 % for extracting the tunnel coupling and of 40 kHz in the extraction of Δf. Solid line, independent theoretical prediction from Eq. (4.4). Inset: charge-stability diagrams for tunneling rates corresponding to the yellow markers. **b)** Resonator response as a function of frequency and power. Power is given at the sample level; this is attenuated by a total of approximately 79 dB after the generator. Top left panel: resonator spectroscopy as function of RF power. Bottom left panel: calculated steady-state population in the excited state. Right panel: resonator shift in blockade (orange), and on degeneracy (blue). Red: prediction from the excited-state population by assuming that the net shift is given by the population-weighted average between ground- and excited-state shifts.

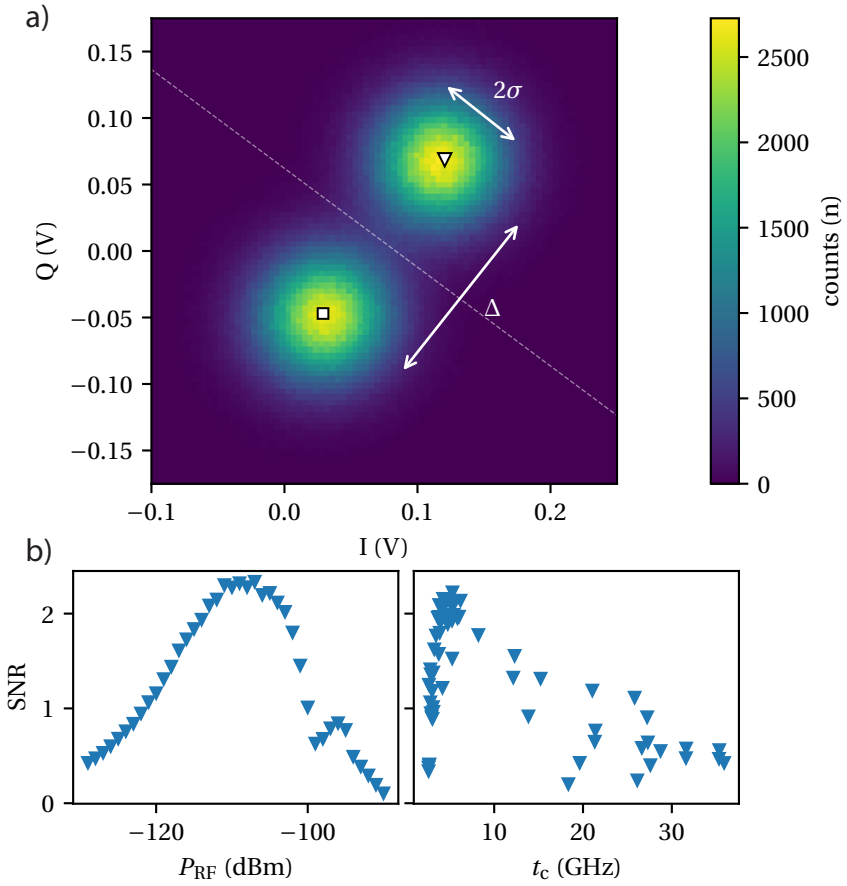


Figure 4.4: **Readout SNR. a)** Histogram of resonator reflection measurements in Coulomb blockade (square marker) and charge degeneracy (triangle marker). This data is taken with a tunnel coupling of 4.3 GHz and a readout power of $P_{RF} = -105$ dBm. Each count corresponds to an integration time of 1 µs. The SNR is defined as $\Delta/2\sigma$. The dashed line is the threshold used for state identification. **b)** Attained SNR as a function of readout power (left panel) and tunnel coupling (right panel). For the tunnel coupling dependence, readout power and frequency are optimized for every data point individually.

4.3.3. SNR FOR DETECTING A TUNNEL AMPLITUDE

In order to show the feasibility of dispersive gate sensing for qubit readout, we finally investigate the time-resolved resonator response. In particular, we aim to show that the difference in charge hybridization between Coulomb blockade and charge degeneracy can be obtained on fast time scales [25, 26] To do so, we repeatedly measure the RF-signal in Coulomb blockade and on charge degeneracy by switching between the two points in the charge-stability diagram. The signal is then binned in 1 µs intervals and for each interval, the in-phase and quadrature components of the signal are extracted and represented in a histogram (Fig. 4.4a). From Gaussian fits we can then extract the SNR, which is given by the distance between the two distributions, Δ, divided by their

full width, 2σ. These widths are set by the noise in the system, which is dominated by the thermal contribution of the cryogenic amplifier. From independent measurements we estimate the equivalent noise temperature of the readout circuit to be around 4 K.

In Figure 4.4b we show the attained SNR per 1 µs 'shot' as a function of readout power and tunnel coupling. The SNR reaches its peak value of > 2 for a RF power of $P_{\mathrm{RF}} \approx -109$ dBm and a tunnel coupling of approximately 5 GHz. In other words, the probability of misidentifying the state of the system using thresholding is less than 2 % for these settings. Since the signal is largely set by the frequency shift, the dependence of the SNR on t_{C} closely follows the evolution of the dispersive shift shown in Fig. 4.3a. The power dependence results from the competition between double dot excitation and signal increase. The optimal power is reached at the point where the diminishing frequency shift starts dominating over the improvement gained from larger accuracy in the estimation of I and Q.
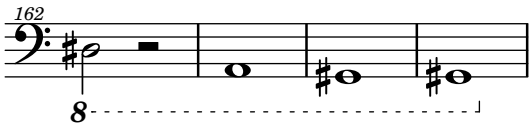
4.4. CONCLUSIONS

We perform gate-based dispersive sensing on a double quantum dot in an InAs nanowire. The observed charge-tunneling-induced dispersive shift on our resonator is comparable to the resonator linewidth, enabling fast detection of the presence of the tunnel amplitude with high SNR. Notably, this result was achieved with a low-Q, lumped-element resonator operating at a frequency of less than 1 GHz; these types of resonators hold great promise for scalable readout due to their reduced footprint compared to high-Q, CPW resonators that are more traditionally used in cQED [73]. Utilizing the large resonator shift, we show that states corresponding to different charge hybridizations can be distinguished in 1 µs measurements while retaining a SNR exceeding two in our experimental setup. We further establish that the factor that predominantly limits the SNR is the tunnel coupling. Its magnitude determines the dispersive shift, and its detuning from the resonator frequency places a limit on the readout power that can be used before adverse effects take over.

Our results show that high-fidelity measurements of semiconductor nanowire-based qubits could be performed using gate sensing on the single-microsecond scale. This is particularly promising for MZM-based topological qubits that could be realized in nanowire networks [25, 26]. Since our work illustrates the dominating factor of only a few key device parameters — such as electron tunneling rate, gate lever arm, and resonator frequency — our results can provide guidance for the design of qubit and measurement circuits. We further expect that existing technology could be used to lower the noise temperature of the cryogenic amplifier [89, 107–109] or optimize the sensing circuits [110] in order to enhance the attainable SNR further, and reduce the required measurement time.

5

REVEALING CHARGE-TUNNELING PROCESSES BETWEEN A QUANTUM DOT AND A SUPERCONDUCTING ISLAND THROUGH GATE SENSING



We report direct detection of charge-tunneling between a quantum dot and a superconducting island through radio-frequency gate sensing. We are able to resolve spin-dependent quasiparticle tunneling as well as two-particle tunneling involving Cooper pairs. The quantum dot can act as an RF-only sensor to characterize the superconductor addition spectrum, enabling us to access subgap states without transport. Our results provide guidance for future dispersive parity measurements of Majorana modes, which can be realized by detecting the parity-dependent tunneling between dots and islands.

The work in this chapter has been published as: J. van Veen, D. de Jong, L. Han, C. Prosko, P. Krogstrup, J. D. Watson, L. P. Kouwenhoven, and W. Pfaff, Revealing charge-tunneling processes between a quantum dot and a superconducting island through gate sensing, Physical Review B **100**, 174508 (2019).

5.1. INTRODUCTION

Quantum dots coupled to superconductors can give rise to novel physical phenomena such as π and ϕ_0-junctions [111–113], Cooper pair splitting [114–116], and Yu-Shiba-Rusinov (YSR) states [117, 118]. These phenomena arise because the single-electron states of the dot hybridize with the more complicated many-particle states of the superconductor. Recently, such hybrid systems have gained interest in the context of Majorana zero modes (MZMs) where the quantum dot (QD) can, for example, be used as a spectrometer [119]. Moreover, projective parity measurements can be achieved by coupling a QD to a pair of MZMs, which are located on a superconducting island (SC) [103, 120], enabling topologically protected quantum computation. These projective measurements rely on the parity-dependent hybridization between a single dot level and the MZMs [25, 26]. Therefore, unambiguous detection of coherent tunneling between a QD and a superconducting island is needed to implement this readout.

Dispersive gate sensing (DGS) provides direct access to charge hybridization between weakly coupled dots or islands. More precisely, tunneling within these structures can impart a frequency shift on a resonant circuit that can be observed on short time scales with high accuracy. In this way, experiments have revealed coherent charge hybridization between superconductors [105, 121, 122] and semiconductor double quantum dots [71, 92, 95, 123]. Moreover, capacitive RF sensing has been used to study charging of QDs connected to normal and superconducting reservoirs [124–126]. As such, DGS presents an excellent opportunity for studying charge-tunneling in hybrid structures containing QDs.

In this paper, we report direct detection of different types of charge-tunneling processes between a QD and a SC through DGS on the QD. From observations of the resonator response, supported by numerical simulations, we find that the nature of the tunneling depends crucially on the ordering of the relevant energy scales of the SC. When the smallest scale is the energy of the lowest single-particle state, the QD and SC can exchange quasiparticles, giving rise to the characteristic 'even-odd' effect. Conversely, when the charging energy of the SC is lowest, we detect signatures of Cooper pairs tunneling out of the SC. Depending on the tunneling amplitude, this results in either $1e$-charging of the QD, with the other electron leaving into a reservoir, or $2e$-charging of the QD. Tunneling to the single-particle states can, however, be re-enabled by operating the device in a floating regime where the total number of charges in the two systems is conserved. These results show that DGS allows us to effectively perform RF-only tunneling spectroscopy on the SC. To this end, we use the QD and capacitively-coupled resonator as a probe to characterize a subgap state in the SC without need for transport via leads. Our method is complementary to recent experiments that employed the dispersive response of inductively-coupled resonators to probe the Andreev bound state occupation in galvanically-isolated nanowire Josephson junctions [127, 128].

A schematic of our experiment is shown in Fig. 5.1a,b. The QD-SC hybrid double dot is formed in an InAs nanowire with an epitaxially grown Al-shell on two of its facets. The superconducting island consists of a proximitized wire segment, which is defined by removing the Al outside a 1.2 µm window using wet etching. The low-carrier density in the wire allows for gate-tunable subgap states in the SC [129]. Tunneling barriers are implemented with gates, insulated from the wire by 10 nm AlO_x. They are used to define

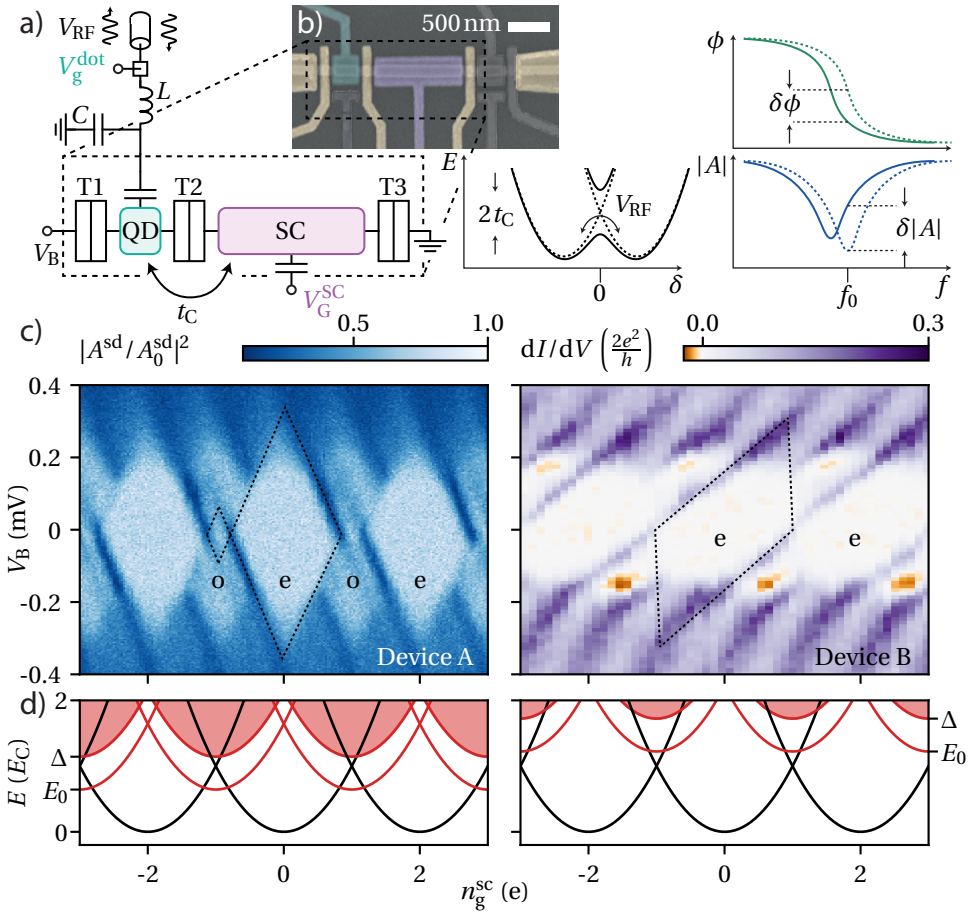


Figure 5.1: **Experimental setup and sample characterization. a)** A gate sensor detects the tunneling of charges on/off the QD. Charge hybridization between QD and SC results in an anti-crossing in the energy spectrum at zero detuning $\epsilon = 0$, and shifts the LC resonator, causing in a change in amplitude, A, and phase, ϕ, response of a probe signal at the bare resonator frequency, f_0. **b)** False-colored electron micrograph of a nominally equivalent hybrid double dot. An additional dot, shown on the right of the device, is unused in this experiment. **c)** Coulomb blockade measurement of the SC. Left: device A, measured using RF reflectometry off the source (circuit not shown). The even-odd pattern indicates $E_0 < E_C^S$. Right: device B, measured using standard lock-in techniques. The doubling of the period at low bias V_b illustrates that $E_0 > E_C^S$. **d)** Energy dispersion of the superconducting island for device A (left) and device B (right). The even (odd) energy levels are shown in blue (green). The odd parity sector consists of a discrete subgap state at E_0 and a continuum of states above Δ (shaded).

the QD and to control the various tunneling rates. Large-lever arm top gates ('plungers') on both QD and SC can be used to tune the chemical potentials. We have measured two nominally-identical devices, labelled A and B. For both devices, we connected the QD plunger to an off-chip, superconducting resonator with a resonance frequency of 449.5 (443.2) MHz for device A (B) [78], see Sec. 5.4.1. We use its response near the resonance frequency to probe charge tunneling on and off the dot. All measurements are done at temperatures of $T \approx 20\,\mathrm{mK}$ and at zero magnetic field unless otherwise indicated.

The relevant energy scales in our devices can be obtained from Coulomb blockade measurements: Figure 5.1c shows Coulomb diamonds of the superconducting island alone, measured through conductance. The diamonds of device A display a clear even-odd pattern, indicating that the energy of the lowest odd-parity state, E_0, is smaller than the charging energy of the superconducting island, $E_C^S = e^2/2C_\Sigma^S$, where C_Σ^S is the total capacitance of the SC (Fig. 5.1d) [130, 131]. For this device, we estimate $E_0 = 72\,\mu\mathrm{eV}$ and $E_C^S = 112\,\mu\mathrm{eV}$ from the extent of the diamonds. Conversely, the charging of the superconducting island of device B is $2e$-periodic, indicating that $E_0 > E_C^S$ [131, 132]; here, we estimate $E_0 \approx 90\,\mu\mathrm{eV}$ and $E_C^S \approx 70\,\mu\mathrm{eV}$. While in an ideal BCS superconductor E_0 is equal to the superconducting gap Δ, current measurements on device A and the negative differential conductance observed in device B indicate the presence of subgap states [120], see Sec. 5.4.3. We attribute the difference in charging energies and E_0 between the devices to a combination of a slightly smaller wire diameter for device A and typical sample-to-sample variations arising from fabrication. In both devices, the charging energy of the dot, $E_C^{QD} \approx 200 - 300\,\mu\mathrm{eV}$, is the largest energy scale in the system, and the typical QD level spacing exceeds the thermal energy, see Sec. 5.4.3.

5.2. RESULTS

In the following, we investigate the change in resonator response when charges are able to tunnel between the QD and SC at zero bias, beginning with device A. To this end, we form a hybrid double dot by tuning the gates T1 and T2 close to pinch-off, and T3 into pinch-off. Figures 5.2a,b show the resonator response as a function of the two plunger gates in the weakly coupled regime. Both amplitude and phase response display the charge stability diagram (CSD) of the hybrid double dot, which shows a clear $1e$ pattern along the QD gate, and an even-odd pattern along the SC gate; this is again a manifestation of $E_0 < E_C^S$, and the CSD shape can be readily reproduced by computing the charge ground states of the system, see Sec. 5.4.5.

We focus on the interdot transitions, highlighted in Figs. 5.2a-c, where we observe a strong amplitude and phase response on all charge degeneracy points. Interestingly, we see a strong difference in the resonator response across interdot transitions with a different parity of the total particle number, indicating a difference between the coupling between the involved states [133].

This dependence on total parity can be understood as a spin-dependent tunnel coupling [134]. To see this, we label the states according to their pairing; for the SC states as even/odd, and for the QD states as singlet/doublet: $|e/o, S/D\rangle$. We can differentiate couplings between two sets of states; $|e, D\rangle$ to $|o, S\rangle$ and $|e, S\rangle$ to $|o, D\rangle$. The coupling

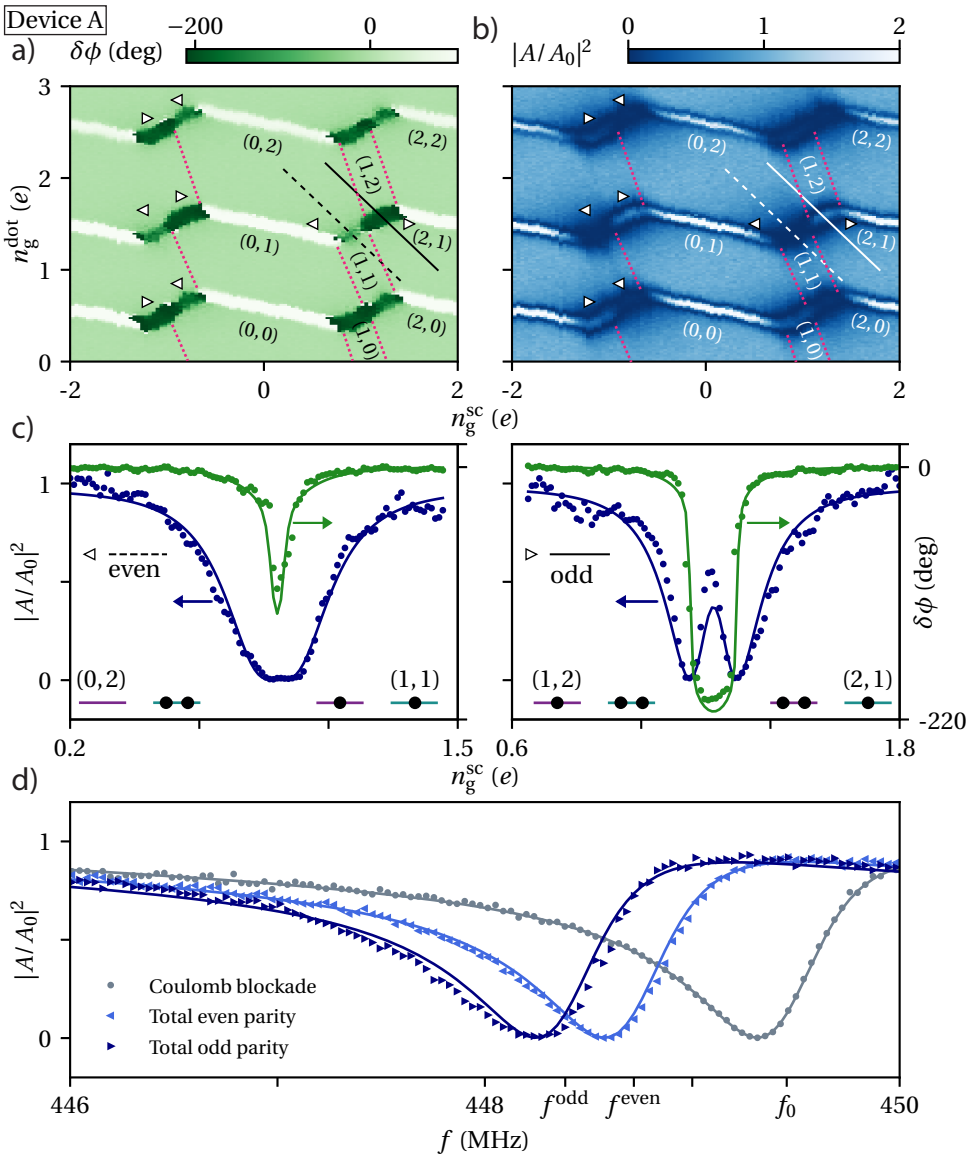


Figure 5.2: **Spin-dependent tunneling between a QD and a SC. a)** and **b)** Charge stability diagram of device A measured in phase **a)** and amplitude **b)**. The charge states are labeled $\left(n^{SC}, n^{QD}\right)$ with respect to the state (N, M) with N and M even. Dashed pink lines: expected locations of the lead-island transitions, in accordance with data obtained from a resonator connected to the SC gate (Sec. 5.4.4), and simulations of the charge ground state of the system (Sec. 5.4.5). **c)** Linecuts of the phase (green dots) and amplitude (blue dots) along two interdot transitions. Dashed line and left-pointing triangle marker, left panel: transition between (0,2) and (1,1), representative of transitions between states of total even parity. Continuous line and right-pointing triangle marker, right panel: transition between (1,2) and (2,1), representative of transitions between states of total odd parity. The lines are fits to a circuit QED model with $t_C^{odd} = t_C^{even}/\sqrt{2}$, see Sec.5.4.2. We find a good fit with $t_C^{even} = 20\,\text{GHz}$ and $g_0 = 100\,\text{MHz}$. **d)** Full-frequency response of the resonator (symbols) together with fits (lines) obtained from a pair of interdot transitions that show the parity effect (outside the gate space shown in **a,b**).

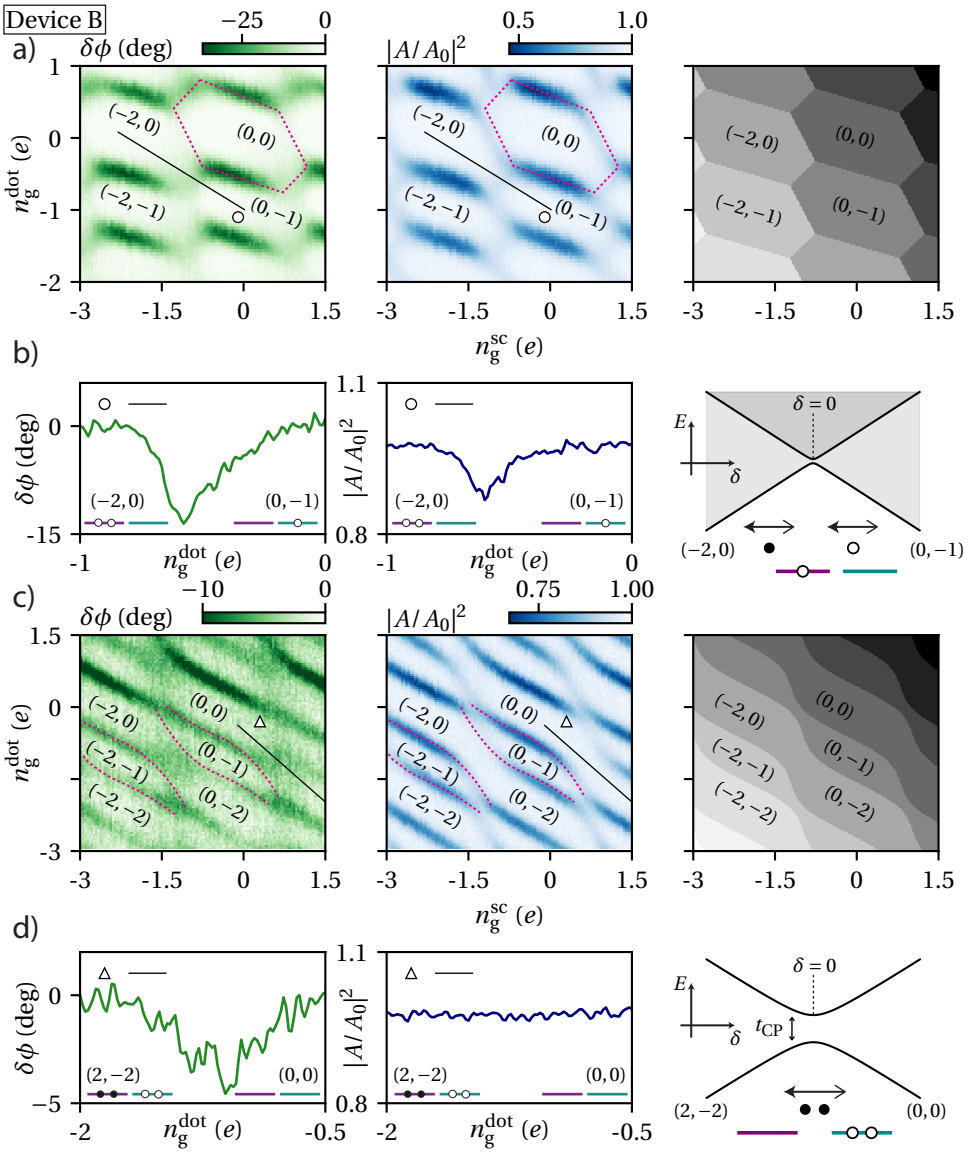


Figure 5.3: **Cooper pair tunneling in a hybrid double dot. a)** Charge stability diagram measured in phase (left) and amplitude (middle) along with a simulation of the charge ground state (right) in the weakly coupled regime. The charge states are labeled $\left(n^{SC}, n^{QD}\right)$ with respect to the state (N, M) with N even. Dashed pink lines: locations of the transitions from the (0,0) state as a guide to the eye. The gray scale in the simulation indicates the sum of the charge in the combined system. **b)** Linecuts of the phase (green) and amplitude (blue) along the (-2,0) to (0,-1) interdot transition. This transition involves a reservoir with a continuous spectrum, indicated by the shaded region above the lowest available energy state. The schematic shows how these states couple via crossed Andreev reflection. **c)** Same as in **a)** for the strongly coupled regime. Dashed pink lines: locations of the lead transitions from the (-2,-1) and (0,-1) states as a guide to the eye. **d)** Linecuts of the phase (green) and amplitude (blue) along the (2,-2) to (0,0) interdot transition. These states couple via Cooper pair tunneling.

is different for these two sets because of spin degeneracy: From $|e,S\rangle$ either of the two electrons forming the singlet can tunnel with equal probability, giving rise to a two-fold degeneracy in the coupling between $|e,S\rangle$ and $|o,D\rangle$, i.e. between the states with total even parity. On the other hand, from $|e,D\rangle$ only one of the two electrons can tunnel from QD to SC due to Pauli exclusion; in this case no degeneracy is present. As a result, the transition rate between states of total even parity is expected to be $\sqrt{2}$ times stronger than between states of total odd parity, corresponding to a $\sqrt{2}$ times smaller frequency shift.

We model the resonator response across the interdot transition by using a circuit QED model derived from input-output theory [71], see Sec. 5.4.2. We find a good agreement between our data and the model using $t_C^{odd} = t_C^{even}/\sqrt{2}$. However, the weak parameter dependence of the model makes it unreliable to confirm the spin-dependence of the tunnel coupling. To obtain quantitative agreement, we measure the frequency-dependent resonator response at a pair of interdot transitions that show this parity effect (Fig. 5.2d). From fits to the resonator responses we extract frequency shifts with a ratio of $(f_0 - f^{odd})/(f_0 - f^{even}) = 1.45 \approx \sqrt{2}$, consistent with the expected spin-dependent tunneling amplitude.

For device B, the situation changes significantly. The energy ordering $E_0 > E_C^S$ implies that quasiparticle states are not accessible (Fig. 5.1d). We form a hybrid double dot by tuning T1, T2, and T3 close to pinchoff. The CSD for a weak QD-SC coupling is shown in Fig. 5.3a. The diagram is $2e$-periodic in the SC gate, indicating that the island is charged via Andreev reflections from the lead. The QD is again $1e$-periodic. To model the measured CSDs, we compute the charge ground state by diagonalizing an effective Hamiltonian of the system that includes charging effects, the superconducting gap in the island, and coupling terms, see Sec. 5.4.5. This model, with the energy scales extracted from the Coulomb blockade measurements and an adjustable tunneling amplitude (rightmost panel in Fig. 5.3a), describes the observed CSD well.

The different gate charge periodicity for the QD and SC leads to interdot transitions that change the total charge of the dot-island system. This implies that a reservoir must be involved in the corresponding charge-transfer process. The observed resonator signal, with a linecut shown in Fig. 5.3b, results from tunneling on and off the QD, and thus should not contain information of SC-lead coupling [133]. A possible candidate for the precise underlying process that gives rise to our data is crossed Andreev reflection (CAR) [114, 115]. There, a hole from the QD is converted to an electron in the lead, consistent with the charge states involved in the experiment. This process is exponentially suppressed in the length of the island $\exp(-L/\pi\xi)$, where ξ is the superconducting coherence length [135]. Still, with $L = 1.2\,\mu m$ and assuming a coherence length of $\xi \sim 260\,nm$ [103] this remains a plausible scenario.

Interestingly, increasing the tunnel coupling allows for bringing the system into a regime where a particle-conserving interdot transition emerges. The CSD in a more strongly coupled regime, together with a simulation of the charge ground states is shown in Fig. 5.3c. In this regime, we assume an induced gap in the quantum dot, consistent with earlier studies on YSR states [118]. Here, we observe that the regions with odd charge number in the QD shrink, while the regions with an even number of QD charges connect, resulting in an even-odd pattern in both gates. Now, the interdot transition

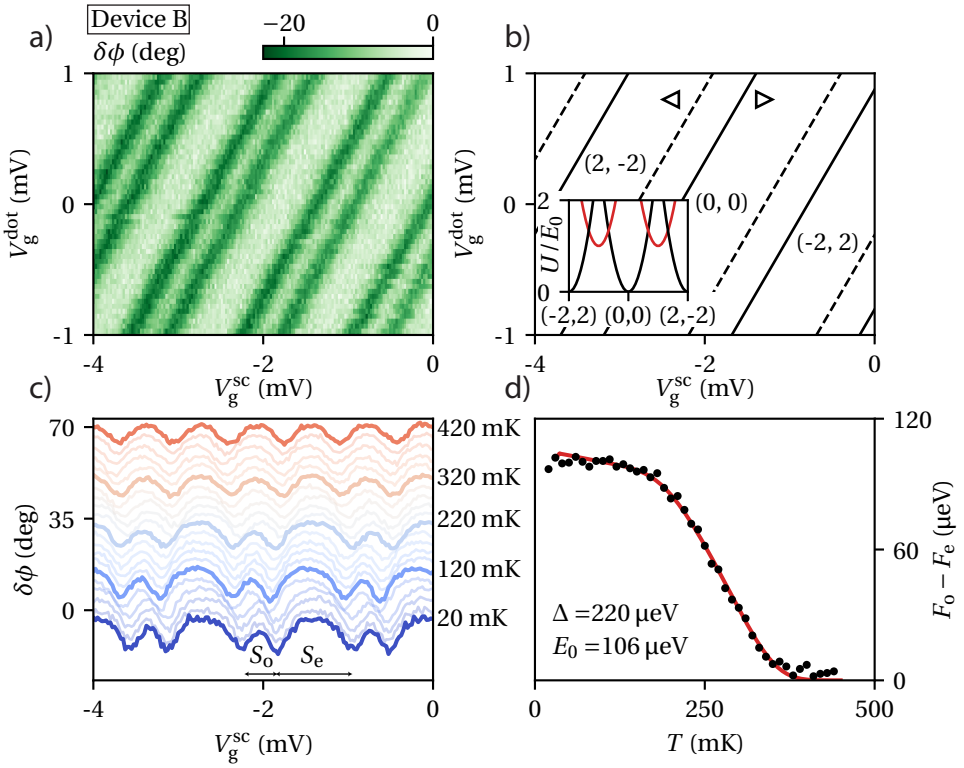


Figure 5.4: **Spectroscopy of a subgap state in the floating regime a)** Charge stability diagram measured in phase in device B. The diagonal lines indicate that the total charge in the system is conserved. **b)** Calculated positions of the transitions in good agreement with the measured stability diagram. Inset: energy spectrum with even states in black and odd states in green, showing that the even-odd pattern is caused by the parity effect even though $E_0 > E_C^S$. **c)** Temperature dependence of the even-odd pattern. **d)** The evolution of the free energy difference with temperature (black dots), with a fit to the model described in Ref. 120 (green line). The free energy difference is extracted from the even-odd pattern via $F_o - F_e = (S_e - S_o)\, e\alpha_{sc}/4$ with $\alpha_{sc} = 0.9$ the lever arm of the SC gate.

appears purely dispersive (Fig. 5.3d): we observe only a small phase shift, without any amplitude response. Overall, our data is consistent with coherent Cooper pair transfer between the dot and the island.

As we have seen, the main difference between the two devices is that the odd states of the SC can not be directly accessed in the regime $E_0 > E_C^S$. This changes in absence of lead reservoirs because quasiparticles that tunnel from the QD onto the SC are confined to the system [122]. The additional energy associated with decharging the QD makes Cooper pair tunneling energetically unfavorable when $E_0 < E_C^S + E_C^{QD}$. We realize this situation experimentally in device B by closing the outer tunnel barriers, through gates T1 and T3. The resulting CSD and corresponding calculation of the ground state transitions are shown in Figs. 5.4a,b. It can readily be seen that no transitions to a reservoir take place, and the even-odd pattern is indicative of the alternating occupation of even and

odd states of the SC.

Importantly, even though SC and QD are now galvanically isolated from the environment, the gate sensor still allows us to study the quasiparticle states in the SC. To show this, we measure the evolution of the even-odd spacing as a function of temperature (Fig. 5.4c). This spacing is a measure for the free energy difference of the SC. In particular, the temperature evolution of the free energy difference can be used to identify and characterize subgap states [136]; for proximitized nanowires, this has earlier been studied in transport [120]. The extracted free energy difference $F_o - F_e$ as a function of temperature is shown in Fig. 5.4d. A fit to the model from Ref. 120 yields a gap of $\Delta = 220\,\mu\text{eV}$, a supgap state energy of $E_0 = 106\,\mu\text{eV}$, and an Al volume of $V = 2.9 \times 10^5\ \text{nm}^3$, consistent with the dimensions of the island. We note that the slightly larger energy of the subgap state is consistent with the more negative plunger gate voltage for this measurement. The excellent quality of the fit corroborates our initial assessment of the presence of a supgap state (Fig. 5.1b). This result shows clearly that the resonator response of the QD gate sensor can be used to characterize states of the SC, even when leads for transport experiments are not available.

5.3. DISCUSSION AND CONCLUSION

In summary, we have performed dispersive gate sensing on a quantum dot that can exchange particles with a superconducting island. Analysis of the resonator response has allowed us to directly detect the charge-tunneling processes that take place between the dot and the superconductor. We have observed single or multi-particle tunneling processes, depending on the dominating energy scales of the hybrid double dot. Our results show that DGS provides an excellent tool for studying subgap excitations. In particular, using a QD and gate sensor allows performing spectroscopy without transport, which is relevant in cases where particle number should be conserved, such as likely required for qubit devices that operate based on parity. The ability of DGS to resolve differences in tunnel couplings — as seen for the case of spin-dependent tunneling — provides a very simple means for precisely characterizing hybridization while leaving the system in the ground state. Going forward, these demonstrated abilities will be crucial for the realization and operation of Majorana qubits based on proximitized nanowires [25, 26]. Our results thus set the stage for the implementation of quantum measurements of topological qubits.

5.4. SUPPLEMENTAL MATERIAL

5.4.1. RESONATOR CHARACTERIZATION

In this section, we present the frequency response for both resonators (Fig. 5.5a,b). From fits to the asymmetric resonator model described in section II (with $\Omega \to \infty$ i.e. in Coulomb blockade), we extract the resonance frequency f_0 and the loaded quality factor $Q = f_0/\kappa$. The resonance frequency is set by the inductance of an off-chip, superconducting spiral inductor ($L = 420\,\text{nH}$), and the parasitic capacitance of the resonator to its environment [78].

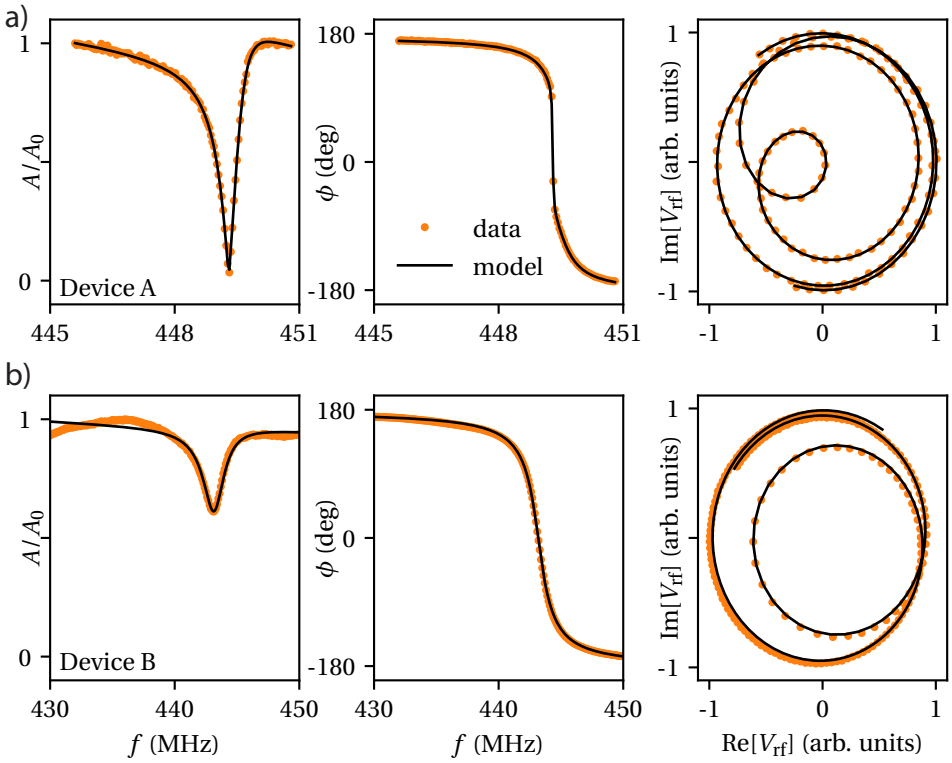


Figure 5.5: **Resonator characterization.** The resonators are characterized by measuring their response $V_{RF} = Ae^{i\phi}$ versus frequency across their resonance frequency. The left panels show the (normalized) amplitude A/A_0 response; the middle panels the phase response ϕ (corrected for the electrical delay in our setup); and the right panels the (normalized) real versus the imaginary part of the response. **a)** For device A, we find $f_0 = 449.4\,\text{MHz}$ and $Q = 620$. **b)** For device B, we find $f_0 = 443.2\,\text{MHz}$ and $Q = 194$.

5.4.2. MODEL FOR THE RESONATOR RESPONSE

In this section, we present the model used to fit the linecuts in Fig. 5.2 of the main text. We solve the Heisenberg-Langevin equations for the reflected probe field of a resonator coupled to a double quantum dot [71]. In order to match our data, we add a phenomenological, complex scattering parameter (S) to account for impedance mismatches in our setup, following the reasoning presented in Ref. 74. Combined, we arrive at

$$\frac{a_{out}}{a_{in}} = \frac{\kappa_{ext}}{i\Delta_0 + \kappa/2 + g_{eff}\chi} - 1 + |S|e^{i\phi}, \tag{5.1}$$

with susceptibility

$$\chi = \frac{g_{eff}}{-\Delta + i\gamma/2}. \tag{5.2}$$

In these equations, a is the probe field, $\Delta_0 = \omega_0 - \omega$ the detuning between the resonator and the probe field; $\Delta = \Omega/\hbar - \omega$ the detuning between the double dot and the probe field, where $\Omega = \sqrt{4t_C^2 + \epsilon^2}$ with t_C the tunnel coupling and ϵ the detuning between the

quantum dots; κ_{ext} the external coupling rate; $\kappa = \kappa_{\text{ext}} + \kappa_{\text{int}}$ the total loss rate with κ_{int} the internal loss rate; $g_{\text{eff}} = g_0 \frac{2t_C}{\Omega}$ the coupling between the resonator and double dot; and γ the dephasing rate of the double dot.

Table 5.1: **Overview of the parameters used to fit the resonator response in Fig. 5.2c. of the main text.**

parameter	value
κ_{ext}	0.41 MHz
κ	0.73 MHz
t_C^{even}	20 GHz
g_0	100 MHz
γ^{even}	2.6 GHz
γ^{odd}	1.0 GHz
S	$-0.054 - 0.354\imath$

5.4.3. ADDITIONAL COULOMB DIAMOND MEASUREMENTS

In this section, we present additional Coulomb blockade measurements of the quantum dot (QD) in Fig. 5.6, and the superconducting island (SC) of device A in Fig. 5.7.

From the Coulomb diamonds in Fig. 5.6, we extract the QD charging energy and estimate the typical level spacing of the dot. We find that the charging energy is the largest energy scale for both QD-SC systems. Moreover, the level spacing, δ, exceeds the thermal energy for both QDs, and it fluctuates with the charge occupation in the QD.

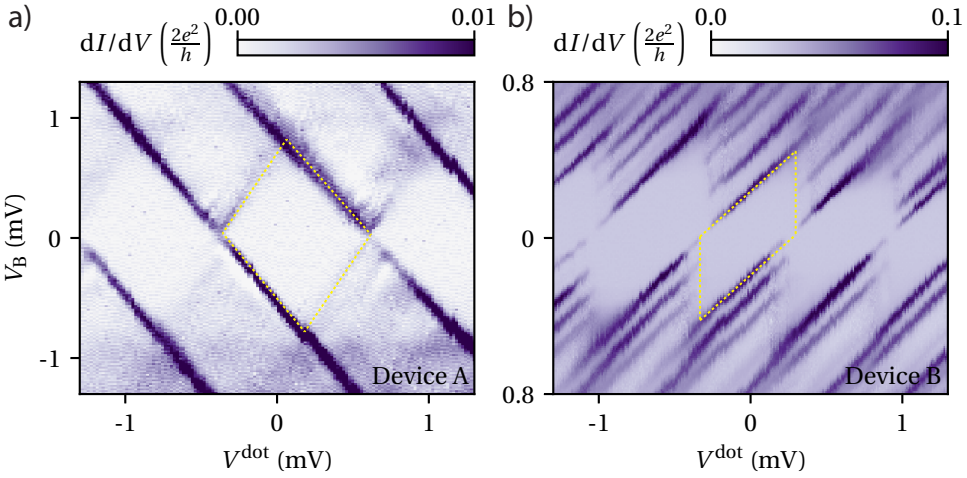


Figure 5.6: **Coulomb blockade measurements on the quantum dots. a)** For device A, the conductance is calculated from the numerical derivative of the measured current. We extract $E_C^{\text{QD}} \approx 300\,\mu\text{eV}$, $\delta = 50 - 150\,\mu\text{eV}$, and $\alpha^{\text{QD}} = 0.8$. **b)** For device B, we obtain $E_C^{\text{QD}} \approx 200\,\mu\text{eV}$, $\delta = 100 - 170\,\mu\text{eV}$, and $\alpha^{\text{QD}} = 0.72$. The pink-dashed lines serve as guide to the eye to indicate a single Coulomb diamond.

Figure 5.7 shows Coulomb diamonds for the SC of device A obtained via current measurements at the same gate settings as the diamond scan shown in Fig. 5.1b of the main

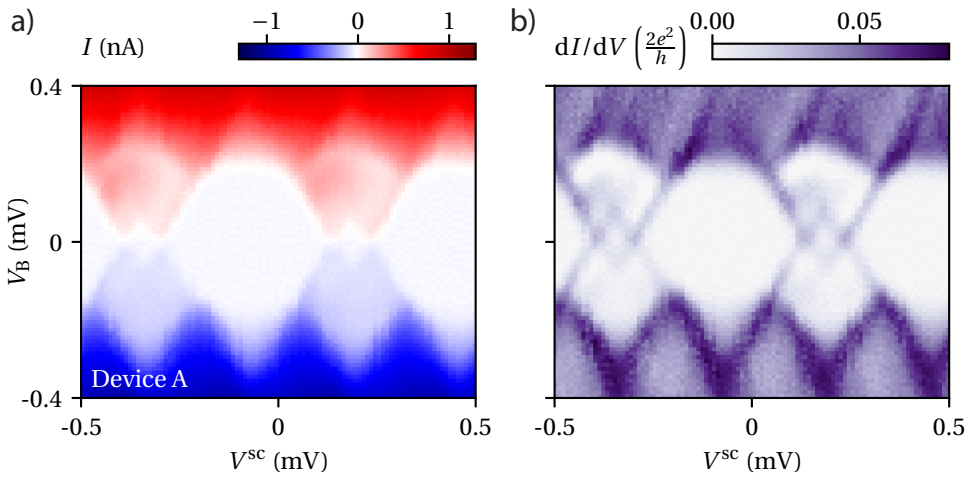


Figure 5.7: **Coulomb blockade measurements of the superconducting island in device A.** Left panel: current data, right panel: differential conductance obtained by taking the numerical derivative of the current data.

5

text. The data in presented in the main text is measured using RF reflectometry from the source of the QD-SC system. The conductance shown here drops back to zero when V_B increase above the height of the small odd diamond. This indicates that for the odd charge states the current is carried by a discrete, subgap state. In contrast, if the current is carried by a continuum of states, the conductance would remain constant.

5.4.4. ADDITIONAL CHARGE STABILITY DIAGRAMS DEVICE A

In this section, we present additional CSDs of the hybrid double dot in device A measured via the resonator connected to the plunger gate of the superconducting island (circuit not shown in Fig. 5.1) (Fig. 5.8). This data is measured simultaneously with the data presented in Fig. 5.2 of the main text, and is used to determine the location of the SC-lead transitions (pink dashed lines in Fig. 5.2).

5.4.5. SIMULATION OF THE CHARGE STABILITY DIAGRAMS

In this section, we discuss the phenomenological model used to simulate the charge stability diagrams shown in Fig. 5.3 of the main text. We start with the Hamiltonian of the QD-SC system

$$\hat{H} = \hat{H}_C + \hat{H}_{BCS} + \hat{H}_T, \tag{5.3}$$

where $\hat{H}_C$ describes the charging energy of the combined system, $\hat{H}_{BCS}$ the superconductivity on the island and the induced superconductivity in the dot, and $\hat{H}_T$ the coupling between the two systems. Note that we neglect the level spacing in both systems. For the superconducting island, this is justified since its estimated level spacing is on the order of several mK. However, for the QD, where $\delta \approx 100\,\mu$eV, this is a large simplification.

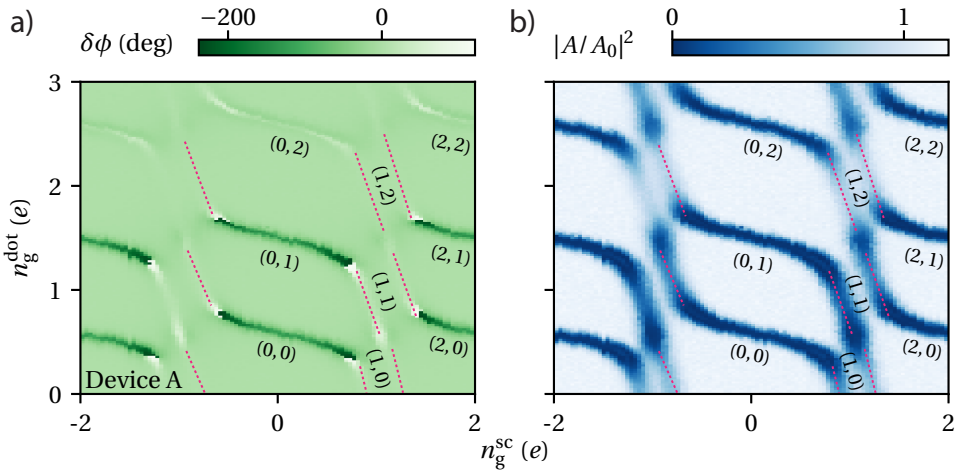


Figure 5.8: **Charge stability diagram measured with gate sensing via the plunger gate of the SC.** Left: phase, right: amplitude. The pink-dashed lines indicate, as guides to the eye, the SC-lead transitions.

We model the charging term by $\hat{H}_\mathrm{C} = \hat{H}_\mathrm{C}^\mathrm{QD} + \hat{H}_\mathrm{C}^\mathrm{SC} + \hat{H}_{\mathrm{C_m}}$

$$\hat{H}_\mathrm{C}^\mathrm{i} = \sum_{n^i} E_\mathrm{C}^i \left(n^i - n_\mathrm{g}^i\right)^2 \tag{5.4}$$

$$\hat{H}_{\mathrm{C_m}} = \sum_{n^\mathrm{SC}, n^\mathrm{QD}} E_{\mathrm{C_m}} \left(n^\mathrm{SC} - n_\mathrm{g}^\mathrm{SC}\right)\left(n^\mathrm{QD} - n_\mathrm{g}^\mathrm{QD}\right) \tag{5.5}$$

where i = QD, SC labels the system; E_C^i is the charging energy, n_g^i the gate charge, and n^i labels the charge state.

We approximate the BCS Hamiltonian by assuming that only the lowest single particle state with energy E_0 is relevant

$$\hat{H}_\mathrm{BCS} \approx \begin{cases} 0 & n^i \text{ is even} \\ E_0^i & n^i \text{ is odd.} \end{cases} \tag{5.6}$$

Note that $E_0 = \Delta$ in case there are no subgap states present on the SC. Usually, $E_0^\mathrm{QD} = 0$, we included this term to be able to model induced superconducting correlations in the quantum dot when the QD-SC coupling is strong.

Lastly, for the tunneling Hamiltonian, we include both $1e$ and $2e$ charge-transfer processes: $\hat{H}_\mathrm{T} = \hat{H}_\mathrm{T}^{1e} + \hat{H}_\mathrm{T}^{2e}$ with

$$\hat{H}_\mathrm{T}^{1e} = \sum_{n^\mathrm{SC}, n^\mathrm{QD}} t_{1e} \left|n^\mathrm{SC} - 1\right\rangle \left\langle n^\mathrm{QD} + 1\right| + \mathrm{h.c.} \tag{5.7}$$

$$\hat{H}_\mathrm{T}^{2e} = \sum_{n^\mathrm{SC}, n^\mathrm{QD}} t_{2e} \left|n^\mathrm{SC} - 2\right\rangle \left\langle n^\mathrm{QD} + 2\right| + \mathrm{h.c.}, \tag{5.8}$$

where t_{1e} (t_{2e}) is the tunneling amplitude for the $1e$ ($2e$) process.

To simulate the charge stability diagrams, we construct a Hamiltonian based of a finite number of charge states $|n^{SC}, n^{QD}\rangle = |-4,-4\rangle, |-4,-3\rangle, \ldots, |4,4\rangle$, using Kwant [67], and numerically solve for its eigenvalues and eigenvectors. We use the eigenvectors to calculate the charge expectation value of the total system which we compare to the data.

ADDITIONAL INFORMATION SIMULATIONS

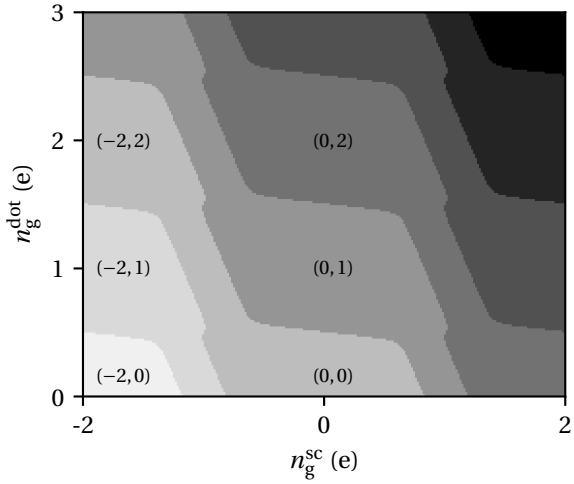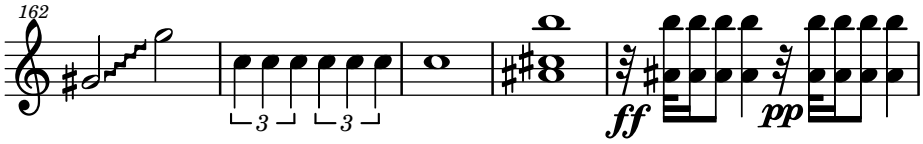


Figure 5.9: **Simulation of the charge stability diagram of Fig 5.2 of the main text.** The gray scale indicates the sum of the charge in the hybrid double dot.

Table 5.2: **Overview of the parameters used in the simulations.** All values are in μeV.

Simulation	E_C^{SC}	E_C^{QD}	E_{C_m}	E_0^{SC}	E_0^{dot}	t_{1e}	t_{2e}
Fig 5.3a	72	230	50	88	0	9	0
Fig 5.3c	72	230	60	88	18	176	308
Fig 5.9	112	500	50	72	0	35	0

6

RAPID MICROWAVE-ONLY CHARACTERIZATION AND READOUT OF QUANTUM DOTS USING MULTIPLEXED GIGAHERTZ-FREQUENCY RESONATORS



Superconducting resonators enable fast characterization and readout of mesoscopic quantum devices. Finding ways to perform measurements of interest on such devices using resonators only is therefore of great practical relevance. We report the experimental investigation of an InAs nanowire multi-quantum dot device by probing GHz resonators connected to the device. First, we demonstrate accurate extraction of the DC conductance from measurements of the high-frequency admittance. Because our technique does not rely on DC calibration, it could potentially obviate the need for DC measurements in semiconductor qubit devices. Second, we demonstrate multiplexed gate sensing and the detection of charge tunneling on microsecond time scales. The GHz detection of dispersive resonator shifts allows rapid acquisition of charge-stability diagrams, as well as resolving charge tunneling in the device with a signal-to-noise ratio of up to 15 in one microsecond. Our measurements show that GHz-frequency resonators may serve as a universal tool for fast tune-up and high-fidelity readout of semiconductor qubits.

The work in this chapter has been published as: D. de Jong, C. G. Prosko, D. M. A. Waardenburg, L. Han, F. K. Malinowski, P. Krogstrup, L. P. Kouwenhoven, J. V. Koski, and W. Pfaff, Rapid microwave-only characterization and readout of quantum dots using multiplexed gigahertz-frequency resonators, Physical Review Applied **16**, 014007 (2021).

6.1. INTRODUCTION

Microwave resonators in the few-gigahertz range are well known as a powerful means to increase the speed with which properties of mesoscopic quantum devices can be read out [44]. In the field of quantum information, resonators in this so-called 'Super High Frequency' (SHF) band have thus enabled the fast and high-fidelity nondemolition readout of quantum bits (qubits)[73, 90, 93, 100], as well as mediating interactions between qubits [137–140]. SHF resonators are also an attractive tool for the fast characterization of quantum devices, because the required tuneup routines are generally time-consuming. Additionally, frequency multiplexing using many high-Q resonators has been established for hardware-efficient mass-characterization of devices [141, 142].

Efficient characterization is particularly relevant for semiconductor quantum devices where many gate electrodes result in a large parameter space. In recent years there have been numerous efforts to utilize SHF resonators for this purpose [108, 143–146] as well as reading out qubit degrees of freedom [71, 95, 126, 143, 147–153]. Despite these successes, however, experiments are still often supplemented with DC or low-frequency measurements to quantitatively extract the DC conductance [154]. As larger-scale devices are developed [155, 156], it is interesting to direct focus to readout and tuneup schemes utilizing SHF resonators only, thus allowing a single framework for all measurements performed on a device.

Here, we present experiments using multiplexed resonators in the range 3–7 GHz coupled to a multiquantum dot (multi-QD) system. Using the resonator response only, we are able to infer quantitatively the DC conductance of the system, and detect single-electron tunneling with high signal-to-noise ratio (SNR) on submicrosecond timescales. The remainder of this paper is organized as follows. In Sec. 6.3 we determine the DC (i.e. zero-frequency) conductance from SHF measurements without any DC calibration data and find agreement with conductance obtained from a DC transport control measurement. In Sec. 6.4, we demonstrate fast multiplexed dispersive gate sensing (DGS) at gigahertz frequencies in a double quantum dot (DQD). This local measurement of charge transitions facilitates fast tuneup of multi-QD systems [156]. Finally, in Sec. 6.5, we attain high SNRs in the detection of charge tunneling in the DQD. State-dependent charge tunneling is a key mechanism for qubit readout in semiconductor qubits [157]. Our optimized resonator design [110], combined with the use of a near-quantum-limited amplifier [89], results in a maximum SNR of 15 in an integration time of 1 μs.

6.2. EXPERIMENTAL SETUP

The device comprises an InAs nanowire with a gigahertz-bandwidth coplanar waveguide resonator [79] coupled to every QD to sense the electronic compressibility of each individual dot. An additional resonator that is galvanically connected to the source of the nanowire is used to probe the admittance of the nanowire. Figures 6.1a and 6.1a show images of the resonators and the multi-QD device, respectively. An approximate lumped-element schematic of the device is shown in Fig. 6.1c. Each resonator is coupled to a central feedline in a hanger geometry and is individually addressable using frequency multiplexing (Fig. 6.1d). The obtained SNR is set by the high resonator bandwidth, optimized resonator coupling quality factors, and a traveling-wave parametric

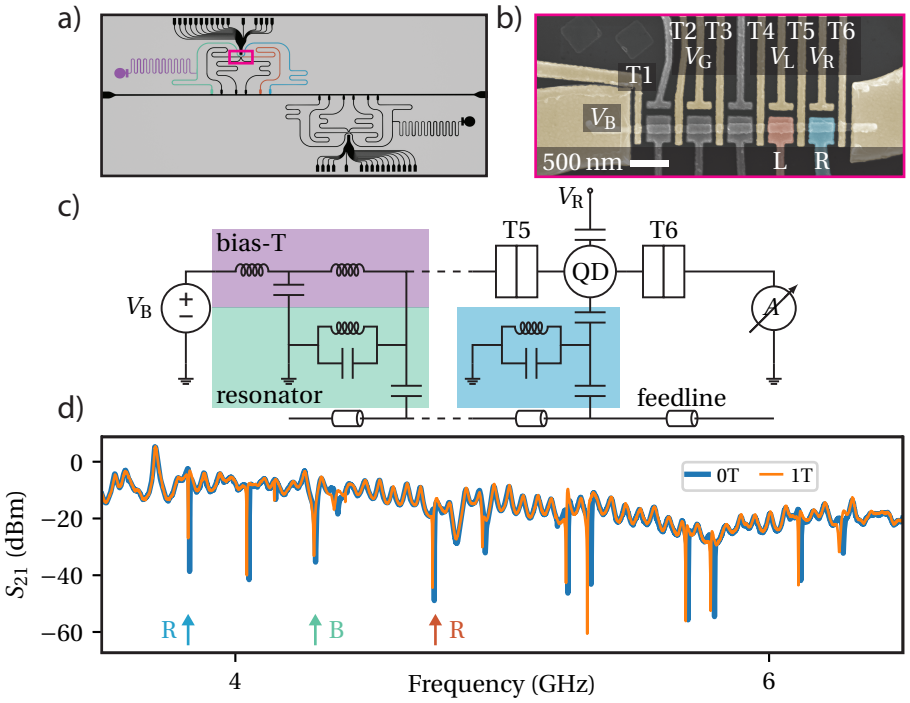


Figure 6.1: **Experimental setup and resonator response. a)** Schematic of the device layout **b)** False-colored electron micrograph of the nanowire and the surrounding gates. **c)** The RF equivalent circuit diagram of the device. The five top gates are coupled to resonators as is the source electrode of the nanowire that can be DC-biased by V_B with a bias-T. The top gates are separated by six tunnel gates such that the nanowire can be pinched off at various positions and quantum dots can be defined. The charge on the quantum dots can be controlled by the side gates. **d)** Transmission through the feedline without magnetic field and at 1 T applied parallel to the plane of the resonators. The arrows L (left), R (right), and B (bias) mark the resonators used here.

amplifier (TWPA) [89] at the base temperature stage of 20 mK of our dilution refrigerator. For further details, see Sec. 3.2.1 and Sec. 6.8.1.

6.3. HIGH-FREQUENCY CONDUCTANCE MEASUREMENTS

We begin by investigating the SHF response of the resonator coupled to the lead in response to changing nanowire conductance [144, 145, 154, 158, 159]. By tuning the gate voltage T2 and keeping the other gates at 0 V we alter the nanowire conductance. This modulates the resonator response, shown in Figures 6.2a and 6.2b, through changes in its load admittance. The DC conductance can be extracted from the load admittance either by building up a calibration map of load admittance and DC conductance, or by quantitatively modeling the resonator circuit [154]. We take the latter approach to maintain independence from DC calibration measurements. To quantify the modulation of the resonator response, we fit the response to a hanger input-output model [74, 76, 160]. The relevant parameters for extracting load admittance are the change in the resonance frequency $\Delta\omega_0$ and the additional photon decay rate $\Delta\kappa_d$ with respect to the pinched-off

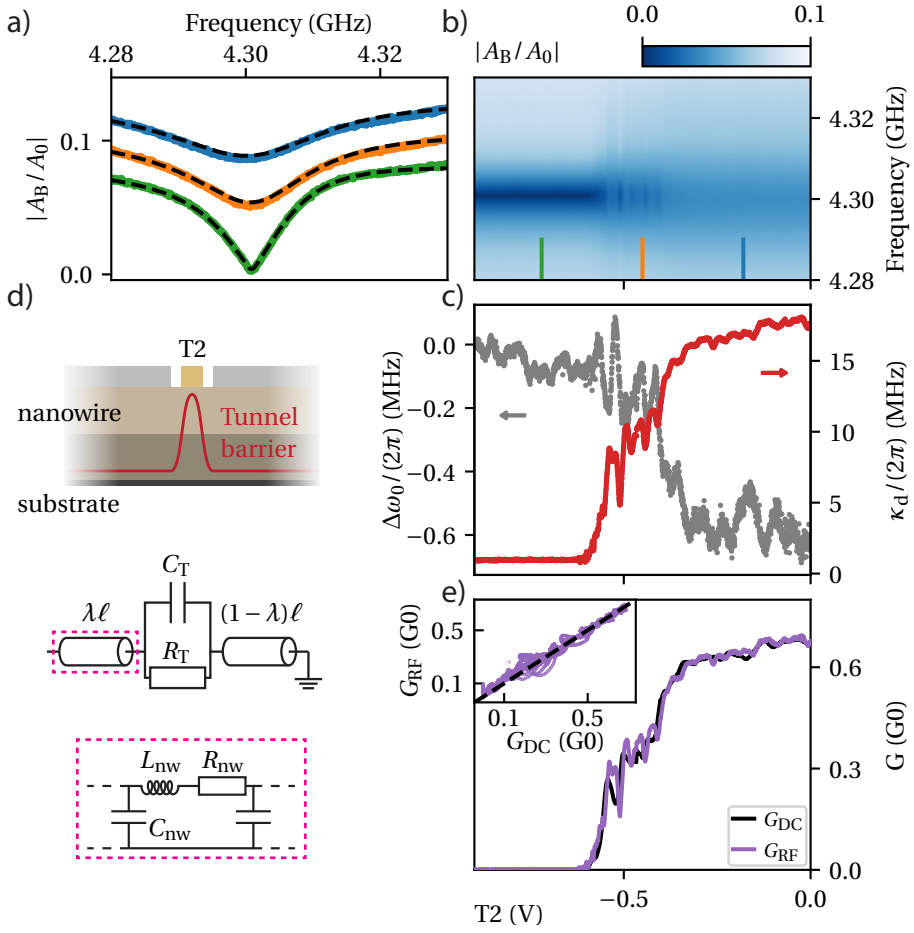


Figure 6.2: **Pinchoff measurements. a**), **b)** Response of the conductance resonator to the tunnel gate voltage T2 and linecuts at the indicated gate voltages in **b)** offset for clarity. The quantity $|A_B/A_0|$ denotes the ratio of measured signal to input signal. **c)** Frequency shift $\Delta\omega_0$ and internal resonator decay κ_d extracted from individual resonator line traces of **b)**. **d)** Schematic of the nanowire for the experiment in **b** with the corresponding lumped-element model used to convert between resonator admittance and conductance G_{RF}. **e)** Conductance G_{DC}, measured with standard voltage-biased current measurements, together with the conductance G_{RF} extracted from **c)**. The inset shows the conductance G_{RF}, as a function of conductance G_{DC}, for the gate response of all tunnel gate voltages T1 through T6. The dashed line indicates $G_{DC} = G_{RF}$. The individual traces are included in Sec. 6.8.6. All measurements in this figure are taken at $V_B = 10\,\text{mV}$ while unused gates are held at 0 V such that only the active tunnel gate can deplete the nanowire.

regime, which is reached by decreasing the gate voltages until κ_d saturates. Representative fits are plotted in Fig. 6.2a and the extracted κ_d and $\Delta\omega_0$ are shown in Fig. 6.2c. The load admittance, Y, can then be calculated by

$$Y = \frac{\pi}{Z_0\omega_0}\left(\frac{1}{2}\Delta\kappa_d - \imath\Delta\omega_0\right), \tag{6.1}$$

which holds for a transmission line resonator of characteristic impedance Z_0 coupled to a high impedance load $1/|Y| \gg Z_0$. We estimate $Z_0 = 116\,\Omega$ from the resonator design. See Sec. 6.8.2 for more details of the procedure outlined above.

Importantly, the load admittance at finite frequency does not directly translate to the DC conductance of the coupled device (i.e. the nanowire). The nanowire itself has an inductive component and the gates surrounding the nanowire add additional shunting capacitive paths to ground, contributing to the load admittance especially for higher frequencies. Our device design with high leverarm gates necessitates compensating for these contributions explicitly, in contrast to the experiments in Refs. [144, 145, 154]. To account for these effects, we model the load admittance Y as in Fig. 6.2d, describing an effective transmission line formed by the nanowire split by a tunnel junction. We denote the series resistance, inductance and parallel capacitance per unit length of this transmission line by R_{nw}, L_{nw} and C_{nw} and introduce $Z_{nw} = \ell(R_{nw} + \imath\omega L_{nw})$ with ℓ the nanowire length. The DC conductance of the nanowire can be calculated from the impedance added by the nanowire itself, Z_{nw}, and the impedance of the tunnel junction Z_T.

The relation between Z_T and Y depends on the fractional position of the tunnel junction along the nanowire, which we parameterize by λ. Explicitly, the relation is given by

$$Z_T = \frac{\frac{Z_{nw}}{\gamma\ell}}{\cosh((1-\lambda)\gamma\ell)} \frac{\frac{YZ_{nw}}{\gamma\ell}\sinh(\gamma\ell) - \cosh(\gamma\ell)}{\sinh(\lambda\gamma\ell) - \frac{YZ_{nw}}{\gamma\ell}\cosh(\lambda\gamma\ell)}, \tag{6.2}$$

where $\gamma \equiv \sqrt{(R_{nw} + \imath\omega L_{nw})\imath\omega C_{nw}}$ denotes the complex propagation constant.

The constants Z_{nw} and $\gamma\ell$ are determined from two SHF calibration measurements. For the first calibration measurement, the load impedance Y_o is measured when all gates are open at 0 V, corresponding to the limit that $Z_T = 0$. For the second calibration measurement, the load impedance Y_p as $|Z_T| \to \infty$ and $\lambda = 1$ is measured by tuning the rightmost gate voltage T6 into pinchoff. Solving the resulting two equations for $\gamma\ell$ and Z_{nw} yields

$$\gamma\ell = \operatorname{arctanh}\left(\sqrt{\frac{Y_p}{Y_o}}\right) \text{ and } Z_{nw} = \frac{\gamma\ell}{\sqrt{Y_p Y_o}}. \tag{6.3}$$

See Sec. 6.8.5 for more information. Using Eq. (6.2) and Eq. (6.3), we then extract Z_T from the admittance Y. We model the junction as a resistor R_T and capacitor C_T in parallel such that $Z_T^{-1} \equiv 1/R_T + i\omega C_T$ [48], and then determine the DC-equivalent conductance as

$$G_{RF}^{-1} = \mathrm{Re}(Z_{nw}) + 1/\mathrm{Re}(Z_T^{-1}). \tag{6.4}$$

To validate our method to infer the conductance, we compare it with the conductance obtained from a control experiment using conventional DC-current detection. Fig. 6.2e

shows the conductance extracted from DC measurements G_{DC} and the DC conductance extracted from the resonator response G_{RF}. Excellent agreement is observed between G_{RF} and G_{DC} for data from pinchoff traces of T1 through T6, changing λ according to the position of the gate, shown in the inset of Fig. 6.2e.

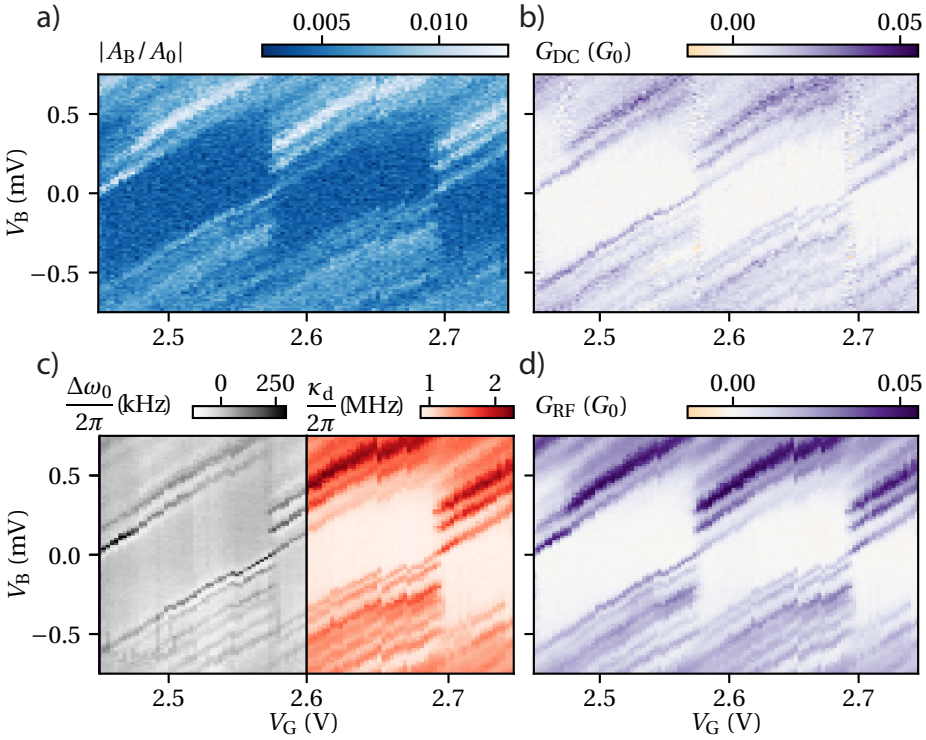


Figure 6.3: **Coulomb blockade diamonds measured in a single quantum dot. a)** Single-frequency response of the resonator. **b)** G_{DC} measurements obtained with standard lock-in techniques. **c)** Frequency shift Δf and resonator decay rate κ_d extracted from frequency traces. **d)** Conductance G_{RF} extracted from resonator data in **c)**.

Applications of RF conductance are not limited to measuring the impedance of tunnel gates [146, 161–163]. As an example, we probe a quantum dot by tuning T2 and T3 into the tunneling regime and modulating the gate voltage V_G, leaving the other gates at 0 V. We show the amplitude response of the lead resonator on resonance in Fig. 6.3a as a function of bias voltage V_B and gate voltage V_G. Even though the amplitude response is not translated into DC conductance here, it shows all the qualitative features present in the control data measured by DC lock-in conductance (Fig. 6.3b), including the excited states of the quantum dot. The amplitude response of Fig. 6.3a is part of a full frequency trace, measured to also allow for a quantitative comparison between the DC results and the resonator response. From these traces, the frequency shift $\Delta\omega_0$ and photon decay $\Delta\kappa_d$ are extracted and shown in Fig. 6.3c. We use the model defined by Eqs. (6.1 - 6.4) to obtain G_{RF}, shown in Fig. 6.3d. This is the same model used for the tunnel junction

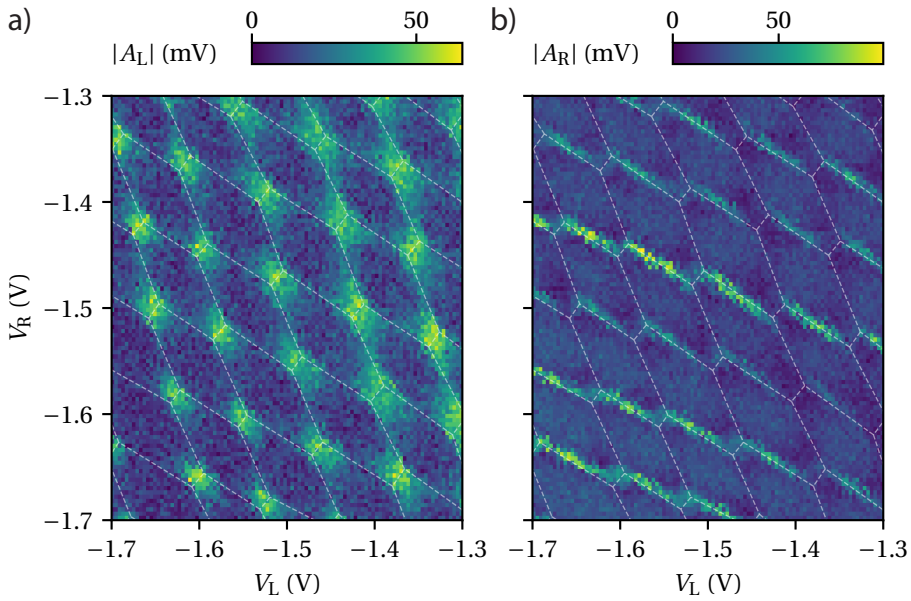


Figure 6.4: **Charge stability diagram measured using multiplexed gate-based readout in the double dot regime. a), b)** Amplitude response of the resonators coupled to the two rightmost quantum dots. Readout power in the feedline is −105 dBm per multiplexed resonator with an integration time of 3 µs. The dimensions of this dataset are 101 × 101 points yielding a total integration time of 30 ms excluding overhead from gate settling time, set by low-pass filters on the gate wiring. The dashed lines are guides to the eye delineating the different charge configurations of the double dot and are identical in **a)** and **b)**.

scans of Fig. 6.2. Note that we neglect here the finite width occupied by the quantum dot and its internal structure; nevertheless we observe reasonable agreement between G_{RF} and G_{DC}.

6.4. RAPID MULTIPLEXED REFLECTOMETRY

We now move on to the capacitively coupled gate resonators and investigate DGS in the double quantum dot (DQD) regime [91, 92, 95, 97–99, 106, 122, 152, 164–166]. To tune the system into a DQD, the gate voltages T4, T5, and T6 are each decreased into the tunneling regime. Accordingly, two quantum dots are formed under the rightmost two top gates in the nanowire [48].

A resonator is coupled to both dots to sense the electronic compressibility of the individual dots [133, 167]. In Fig. 6.4 we show a charge stability diagram (CSD) using V_L and V_R to change the electron occupation of the DQD. We perform pulsed readout with an integration time of 3 µs per point, constituting a total data acquisition time of 30 ms for the entire CSD [108, 109]. The data acquisition is frequency-multiplexed for both resonators such that the data in Figures 6.4a and 6.4b are measured simultaneously [78, 156]. This not only reduces the measurement time, but multiplexing also guarantees that the measurements in Figures 6.4a and 6.4b correspond to the exact same physical regime, regardless of charge jumps and gate hysteresis. To emphasize the correspon-

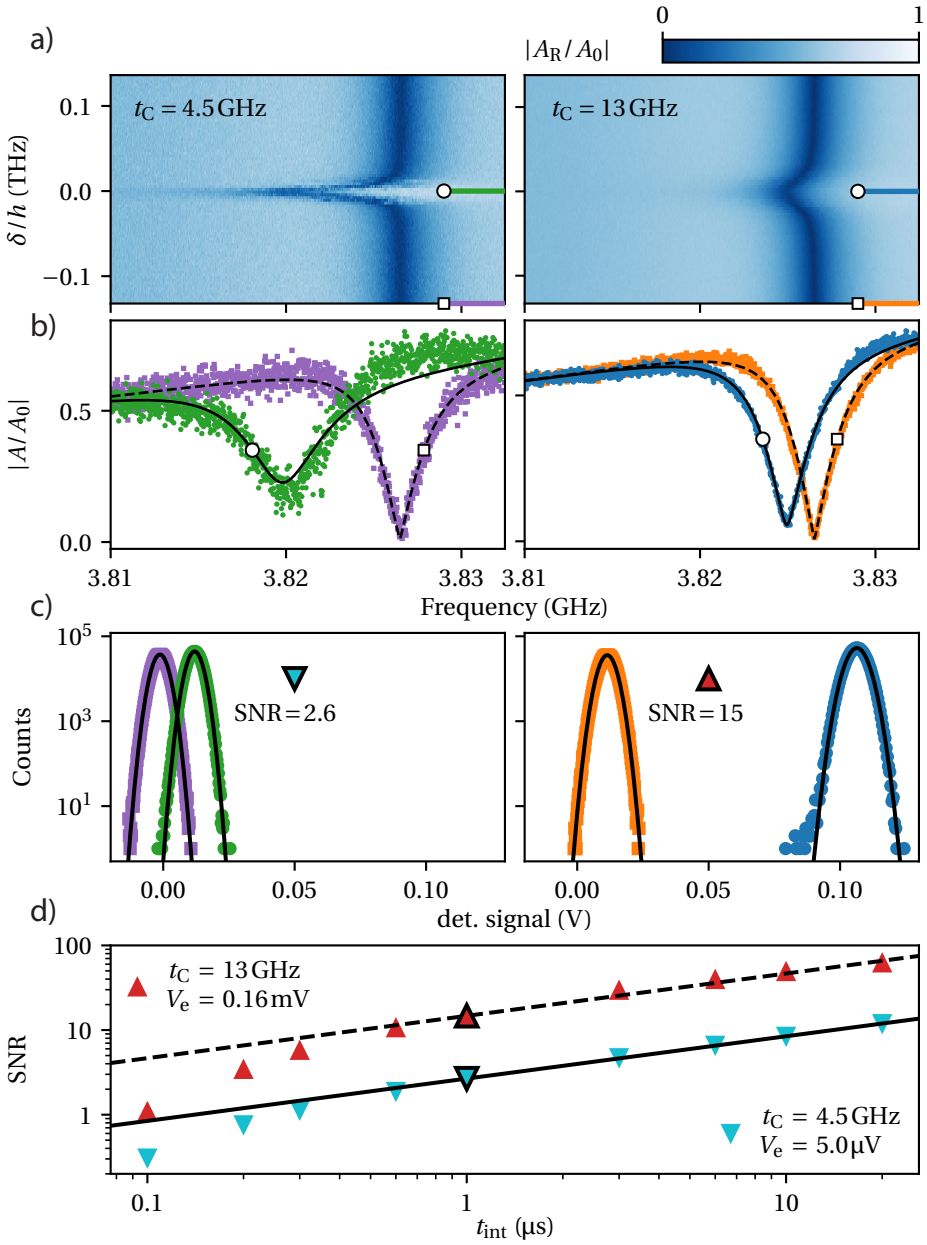


Figure 6.5: **Readout SNR. a)** Amplitude response as a function of detuning δ of the resonator coupled to the right dot for the two different tunnel coupling regimes. **b)** Linecuts for Coulomb blockade (square marker) and on resonance (circle marker) together with fits to the theoretical model. **c)** Histograms of the resonator responses in Coulomb blockade and charge degeneracy, with pulse length of 1 μs. Responses are acquired with a probe frequency tuned to resonance for the Coulomb blockade case, at approximately 3.826 GHz. **d)** Attained SNR on the right dot's resonator, defined as $\Delta/(2\sigma)$, as a function of measurement pulse length. Optimized with excitation voltage as a free parameter (red, up triangles) and optimized at fixed excitation voltage of 5μV (aqua, down triangles).

dence between Figures. 6.4a and 6.4b, the same guides to the eye outlining stable charge configurations are drawn in both panels.

Resonators are only sensitive to charge transitions involving the quantum dots to which they are coupled. Therefore, both resonators detect the interdot transitions; however, transitions from the right dot to the right electrode are detected only by the resonator connected to the right dot. Here, the resonator connected to the left dot does not respond to transitions between the left dot and the left electrode. We attribute this to a mismatched left dot - left electrode tunnel coupling. Hence multiplexing also enables spatial correlation of electron tunneling by comparing the DGS signal from each gate's resonator, effectively 'tracking' the electron through the device.

6.5. SIGNAL TO NOISE

Finally, we investigate the attainable SNR for resolving charge tunneling with DGS by changing detuning from charge degeneracy in the DQD. This procedure serves as a proxy for different qubit states in schemes where readout is based on state-dependent tunneling [25, 26, 152, 159, 164, 168]. Because actual qubit systems will have limitations on the readout power [157] we investigate the SNR both at a fixed 'low' excitation voltage in the resonator, $V_e = 5\,\mu V$, as well as at an optimized excitation voltage, $V_e = 0.16\,mV$. These excitation voltages are calculated from the generator power and line attenuation in addition to the resonator frequency and coupling capacitance to the feedline.

We fix the total charge in the system by pinching off gates on either side of the DQD. The only remaining transitions are interdot transitions occurring through a tunnel coupling denoted by t_C. The resonator response as a function of the energy detuning δ from the interdot transition is shown in Fig. 6.5a. We determine t_C by fitting the resonator response to an input-output model [71], see Sec. 6.8.2. Linecuts of the fit results and measurement data are shown in Fig. 6.5b.

We define SNR as the change in signal between charge degeneracy and Coulomb blockade divided by the noise. To measure it, we perform a series of pulsed measurements of I and Q with a pulse time of t_{int} at both Coulomb blockade and charge degeneracy, and show the obtained histograms for an integration time of $t_{int} = 1\,\mu s$ in Fig. 6.5c. These histograms are fit with a Gaussian to extract the separation between the Gaussian peaks Δ in the IQ plane as well as their average standard deviation σ representing the width. The SNR is given by $\Delta/(2\sigma)$. More details are given in Sec. 6.8.7.

In Fig. 6.5d we plot the dependence of SNR on t_{int}, which approaches a square-root dependence for longer times. We attribute the discrepancy between attained SNR and a square-root dependence for pulse times shorter than 1 µs to the finite bandwidth of the resonators. For these pulse lengths, the resonator cannot reach a steady-state photon population, limiting the signal available for readout.

Next, we compare the observed SNR with expected theoretical limits. The change in signal at the feedline level $\Delta_f = \Delta/G_{sys}$ — with G_{sys} the gain of the amplification chain in the system — can never exceed the total voltage swing in the feedline V_f. The fit to the data in Fig. 6.5a, used to extract t_C, also provides a direct measurement of the ratio $\Delta_f/V_f = 0.89$, close to the absolute maximum. In other words, the resonator is coupled near optimally for this tunnel coupling, such that its external coupling rate is nearly equal to the dispersive shift.

The achievable SNR is then set by Δ_f together with noise temperature, T_N, and readout time, t_{int}, as

$$\mathrm{SNR} = \frac{\Delta_f \sqrt{t_{int}}}{2\sqrt{Z k_B T_N}}, \tag{6.5}$$

where $Z = 50\,\Omega$ is the impedance of the feedline [169], see Sec. 6.8.8. The SNR $\simeq 2.6$ found in Fig. 6.5c together with the readout time $t_{int} = 1\,\mu s$ and the deduced approximate voltage swing in the feedline, $V_f = 0.15\,\mu V$ corresponds to a noise temperature estimate of $T_N = 1\,K$. Without the use of a TWPA, we expect that the noise temperature would increase to $T_N \approx 4\,K$. To improve the SNR, one can increase either the readout time or readout power in accordance with Eq. (6.5), as shown in Fig. 6.5d. In practice, limits to these two parameters will be determined by the specific qubit implementation. Specifically, by optimizing the excitation voltage and tunnel coupling together, a SNR of 15 is achieved at $V_e = 0.16\,mV$.

6.6. CONCLUSIONS

We show the characterization of an InAs nanowire multi-QD system using gigahertz-frequency sensing. Probing the finite frequency admittance of the nanowire allows us to infer the low-frequency conductance with good accuracy, even without calibration from DC measurements. Further, we show high-SNR dispersive sensing on timescales near the bandwidth limit set by the Q factor of the resonators. Besides the use for qubit devices, we envision that fast multiplexed readout of quantum devices may be used for more complex sensing schemes. In particular, rapid simultaneous conduction of multiple local measurements could facilitate unique quantum transport experiments because they provide spatial information about tunneling processes. For example, probing two quantum dots at either end of a central charge island, tunneling events into the outer dots may be correlated [170, 171]. We conclude that multiplexed SHF resonators may serve as a complete toolset for characterization and readout of semiconductor quantum devices, and present intriguing opportunities for developing high-speed quantum transport measurement schemes. Original data are available via the online data repository [172].

6.7. ACKNOWLEDGMENTS

We thank D. Bouman and J.D. Mensingh for nanowire deposition and A. Bargerbos for valuable comments on the manuscript. We further thank N.P. Alberts, O.W.B. Benningshof, R.N. Schouten, M.J.Tiggelman, and R.F.L. Vermeulen for valuable technical assistance. This work is supported by the Netherlands Organization for Scientific Research (NWO) and Microsoft.

6.8. SUPPLEMENTAL MATERIAL

6.8.1. SAMPLE FABRICATION AND EXPERIMENTAL SETUP

The experimental setup is schematically shown in Fig. 6.6. On-chip superconducting coplanar waveguide (CPW) resonators are fabricated from a 20 nm NbTiN layer using reactive ion etching, similar to Ref. [79] ensuring magnetic field compatibility. The res-

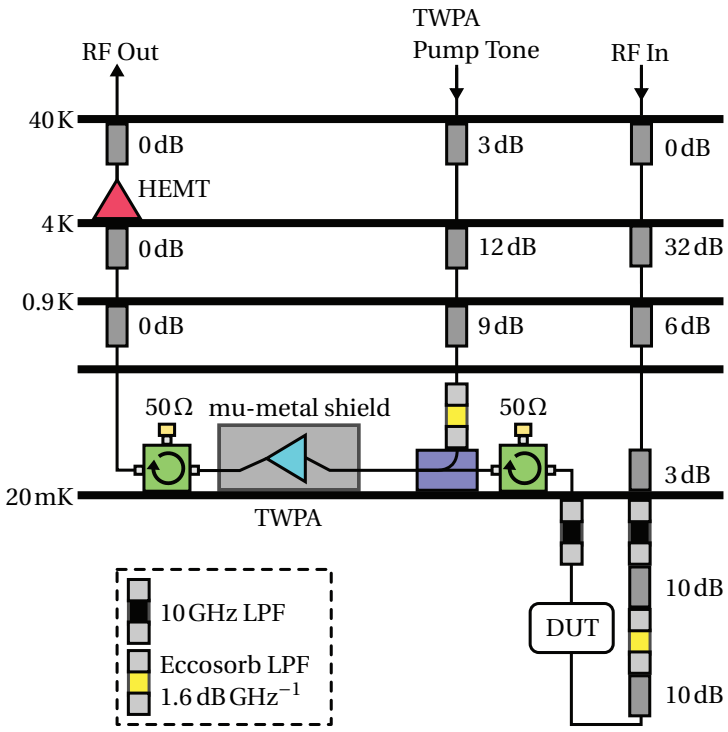


Figure 6.6: **RF circuit of the dilution refrigerator.** An RF signal generated either by a vector network analyzer or Quantum Machines OPX pulse generator is attenuated at each stage of the refrigerator on its way to the device under test (DUT) at base temperature. The signal is amplified on the way out of the fridge first by a traveling wave parametric amplifier (TWPA) at base temperature, driven by a GHz-frequency pump tone, and then by a 4 to 8 GHz bandwidth high electron mobility transistor (HEMT) amplifier at the 4 K plate. In front of and behind the TWPA are circulators (green) and a directional coupler (violet) designed to reduce back-action of the TWPA on the DUT and attenuate any noise traveling down the output and pump tone lines. Low pass filters are also present to reduce noise above the measurement bandwidth.

onator design is half-wavelength with hanger-style geometry, with each resonator coupled to a central feedline. The resonators used for DGS have an external coupling factor around $\kappa_{\text{ext}} \simeq 10\,\text{MHz}$ to maximize readout signal.

An InAs nanowire with an epitaxial Al shell is deposited using a micromanipulator. The superconducting shell is removed everywhere except over the middle dot using a PMMA etch mask and a 70 s wet etch using MF-321 developer. However, no superconducting effects are observed in this experiment. We attribute the absence of superconductivity to over-etching of the Al shell on the wire. Contacts are fabricated by in-situ argon milling followed by evaporating 10 nm Ti then 150 nm Au. A 10 nm AlOx dielectric is selectively deposited on the nanowire, away from the resonators to avoid additional dielectric loss. Lastly, top gates are evaporated in the same way as the contacts. To minimize the noise temperature in our measurements we use a TWPA [89] on the base temperature stage of a dilution refrigerator operating at 20 mK. Additionally, a high electron

mobility transistor amplifier at 4 K is used to further amplify the signal.

6.8.2. FITTING PROCEDURE FOR RESONATOR RESPONSE

In this section we describe the complete fitting procedure for the measured resonator response. The model used for fitting the transmission S_{21} through a feedline with a hanger-style resonator is given by[74, 76, 160]:

$$S_{21} = e^{\imath(\theta_0+\theta_1\omega)} s_0 \left(1 + s_1 \frac{\omega-\omega_0}{\omega_0}\right)\left(1 - \frac{1}{2}\frac{\imath\kappa_{\text{ext}}}{\imath(\kappa_{\text{ext}}+\kappa_{\text{d}})/2 - \omega + \omega_0}\right). \tag{6.6}$$

The probe frequency is denoted by ω and the resonator frequency by ω_0.

To account for the line delay, θ_0 and θ_1 account for a linear offset in phase. Similarly, we account for a linear amplitude offset by s_0 and s_1. The photon decay is represented by κ_{d} and the external coupling factor κ_{ext} is complex to account for impedance mismatches.

The calibration frequency trace used for the data in Fig. 6.2 is shown in Fig. 6.7a together with a fit to Eq. (6.6). We find $\omega_0/2\pi = 4.3\,\text{GHz}$, $\kappa_{\text{ext}}/2\pi = (18.6 - 3.4\imath)\,\text{MHz}$ and $\kappa_{\text{d}}/2\pi = 0.9\,\text{MHz}$. The calibration measurement defines the zero-point of $\Delta\omega_0$ and $\Delta\kappa_{\text{i}}$. We also use the calibration to hold all parameters except for ω_0 and κ_{i} fixed when fitting the frequency traces for obtaining the pinch-off data, such as in Fig. 6.2b. The Root-mean-square error is used to identify points where the fitting algorithm fails to identify the correct resonator line shape. Using this method, we have identified and excluded 7 outliers from subsequent analysis and plotting compared to the 15006 fits used for Fig. 2.

For fitting the dispersive shift as a function of detuning δ, in Fig. 6.5 we add the contribution of the DQD to Eq. (6.6). This contribution is accounted for by substituting $\kappa_{\text{d}} \to \kappa_{\text{d}} - 2\imath g\chi$ in Eq. (6.6) caused by coupling to the susceptibility of the DQD [71] with

$$g\chi = \frac{4g_0^2 t_{\text{C}}^2/\Omega^2}{\omega_0 - \Omega + \imath\gamma/2}, \tag{6.7}$$

where g is the effective coupling strength and χ the susceptibility of the DQD. Furthermore, g_0 is the Jaynes-Cummings coupling, $\Omega = \sqrt{4t_{\text{C}}^2 + \delta^2}$ is the DQD energy splitting, t_{C} the tunnel coupling between the dots and γ the decoherence rate.

6.8.3. CORRESPONDENCE BETWEEN Y AND RESONATOR RESPONSE

Here we relate the nanowire load admittance to the quality factor and resonance frequency of a resonator connected to its lead. Throughout the following derivations, we assume that within the small window of frequencies used to fit our resonator's resonance frequency and quality factor, the sample load admittance Y is constant. The resonator is modeled as a transmission line capacitively coupled to a central feedline and terminated by a load impedance Y^{-1} determined by the nanowire. Assuming the feedline coupler to behave as a lumped element capacitance C_{c}, the input impedance Z_{in} of the terminated resonator and coupler is [169]:

$$Z_{\text{in}} = \frac{1}{\imath\omega C_{\text{c}}} + Z_0 \frac{1 + Z_0 Y \tanh(\gamma_{\text{r}}\ell_{\text{r}})}{Z_0 Y + \tanh(\gamma_{\text{r}}\ell_{\text{r}})}, \tag{6.8}$$

where Z_0 is the line's characteristic impedance, $\gamma_r \equiv \alpha_r + \imath\beta_r$ is the complex propagation constant, and ℓ_r is the length of the resonator. Note that $\beta_r = \omega/v_p$ where v_p is the phase velocity in the transmission line, while α_r quantifies internal losses. To simplify the above expression, we first note the trigonometric relation

$$\begin{aligned}\tanh(\alpha_r\ell_r + \imath\beta_r\ell_r) &= \frac{\sinh(\alpha_r\ell_r)\cos(\beta_r\ell_r) + \imath\cosh(\alpha_r\ell_r)\sin(\beta_r\ell_r)}{\cosh(\alpha_r\ell_r)\cos(\beta_r\ell_r) + \imath\sinh(\alpha_r\ell_r)\sin(\beta_r\ell_r)} \\ &\sim \frac{\alpha_r\ell_r\cos(\beta_r\ell_r) + \imath\sin(\beta_r\ell_r)}{\cos(\beta_r\ell_r) + \imath\alpha_r\ell_r\sin(\beta_r\ell_r)}\end{aligned} \tag{6.9}$$

where we have assumed small internal losses in the resonator, $\alpha_r\ell_r \ll 1$. Since the load admittance is assumed to be small, our resonator nearly has an open at one end. Consequently, the effect of Y should be that of a perturbed $\lambda/2$ resonator. In this case, for small detuning $\delta\omega$ from the resonance frequency ω_0, $\beta_r\ell_r \sim \pi + \pi\delta\omega/\omega_0$ [169]. Since Y is a small perturbation of the load admittance away from zero, it will shift the resonance frequency only slightly, in which case it is still true that $\beta_r\ell_r \sim \pi + x$ where x is a small number. Applying this approximation to Eq. 6.9, we find $\tanh(\gamma_r\ell_r) \sim \alpha_r\ell_r + \imath\tan(\beta_r\ell_r)$. Finally, we assume ω is near resonance such that we may apply the limit $\tan(\beta_r\ell_r) \ll 1$ by the above argument, which in combination with our assumption of small load admittance $Y \ll Z_0^{-1}$ and losses $\alpha_r\ell_r \ll 1$ simplifies Eq. 6.8 to:

$$Z_{in} \sim \frac{1}{\imath\omega C_c} + \frac{Z_0}{Z_0 Y + \alpha_r\ell_r + \imath\tan(\beta_r\ell_r)} = \frac{1}{\imath\omega C_c} + \frac{Z_0}{\alpha_{eff}\ell_r + \imath\left[\tan(\beta_r\ell_r) + Z_0\mathrm{Im}(Y)\right]} \tag{6.10}$$

to first order in these small parameters. Above, we defined the effective dissipation constant $\alpha_{eff}\ell_r \equiv \alpha_r\ell_r + Z_0\mathrm{Re}(Y)$.

Next, we determine the relation between $\mathrm{Im}(Y)$ and the resonance frequency ω_0. At resonance, the imaginary part of Z_{in} disappears, so we solve this condition for ω_0:

$$0 = \mathrm{Im}(Z_{in}) = -\frac{1}{\omega_0 C_c} - Z_0\frac{\tan(\omega_0\ell_r/v_p) + Z_0\mathrm{Im}(Y)}{(\alpha_{eff}\ell_r)^2 + (\tan(\omega_0\ell_r/v_p) + Z_0\mathrm{Im}(Y))^2}. \tag{6.11}$$

With the foresight that internal quality factors of our resonators will be related to $\alpha_{eff}\ell_r$ through $\alpha_{eff}\ell_r = \pi/(2Q_i)$, from resonator fits we may estimate that $\alpha_{eff}\ell_r < 0.002$ even when the nanowire is completely open. In our resonator chip, coupling capacitances are on the order of 40 fF, so that at few-GHz frequencies and when $Z_0 = 116\,\Omega$, $\omega_o C_c Z_0 \approx 0.03$ to 0.1 is a small parameter, but still much larger than $\alpha_{eff}\ell_r$. Rearranging and neglecting terms above first order in $\alpha_{eff}\ell_r/(Z_0\omega C_c)$, we obtain the implicit solution:

$$\frac{\omega_0\ell_r}{v_p} = n\pi - \arctan\left(Z_0\mathrm{Im}(Y) + \omega_0 C_c Z_0\right), \quad n \in \mathbb{Z} \tag{6.12}$$

The smallest substantial resonance frequency occurs for $n = 1$, constituting the GHz-range resonances of interest. Taylor expanding in the small parameters $Z_0\mathrm{Im}(Y)$ and $\omega_0 C_c Z_0$, we see then that the coupling capacitance serves only to impose a constant perturbation to the bare resonance frequency, defined as $\omega_0^* \equiv \omega_0|_{\mathrm{Im}(Y)=0} = \pi(\ell_r/v_p + C_c Z_0)^{-1}$:

$$\omega_0 = \omega_0^*\left(1 - \frac{Z_0\mathrm{Im}(Y)}{\pi}\right). \tag{6.13}$$

At frequencies near resonance such that $\omega = \omega_0 + \delta\omega$ with $\delta\omega \ll \omega_0$, Eq. 6.10 is asymptotic to:

$$Z_{\text{in}} \sim \frac{1}{\imath\omega C_{\text{c}}} + \frac{Z_0}{\alpha_{\text{eff}}\ell_{\text{r}} + \imath\pi\delta\omega/\omega_0}, \qquad \delta\omega \ll \omega_0,\ \alpha_{\text{eff}}\ell_{\text{r}} \ll Z_0\omega_0 C_{\text{c}} \ll 1, \tag{6.14}$$

which is the input impedance of a capacitively coupled parallel LRC resonator circuit near resonance of internal quality factor $Q_i = \pi/(2\alpha_{\text{eff}}\ell_{\text{r}})$ [169]. The internal quality factor is related to the photon decay rate by $\kappa_{\text{d}} \equiv \omega_0/Q_i = 2\omega_0\alpha_{\text{eff}}\ell_{\text{r}}/\pi$. From the definitions of $\alpha_{\text{eff}}\ell_{\text{r}}$ and ω_0, we can thus relate the device admittance to resonator parameters through:

$$Y = \frac{1}{Z_0}\left(\alpha_{\text{eff}}\ell_{\text{r}} - \alpha_{\text{r}}\ell_{\text{r}}\right) - \imath\frac{\pi}{Z_0\omega_0}\left(\omega_0 - \omega_0^*\right) \equiv \frac{\pi}{Z_0\omega_0}\left(\frac{1}{2}\Delta\kappa_{\text{d}} - \imath\Delta\omega\right), \tag{6.15}$$

valid to first order in $\Delta\omega/\omega_0$, where $\Delta\omega \equiv \omega_0 - \omega_0^*$ and $\Delta\kappa_{\text{d}} \equiv \kappa_{\text{d}} - 2\omega_0\alpha_{\text{r}}\ell_{\text{r}}/\pi$. In other words, load conductance is proportional to shifts in the resonator's internal decay factor, while its susceptance is proportional to shifts in the resonance frequency.

6.8.4. DERIVATION OF G_{RF}

Since the nanowire device is covered at most points by a capacitively coupled gate layer of uniform thickness (excluding the small gaps between gates), we model the nanowire as a highly resistive transmission line, and aim to solve for its admittance Y. As per the lumped element model of Fig. 6.2d, we parameterize this with a resistance, inductance, and capacitance per unit length of R_{nw}, L_{nw}, and C_{nw}, respectively. At a fraction λ along the wire's length ℓ, we include a lumped element impedance Z_{T}, modeling a cutter gate or quantum dot.

As a transmission line, on either side of Z_{T} the nanowire obeys the telegrapher equations [169]:

$$\frac{\mathrm{d}V(x)}{\mathrm{d}x} = -Z_{\text{nw}}I(x)/\ell \text{ and } \frac{\mathrm{d}I(x)}{\mathrm{d}x} = -\imath\omega C_{\text{nw}}V(x), \tag{6.16}$$

at every point x along the wire's length, with $x = 0$ denoting the source lead. Above, we have assumed phasor solutions of the voltage v with respect to ground and current i through the wire so that $v(x,t) = V(x)e^{i\omega t}$ and $i(x,t) = I(x)e^{\imath\omega t}$. On either side of the impedance Z_{T}, these coupled differential equations have the solution:

$$V(x) = \begin{cases} V_s^+ e^{-\gamma x} + V_s^- e^{\gamma x} & x < \lambda l \\ V_d^+ e^{-\gamma x} + V_d^- e^{\gamma x} & x > \lambda l \end{cases}, \; I(x) = \begin{cases} \frac{\gamma\ell}{Z_{\text{nw}}}\left(V_s^+ e^{-\gamma x} - V_s^- e^{\gamma x}\right) & x < \lambda\ell \\ \frac{\gamma\ell}{Z_{\text{nw}}}\left(V_d^+ e^{-\gamma x} - V_d^- e^{\gamma x}\right) & x > \lambda\ell \end{cases} \tag{6.17}$$

The nanowire's input admittance is $Y = I(0)/V(0)$ and is fully determined by the boundary condition of a grounded wire $V(\ell) = 0$, current continuity just before and after Z_{T}, and Ohm's law across Z_{T}. Combined, these three conditions allow us to solve for all constants V_s^-, V_d^-, and V_d^+ in terms of V_s^+. In particular:

$$V_s^- = V_s^+ \left[\frac{\frac{Z_{\text{T}}\gamma\ell}{Z_{\text{nw}}}\left(e^{-2\gamma\lambda\ell} + e^{-2\gamma\ell}\right) - 2e^{-2\gamma\ell}}{\frac{Z_{\text{T}}\gamma\ell}{Z_{\text{nw}}}\left(1 + e^{-2\gamma(1-\lambda)\ell}\right) + 2}\right] \tag{6.18}$$

After substituting Eq. 6.17 into the definition of Y, we arrive at the expression

$$Y = \frac{\gamma\ell}{Z_{\mathrm{nw}}}\left(\frac{V_s^+ - V_s^-}{V_s^+ + V_s^-}\right) = \frac{\gamma\ell}{Z_{\mathrm{nw}}}\left[\frac{\cosh(\gamma\ell) + \frac{Z_{\mathrm{T}}\gamma\ell}{Z_{\mathrm{nw}}}\sinh(\gamma\lambda\ell)\cosh(\gamma(1-\lambda)\ell)}{\sinh(\gamma\ell) + \frac{Z_{\mathrm{T}}\gamma\ell}{Z_{\mathrm{nw}}}\cosh(\gamma\lambda\ell)\cosh(\gamma(1-\lambda)\ell)}\right]. \tag{6.19}$$

Finally, this expression may be rearranged to yield Eq. 6.2. Together, Eq. 6.2 and Eq. 6.4 yield an explicit formula for G_{RF}. Substituting the Z_{T} result into Eq. 6.4 we obtain:

$$G_{RF} = \frac{|z_\lambda|\cos(\arg[z_\lambda] - \arg[z_1])}{\mathrm{Re}(Z_{\mathrm{nw}})|z_\lambda|\cos(\arg[z_\lambda] - \arg[z_1]) + |z_1|}. \tag{6.20}$$

Above, the parameters

$$z_1 \equiv \sinh(\gamma\ell)\,Y - (\gamma\ell/Z_{\mathrm{nw}})\cosh(\gamma\ell), \tag{6.21}$$

and

$$z_\lambda \equiv (\gamma\ell/Z_{\mathrm{nw}})\cosh(\gamma(1-\lambda)\ell)\left[(\gamma\ell/Z_{\mathrm{nw}})\sinh(\gamma\lambda\ell) - \cosh(\gamma\lambda\ell)\,Y\right] \tag{6.22}$$

represent singularities of Z_{T}^{-1} and Z_{T} respectively.

6.8.5. DETERMINATION OF $\gamma\ell$ AND Z_{nw} FROM EXPERIMENTAL DATA

As described in Sec. 6.3, the determination of $\gamma\ell$ and Z_{nw} requires a measurement of the admittance in both the conducting and pinched-off regime. Since there are many measurements of the admittance in both regimes, we here describe the procedure to fix Y_{p} and Y_{o}. To approach the open and pinched-off regimes as precisely as possible, the approach is to take the admittances that are furthest removed from the pinched-off and open regime respectively. In practice, before we determine the admittance in the pinched-off regime of T6, Y_{p}, we first select any admittance data point where all gates are open $\widetilde{Y}_{\mathrm{o}}$. We then find Y_{p} as the point in the T6 pinchoff measurement that is furthest removed from $\widetilde{Y}_{\mathrm{o}}$. Subsequently, we determine Y_{o} by finding the admittance furthest removed from Y_{p} in the aggregated data for all tunnel gates. The aggregate data is shown in Fig. 6.7b, with the datasets from the T6 pinchoff measurement highlighted in blue. The obtained points $\widetilde{Y}_{\mathrm{o}}$, Y_{p} and Y_{o} are also identified in the figure. We obtain $\gamma\ell = 0.6 + 0.3\imath$ and $Z_{\mathrm{nw}} = (16.7 + 3.6\imath)\,\mathrm{k\Omega}$.

6.8.6. COMPARISON OF G_{DC} AND G_{RF} FOR ALL PINCHOFF CURVES

Here, we provide a more detailed overview of all admittance data obtained and used for the inset in Fig. 6.2e. Similar to Fig. 6.2e, we plot a comparison between G_{DC} and G_{RF} for all tunnel gates in Fig. 6.7c-h. Additionally, we therein show the real part of the admittance, equivalent by definition to the finite frequency conductance. All traces are taken at $V_{\mathrm{B}} = 10\,\mathrm{mV}$ and every gate that is not being swept is kept at 0 V. This ensures the nanowire can only be depleted close to the swept tunnel gate. The further the tunnel gate is from the source of the nanowire, the more important the correction for finite frequency effects is to obtain the correct G_{RF}. This is expected since a larger portion of the shunting capacitance is available as an alternative path to ground which becomes more dominant the closer the nanowire is to pinch-off.

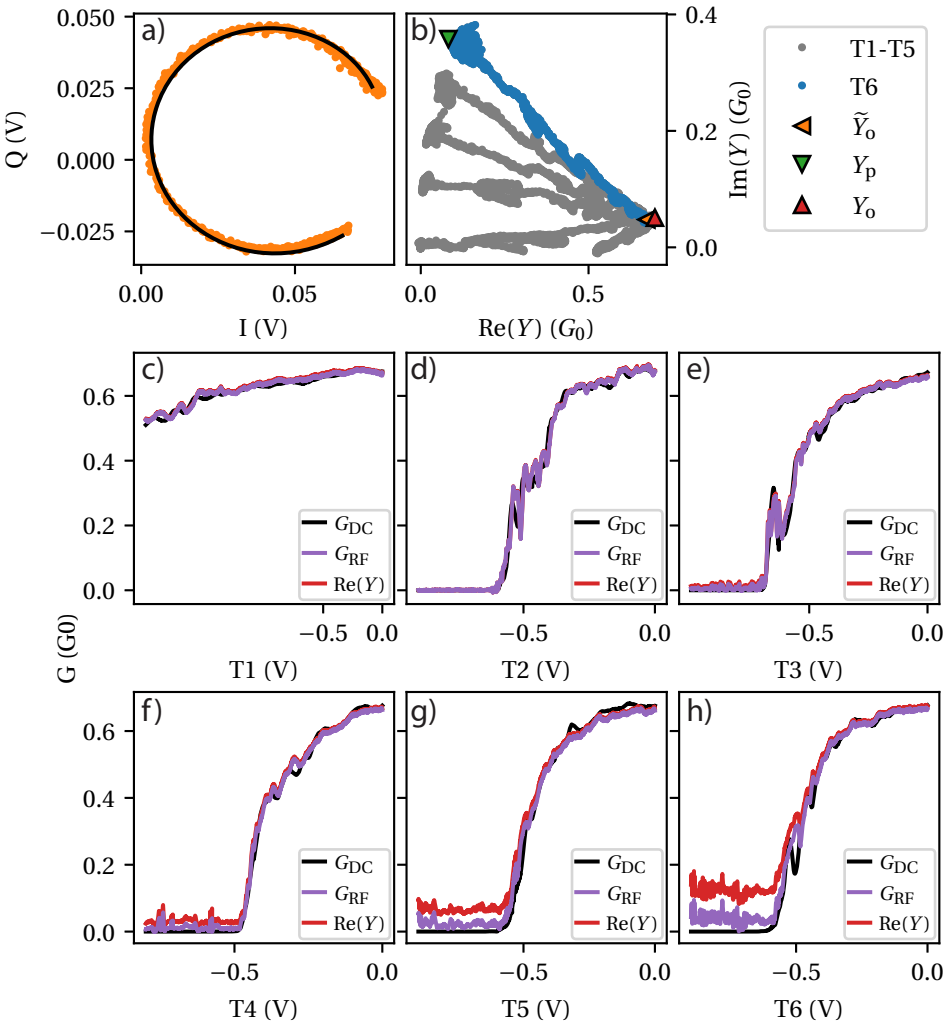


Figure 6.7: **Supplemental data for pinch-off measurements. a)** Resonator response in the IQ plane together with a fit with Eq. (6.6). The phase delay of the line corresponding to $e^{\imath(\theta_0+\theta_1\omega)}$ in Eq. (6.6) is removed from both the data and the fit. **b)** Admittance data for all pinch-off measurements. The data obtained for T6 is highlighted in blue. **c)** to **h)** Conductance measured with DC techniques together with the conductance G_{RF} extracted from the admittance in **b**. To show the importance of correcting for the finite frequency effects in the nanowire, the real part of the admittance is also shown.

6.8.7. SNR MEASUREMENT

The SNR is measured by acquiring a histogram of resonator responses with pulse length t_{int} in both Coulomb blockade and on charge degeneracy. The resulting histograms in the IQ plane are shown in Fig. 6.8. We denote the average response in Coulomb blockade and charge degeneracy by μ_b and μ_r respectively. To calculate the SNR from the histogram, the IQ data is rotated in the complex plane by an angle $\text{Arg}(\mu_r - \mu_b)$. After

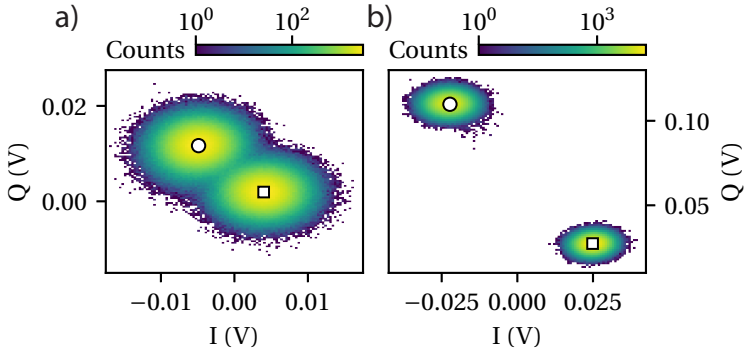


Figure 6.8: **Supplemental data for SNR measurements.** Histograms of the resonator response in the IQ plane with a pulse length of $t_{\text{int}} = 1\,\mu\text{s}$, corresponding to the two regimes in Fig. 6.5. Both histograms contain measurements for Coulomb blockade (square marker) and on charge degeneracy (circle marker). **a)** Histogram for $t_C = 4.5\,\text{GHz}$ and $V_e = 5\,\mu\text{V}$. **b)** Histogram for $t_C = 13\,\text{GHz}$ and $V_e = 0.16\,\text{mV}$.

the rotation, there is no relevant information in the complex part of the data. Therefore we project to data onto the real axis, the result of which is shown in Fig. 6.5c. We fit a Gaussian to the projected data for Coulomb blockade and charge degeneracy separately yielding the standard deviation σ_b and σ_r respectively. Finally, the SNR is given by

$$\text{SNR} = \frac{|\mu_b - \mu_r|}{\sigma_b + \sigma_r}. \tag{6.23}$$

6.8.8. RELATION BETWEEN SNR AND AMPLIFIER NOISE TEMPERATURE

To calculate the relation between SNR and the equivalent noise temperature of the amplifier, we assume that the noise level of the input signal is negligible. The equivalent noise temperature T_N, is defined as [169]

$$T_N = \frac{N_{\text{in}}}{k_B B}, \tag{6.24}$$

where B denotes the measurement bandwidth and N_{in} the equivalent noise input power to the amplifier. Since the integration time, t_{int} is longer than any other timescale in the system, the bandwidth is given by $B = 1/t_{\text{int}}$.

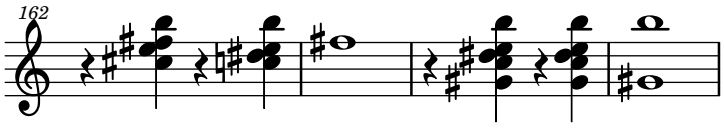
We calculate the voltage fluctuations corresponding to this noise power as $v = \sqrt{N_{\text{in}} Z}$, where Z is the characteristic impedance of the feedline. Using G_{sys} to denote the gain of the amplification in the system, the SNR is defined as the ratio between signal $\Delta = G_{\text{sys}}\Delta_f$ and the noise $2G_{\text{sys}}v$. As such, we find the following equation for the SNR

$$\text{SNR} = \frac{G_{\text{sys}}\Delta_f}{2G_{\text{sys}}v} = \frac{\Delta_f\sqrt{t_{\text{int}}}}{2\sqrt{Z k_B T_N}}, \tag{6.25}$$

assuming the SNR is limited by the noise introduced by the finite noise temperature of the amplifiers in the system.

7

On-demand splitting of single Cooper pairs in hybrid quantum dot systems



Quantum dots have become ubiquitous in quantum processing applications to store quantum information and control the movement of charge. We report on the implementation of a quantum dot device geometry that splits Cooper pairs on demand and detects the emerging electrons. First, we show specific charge transitions can be induced in the system and we identify them using dispersive gate sensing implemented through GHz frequency superconducting resonators. Second, we present results utilizing a double quantum dot as an electron parity sensor without relying on external charge detectors. Finally, we tune up a quadruple quantum dot system and detect parity changes resulting from electrons emerging from the superconducting island. The measurement scheme presented in this chapter reveals a practical way forward to achieve spin correlation measurements on split Cooper pairs.

7.1. INTRODUCTION

The generation of entangled quantum states is an important resource in the study of quantum mechanics and the construction of a quantum computer [173]. In solid-state systems, coherent Cooper pair splitting (CPS) is predicted to generate an entangled spin singlet pair [174]. Besides its application in quantum computation schemes and Bell test experiments [175–178], it also serves as a fundamental probe of spin pairing in the superconducting condensate. The Coulomb repulsion of electrons in a quantum dot (QD) can force a Cooper pair to split, as proposed in Ref. [179]. Indeed, using this method, CPS has been achieved in various material systems [114–116, 170, 180–183].

Splitting Cooper pairs is not sufficient to yield functional entanglement. Firstly, the emerging electrons must be retained in order to perform subsequent experiments. This has recently been achieved by using charge sensing to detect electron tunneling rather than measuring cross-correlations in electron current [184]. Secondly, in order to simplify using CPS as an entanglement resource, allowing the splitting to take place on demand reduces the operational complexity. Combining these two capabilities with cQED techniques allows detailed and rapid investigation of CPS transitions [126, 185, 186].

In this chapter we present single Cooper pair splitting on demand using electrostatic interactions and present a way for the subsequent detection of the emergent electrons. These methods are implemented using an InAs nanowire in which we induce a hybrid quantum dot system; a superconducting quantum dot with normal quantum dots on either side. We show how dispersive gate sensing detects changes in the electron parity in a double quantum dot (DQD) system. Therefore, dispersive gate sensing can replace electrical current measurements, while allowing the emerging electrons to be retained in quantum dots. Specifically, this chapter consists of three main parts. In Sec. 7.3, we show measurements of the central part of this CPS scheme, a floating triple quantum dot (TQD) system. Using multiplexed resonator readout allows distinguishing different charge transitions in the system, and by extension labeling the charge states. One transition in particular corresponds to CPS, where its constituent electrons are loaded into the two outer quantum dots. This transition is studied in detail in Sec. 7.4. Finally, we show how a double quantum dot reveals the presence of a single electron and can detect electrons emerging from the superconducting island in Sec. 7.5. We therefore show all the necessary ingredients for splitting Cooper pairs on demand. These demonstrated capabilities could be used in subsequent experiments to split and detect electrons from a single Cooper pair.

7.2. EXPERIMENTAL SETUP

The devices measured in this chapter consist of an InAs nanowire with epitaxial Al shell, and are shown in Fig 7.1a. Lithographically defined gates define five QDs in the wire. The Al shell of the nanowire is etched from the two dots to the left, and the two dots to the right of the middle island M, such that only the middle QD has a superconducting pairing interaction. Every QD is capacitively coupled to a coplanar waveguide (CPW) resonator with a common feedline for multiplexed gate-based readout of the individual QDs [78, 79, 156, 187]. Additional fabrication details can be found in Chapter 3 and Appendix A.

Fig. 7.1a shows the two devices discussed in this chapter. Device A has a super-

conducting island length of 1.2 µm while the superconducting island length of device B has the same length as the normal QDs, 0.44 µm. The charging energy of the used normal QDs is determined from independent Coulomb diamond measurements as $E_C^N = \frac{e^2}{2C_\Sigma} \approx 250\,\mu\text{eV}$, see Sec. 7.7. From E_C^N and the charge stability diagrams (CSDs) shown in Fig. 7.1c, the charging energy of the superconducting island for device A is extracted as $E_C^S \approx 100\,\mu\text{eV}$ and its lowest-energy odd-parity state at zero magnetic field is given by $E_0 \approx 130\,\mu\text{eV}$. Here, we do not distinguish between the gap edge and subgap states. Similarly, for device B, we obtain $E_C^S \approx 350\,\mu\text{eV}$ and $E_0 \approx 50\,\mu\text{eV}$. The value of E_0 is not intrinsic to the device but signifies the presence of a subgap state in measurement shown in Fig. 7.1c.

Both samples are measured in a dilution refrigerator at a base temperature of approximately 20 mK. The low power signals are amplified by a traveling wave parametric amplifier (TWPA) [89], in addition to a high-electron-mobility transistor (HEMT).

7.3. TRIPLE DOT CHARGE STABILITY DIAGRAM

We start by investigating the floating TQD system by measuring its CSD. By measuring a CSD, we can obtain the relative charge occupation for different regions in gate-space, and thereby infer how the charges in the system interact. The system is brought into this regime by first tuning gate voltages T3 and T4 into the tunneling regime. Subsequently, gate voltages T2 and T5 are set deep into the pinch-off regime to prevent any electrons tunneling across these gates. Operating in the floating regime significantly reduces the complexity of the system. Since electron tunneling to the environment is inhibited, the total number of electrons is conserved, effectively leaving only two charge degrees of freedom. This means that to measure the full CSD, it is sufficient to vary two gate voltages (e.g. V_L and V_R) because all available charge occupations and transitions can be reached without using a third plunger gate.

To measure the CSD, we perform gate-based readout which shows the charge hybridization between the different QDs in the system, thereby signaling the stability of the different charge regions. Measuring the response of resonators L, M and R simultaneously using frequency multiplexing, additionally reveals between which QDs an electron is being exchanged, further aiding the interpretation of the CSD. The multiplexed measurement yields three complex-valued amplitudes, A_i with $i \in \{L, M, R\}$, representing the in phase and quadrature components of the response of each individual resonator. We simplify the resonator response to reveal correlations between the different resonators. This is achieved by projecting the complex data onto a line such that the difference between Coulomb blockade and charge degeneracy is accentuated, see Sec. 7.7. Finally, we normalize the projected data for every resonator and denote the result by the real-valued parameter A_i'. We visualize the three resonator responses using a combined colormap. Starting with the color white in the case of absence of response on all resonators (i.e. Coulomb blockade), we add cyan, magenta and yellow color controlled by the resonator responses, A_L', A_M' and A_R' respectively. For the case of at most two responding resonators, a partial colormap is shown in Fig. 7.1b.

The resulting CSD is shown in Fig. 7.1c for both devices A and B. Indeed, Coulomb blockaded regions can be observed in white separated by charge transitions. At these

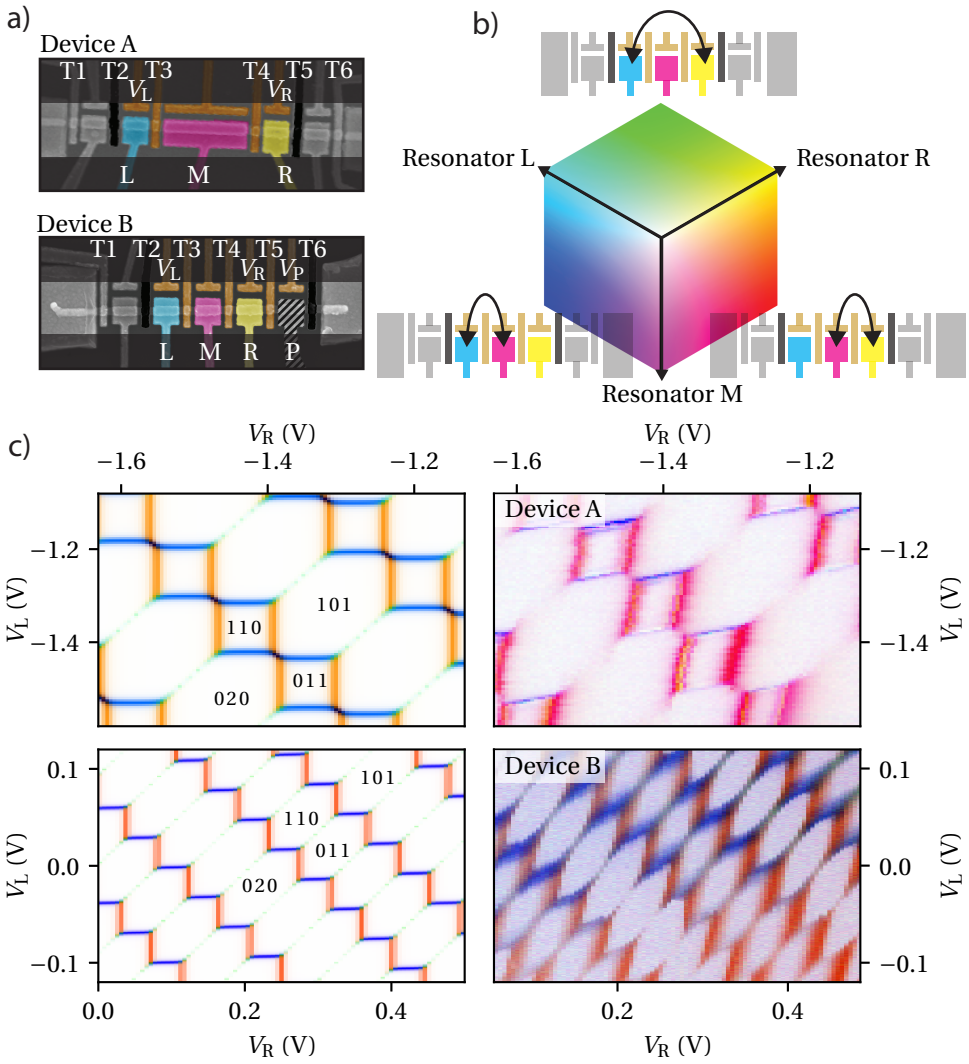


Figure 7.1: **Sample design with corresponding charge stability diagrams in the floating TQD regime. a**) False-colored SEM micrographs of devices similar to those measured in this chapter, labeled device A and device B. Device A is shown in the floating TQD regime, while device B is shown in the floating quadruple dot regime. The resonators are color coded using cyan, magenta and yellow for the (L)eft, (M)iddle and (R)ight resonator respectively. The rightmost resonator (P) of device B is shown in black stripes and is used for the parity sensing in Sec. 7.5. **b**) To concisely show the response of the multi quantum dot system, the response of the three main resonators is mixed using their respective colors, cyan, magenta and yellow. The response of every resonator is normalized individually before combining them as a single color. This results in a 3 dimensional colormap, the outer shell of which is shown here. For every combination of 2 responding resonators, the corresponding tunneling process is schematically depicted. **c**) The experimentally obtained charge stability diagram of the floating TQD system is shown on the right hand side using the colormap shown in **b**). The measurements for the individual resonators are included in Sec. 7.7. On the left, we show the corresponding theoretical simulations, using the energy scales quoted in Sec. 7.2. Several charge states are labeled with the relative number of electrons in the left, middle and right dot. For more details, see Sec. 2.1.6.

charge transitions, electrons are hybridizing between two QDs. Since gate-based sensing reflects charge hybridization, the resonators connected to both these QDs show a response. For the transition between the middle and the left QD, a response is expected in A'_{L} and A'_{M} which shows up as blue in the colormap, shown in Fig. 7.1b. Similarly, the transition between the middle and right QD corresponds to the color red. These two processes are the most prominent in the CSD shown in Fig. 7.1c as changing the gate voltage V_{L} (V_{R}) predominantly exchanges electrons to the left (right) QD, which indeed show up as blue (red). An electron directly tunneling from the left to the right dot, cotunneling over the middle dot [49, 188], represents an essential process for Majorana box qubit readout [25, 26]. These transitions show up in green, but in this configuration, they are much weaker than the first order transitions.

Comparing the CSDs from device A and B, a stark difference can be observed; the latter shows only hexagonal Coulomb blockaded regions while the former alternates between square and octagonal regions. To further understand the difference between the two devices we make a comparison to simulations of the QD system, as shown in the left column of Fig. 7.1c, taking the charging energies, $E_{\mathrm{C}}^{\mathrm{S}}$ and lowest odd-parity state, E_0 obtained from the CSDs. Sec. 2.1.6 describes the simulation procedure and provides the necessary details to calculate the theoretical resonator response using input/output theory [153], see also Sec. 2.2.2. The difference in structure between the two CSDs is controlled by the condition $E_{\mathrm{C}}^{\mathrm{S}} < E_0$ (device A) or $E_{\mathrm{C}}^{\mathrm{S}} > E_0$ (device B). Additionally, the simulated CSDs are labeled with the lowest energy charge states. As expected, the transitions separating two charge regimes show the resonators responding corresponding to the charge being moved. Crucially, in the CSD of device A, a transition between $(0,2,0)$ and $(1,0,1)$ can be observed, corresponding to a Cooper pair splitting in the superconducting island and appearing as separate electrons in both the left and right QD.

7.4. GATE INDUCED COOPER PAIR SPLITTING

As we have seen, Cooper pairs can be split into individual electrons by moving across the appropriate charge transition in a floating TQD. Here we examine this transition —only appearing in the CSD if $E_{\mathrm{C}}^{\mathrm{S}} < E_0$ as is the case for device A— in more detail in Fig. 7.2. To this end, the full frequency response of the middle resonator is measured rather than the fixed frequency response. We fit the resonator response for every gate voltage individually to a hanger input-output model [74, 76, 160]. The obtained resonance frequency, ω_0 and photon decay rate, κ_{d} are shown in Fig. 7.2a and Fig. 7.2b respectively. The resonator responds strongly for the single electron transitions with a frequency shift $\Delta\omega_0 > 2\pi \times 2.5\,\mathrm{MHz}$.

By changing the gate voltages V_{L} and V_{R} simultaneously, we can isolate the CPS transition as shown by the dashed arrow labeled ζ in Fig. 7.2a,b. We note that this is equivalent to changing the gate voltage V_{M} in the opposite direction. Fig. 7.2c shows the frequency response along a linecut over this transition. A significant dispersive shift, $\Delta\omega_0 > 2\pi \times 1\,\mathrm{MHz}$, is observed for the CPS transition. The microscopic origin of the underlying process cannot be determined from the data presented here. One possibility is crossed Andreev reflection, where both electrons directly tunnel into the two normal QDs. This process is suppressed exponentially by the length of the superconducting island, $L = 1.2\,\mu\mathrm{m}$ over the superconducting coherence length in the nanowire, ξ as $\exp(-L/\pi\xi)$.

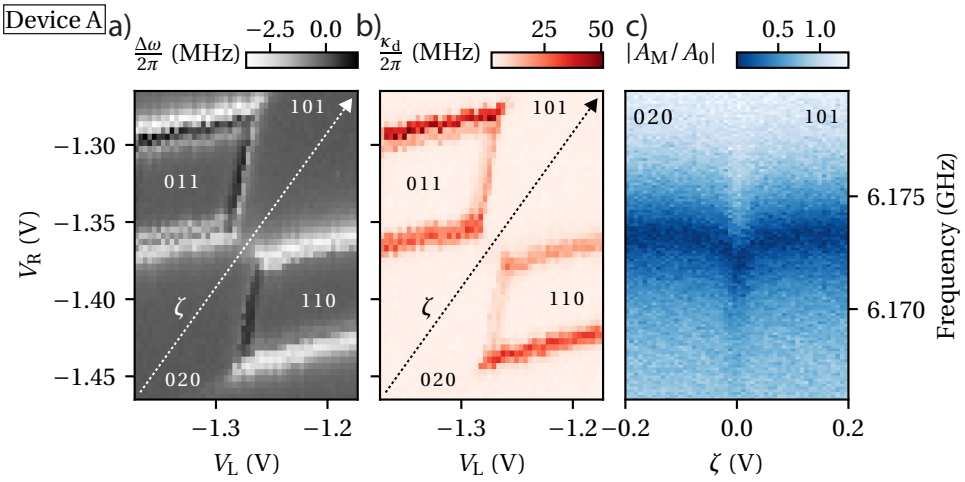


Figure 7.2: **Middle resonator response in the floating triple dot regime. a**), **b**) The resonance frequency, $\Delta\omega$, and linewidth, κ_d of the middle resonator. The values are from the frequency response of the middle resonator for every point in the charge stability diagram. **c**) Frequency response of the middle resonator across the Cooper pair splitting transition. The gate voltage, $\zeta = V_L + V_R - V_{offset}$ is defined in **a**) and **b**) by the dashed arrow.

From the reported coherence lengths in comparable geometries [103, 135, 189], we conclude that for device A, this remains a possible scenario, but alternative processes cannot be excluded. One important alternative is an elastic co-tunneling process in which the lowest odd-parity state in the superconductor (i.e. one of the square charge regimes in Fig. 7.2) is occupied virtually [49, 188]. The contribution of this process is controlled by the detuning of the odd-parity state, which at the CPS transition is proportional to $E_0 - E_C^S$. Importantly, regardless of the underlying mechanism, the measurement shows CPS, splitting a Cooper pair on demand by crossing a single charge transition. To increase the relative contribution of crossed Andreev reflection to the transition, the length of the superconducting island should be reduced while maintaining $E_C^S < E_0$.

7.5. PARITY SENSING IN A QUADRUPLE QUANTUM DOT

Having shown the charge configuration where the Cooper pair splitting transition appears, in this section we focus on how the resulting individual electrons can be observed. In essence, a floating double quantum dot (DQD) is sensitive to the parity of the number of electrons it contains [190]. This is illustrated by the simulation shown in Fig. 7.3a neglecting spin, where we calculate the resonator response as a function of detuning, δ between the two QDs. From this figure, we observe that the position of Coulomb resonance depends on whether there is an even or odd number of electrons in the DQD. When the relative parity inside the DQD changes, the position of charge degeneracy will change into Coulomb blockade and vice versa. Note that a parity dependent result can be observed except on the two crossing points when the width of the Coulomb peaks is on the same order as the gate periodicity. Using dispersive gate sensing is an attractive

method for reading out the configuration of the DQD since it simplifies the needed device geometry compared to using external charge sensors. It has been shown that the difference between Coulomb blockade and degeneracy can be measured rapidly and reliably [91, 92, 95–99, 106, 122, 152, 164–166]. Note that measuring the position of charge degeneracy does not allow measuring the absolute parity inside the DQD, but only relative changes. However, this is sufficient to observe individual electrons splitting off from Cooper pairs, as will be shown in the remainder of this section.

Concretely, we apply parity sensing to the tripledot system shown in Fig. 7.1 where we aim to observe parity changes in the right quantum dot (QD R). To this end, we also tune-up the parity quantum dot (QD P) which together with QD R creates a DQD forming the parity sensor, see bottom panel of Fig. 7.1a. In practice, to reach the appropriate configuration, the gates T3 and T4 are left in the same tunneling regime as before while T5 is tuned to a tunneling regime with large tunnel coupling, such that the two rightmost QDs together form a DQD while also retaining the behavior of a single QD. Finally, T2 and T6 are pinched off completely to prevent the any electrons tunneling to or from the outside leads. This means there are three charge degrees of freedom in the system requiring a three-dimensional CSD to observe every transition. Rather than using V_L, V_R and V_P as independent parameters, we use a different linear combination. Specifically, we use V_L together with the detuning between the rightmost two dots, $\delta = V_\mathrm{R} - V_\mathrm{P}$ and the average of V_R and V_P, denoted by ϵ, see Fig. 7.3c.

The acquisition method and data representation for this measurement is identical to the procedure outlined for Fig. 7.1c in Sec. 7.3. For the quadruple quantum dot system, the resulting CSD is shown in Fig. 7.3b, for two different values of the detuning δ, chosen such that the DQD is on charge degeneracy for even or odd parity. The structure of both CSDs is similar to that of Fig. 7.1c except that some Coulomb blockaded charge plateaus show up as yellow rather than white. The yellow color signifies that an electron is hybridizing between QD R and a QD not represented in the colormap (cf. Fig 7.3e). In this case, the only possibility is QD P. Notice that the charge plateaus for which resonator R responds are opposite between the two detuning values represented in Fig. 7.3b. Also, whenever the right DQD system changes parity, the response changes from white to yellow or vise versa. The extra electron/hole can come from the leftmost QD, by crossing the co-tunneling transition between the circle and square marker in the CSD. Alternatively, the electron can be exchanged with the middle island, crossing a charge transition that shows up in red. In short, the parity dependent response is consistent with the labeling of the charge states in Fig. 7.1c.

Instead of showing the CSD for a constant detuning, Fig. 7.3d shows the response of resonator P as a function of the detuning, δ measured at the circle and square markers in Fig. 7.3b. We fit the resulting Coulomb oscillations with a repeated Lorentzian and observe that Coulomb resonance for the solid line occurs exactly when the dashed line shows Coulomb blockade, consistent with the simulation shown in Fig. 7.3a. Keeping the periodicity of the repeated Lorentzian fixed, we repeat this fitting procedure for all gate voltages shown in the CSD. We denote the detuning offset of the repeating pattern by δ_r, indicating the position of the charge degeneracy in the detuning window between $-14\,\mathrm{mV}$ and $43\,\mathrm{mV}$. In other words, the fitting parameter δ_r signals whether the parity corresponds to the region indicated by the square or circle markers in Fig. 7.3.

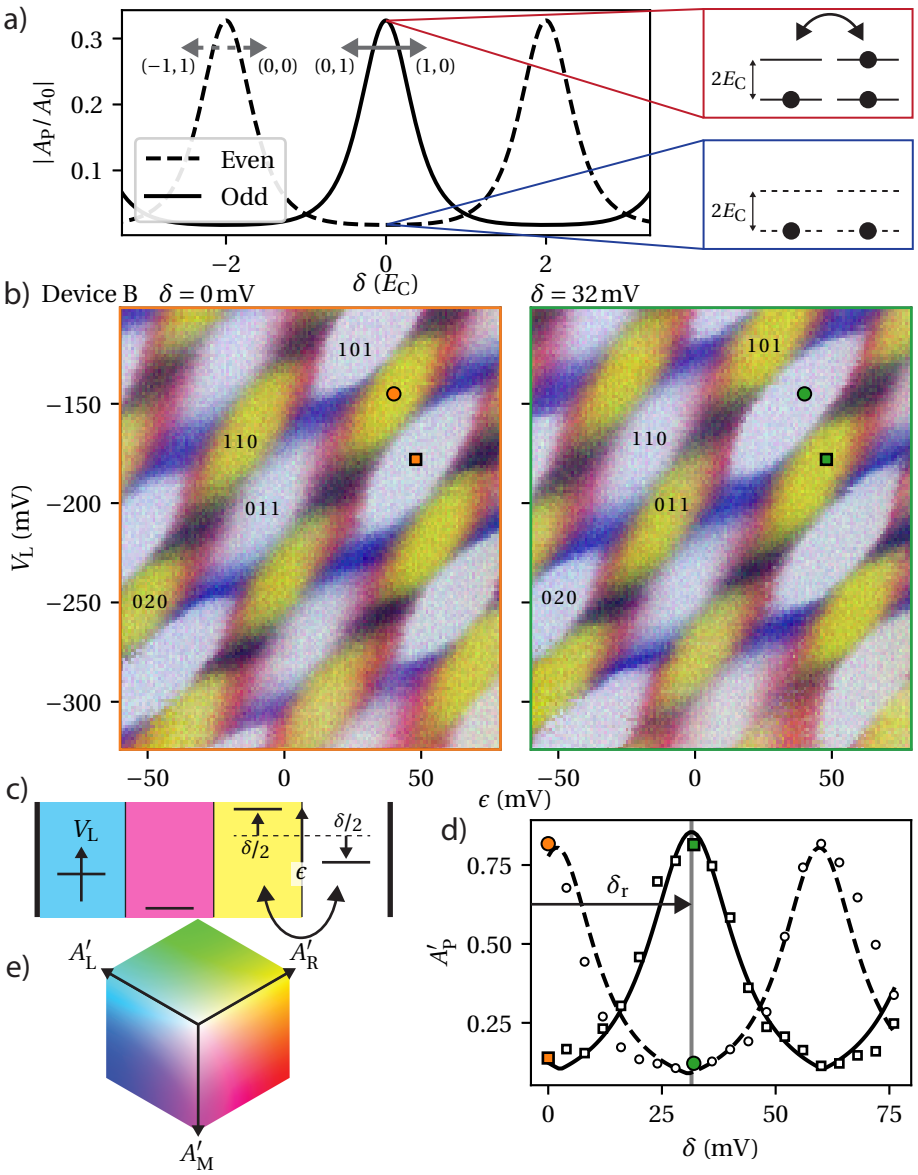


Figure 7.3: **Parity measurement with a DQD. a**) Simulation showing the position dependence on parity of the Coulomb resonance peaks neglecting spin. At zero detuning between the dots, i.e. $\delta = 0\,\mu$eV the resonator P shows a response in the odd regime (solid line), but is blockaded in the even regime (dashed line). The insets show a cartoon of the quantum dot levels at this position in both cases. **b**) Multiplexed charge stability diagram of the floating quadruple dot regime with the colormap shown in **e**). The voltage ϵ represents changing the gate voltages on the right double dot keeping its detuning δ fixed. Several charge plateaus are labeled to represent the occupancy of the dots where the rightmost number represents the combined occupation of QD R and QD P. The left and right diagram show the linecut at $\delta = 0$ mV and $\delta = 32$ mV respectively. The definition of δ and ϵ is schematically shown in **c**). The individual resonator response of these figures is shown in Sec. 7.7. **d**) Linecuts of the normalized resonator P response as a function of the detuning δ, measured at the position indicated by the square and circle marker in **b**). The solid and dashed line show a fit with a repeated Lorentzian peak to the two linecuts. From the solid line, the quantity δ_r is extracted as shown by the arrow.

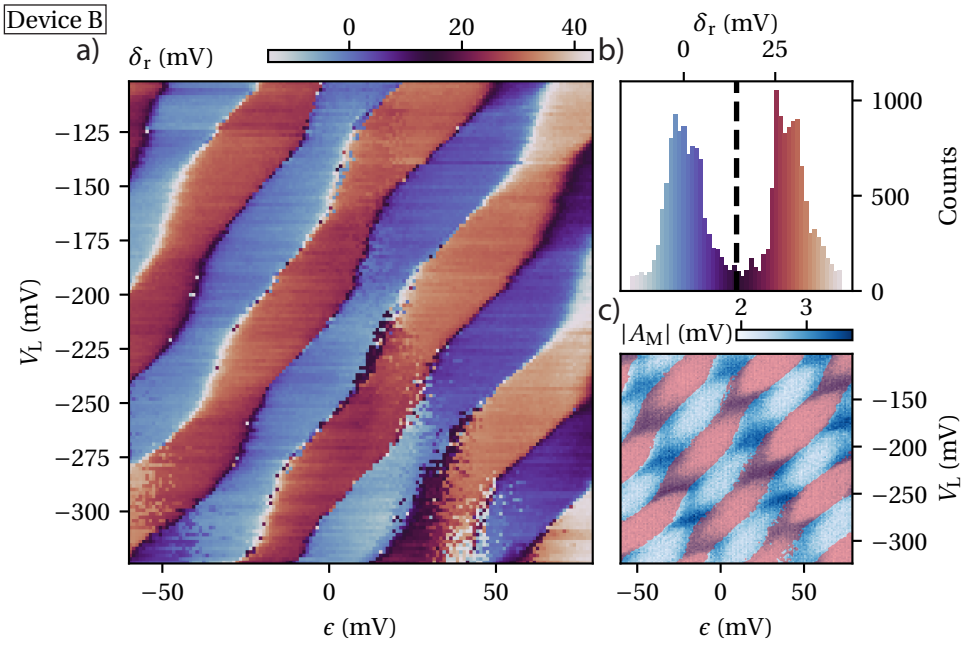


Figure 7.4: **Assignment of parity to the charge stability diagram in the floating quadruple dot regime. a**) The detuning for which the double dot is on resonance, $-14\,\text{mV} < \delta_r < 43\,\text{mV}$. **b**) Histogram of δ_r representing the data shown in **a**). The dashed line is the threshold used for parity assignment. **c**) The normalized response of the middle resonator for the same charge stability measurement shown in **a**). parity is assigned using the histogram shown in **b**) for every point in this charge stability diagram. The red overlay shows the regions where odd parity is assigned.

In Fig. 7.4a, we show the position of charge degeneracy, δ_r as a function of the remaining gate parameters. The figure shows clear regions corresponding to the two different parities in the DQD. Indeed, two separate parity states can be inferred from the histogram of the values of δ_r (Fig. 7.4b). The two different parities are centered around $\delta_r = 0\,\text{mV}$ and $\delta_r = 29\,\text{mV}$ corresponding the dashed and solid line in Fig. 7.3d. Parity can be assigned to each value of δ_r, by defining a threshold in between the two parity states, represented by the dashed line in Fig. 7.4b. Finally, we show the assigned odd-parity regions in Fig. 7.4c on top of the normalized response of the middle resonator. We observe that there is a clear correspondence between the assigned parity, and the CSD of the TQD showing the accuracy of the parity sensor.

7.6. CONCLUSIONS & OUTLOOK

We have realized a normal-superconducting-normal hybrid triple quantum dot system in an InAs nanowire. Multiplexed dispersive gate sensing shows different pairs of resonators responding depending on the nature of the charge transition. This allows inferring the spatial position of the electron through the system and reveals charge states arising in the CSD. We observe a CPS transition, repelling two electrons from the super-

conducting island to the normal dots on both sides. Crossing this transition, splits a single Cooper pair on demand and retains the resulting individual electrons for subsequent investigation. Furthermore we have shown that a double quantum dot is sensitive to its parity and can be used to observe electrons being ejected from the superconducting island when the system is tuned up in the quadruple dot geometry.

From the methods presented in this chapter, the spin correlation between the electrons in a Cooper pair cannot be obtained. In order to achieve this goal, we discuss ways to improve the experiments performed in this chapter. To make crossed Andreev reflection the dominant contribution to the CPS, the superconducting island must be shorter than the superconducting coherence length. At the same time, we require that $E_C^S < E_0$ which requires a sizable superconducting island. Using the methods presented in Ref. [191], small charging energy superconducting islands can be created, extending perpendicular to the nanowire direction. Alternatively, the system can be implemented in 2DEG based material platforms to similarly achieve a non-linear device geometry [192, 193]. Both methods allow satisfying $E_C^S \ll E_0$ while keeping the island much shorter than the superconducting coherence length ensuring the odd-parity states in the superconductor are well separated in energy from the ground state of the system.

After detection of the charge, the next step is to perform spin correlation measurements, which can be achieved using the spin qubit toolkit [194, 195]. Spin-to-charge conversion [196, 197] together with dispersive gate sensing [91, 92, 95, 106, 122, 164, 165] allow inferring the electron spin states [97–99, 152, 166]. This can be achieved by initializing the DQDs on either side of the superconducting island with known spin states in a magnetic field. By measuring the hybridization after forcing a CPS event, the spin state of the emerging electrons can be measured, since the Pauli exclusion principle ensures only oppositely oriented spins can hybridize between the quantum dots. Using electric-dipole spin resonance (EDSR) [101, 198–201], the initialization step can now prepare two independent, known spin states using a microwave excitation applied to both DQD systems. This allows performing a Bell test, using CPS as an entanglement source because the emerging electrons together are predicted to form an EPR pair [175–178].

7.7. SUPPLEMENTAL INFORMATION

In this section we describe the process by which the resonator response is normalized in detail. First, in Fig. 7.5 and Fig. 7.6, we show the raw data for the CSDs shown in Fig. 7.1 and Fig. 7.3 of the main text.

The goal of normalizing the resonator response data is to reduce the dimensionality of the data while accentuating the difference between Coulomb blockade and charge degeneracy. First, the complex-valued response is projected onto a line. Then, the data is normalized such that Coulomb blockade is mapped to 0 while charge degeneracy is mapped to 1. By following the same procedure for the different CSDs shown in this chapter, similar charge transitions show up with the same colors in the different figures.

As an example, we outline the procedure in Fig. 7.7a showing the response of resonator M corresponding to Fig. 7.5b. To project the complex-valued data onto a line, we first estimate the resonator response A_0 in Coulomb blockade as the most occurring response in the CSD. Secondly, we find the average response, A_1 to estimate the vector along which the resonator responds on average. Both points are marked in Fig. 7.7a and

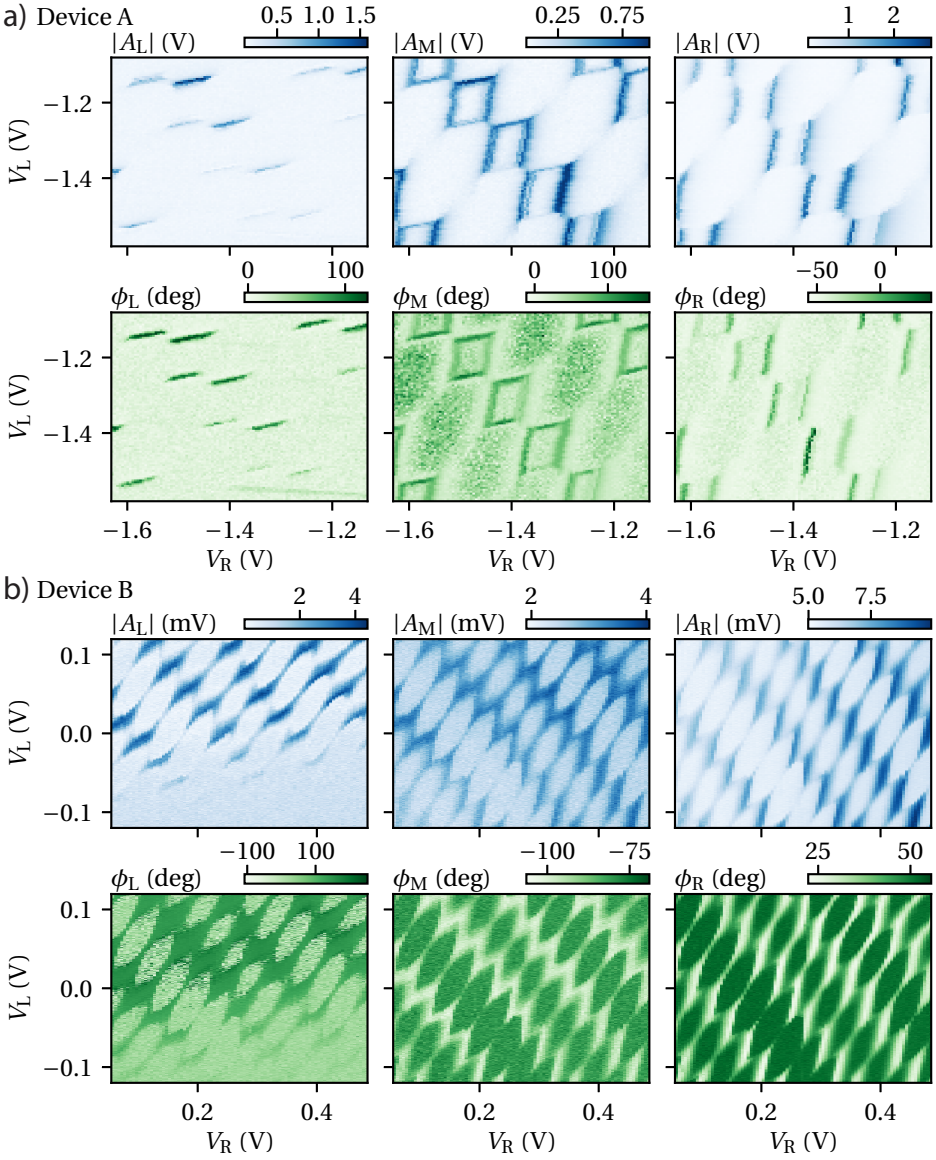


Figure 7.5: The individual resonator responses corresponding the two CSDs shown in Fig. 7.1c. Here, $|A_i|$ and $\phi_i = \arg(A_i)$ denote the amplitude and phase response of resonator i. **a**) Shows the response of device A while **b**) shows the response of device B.

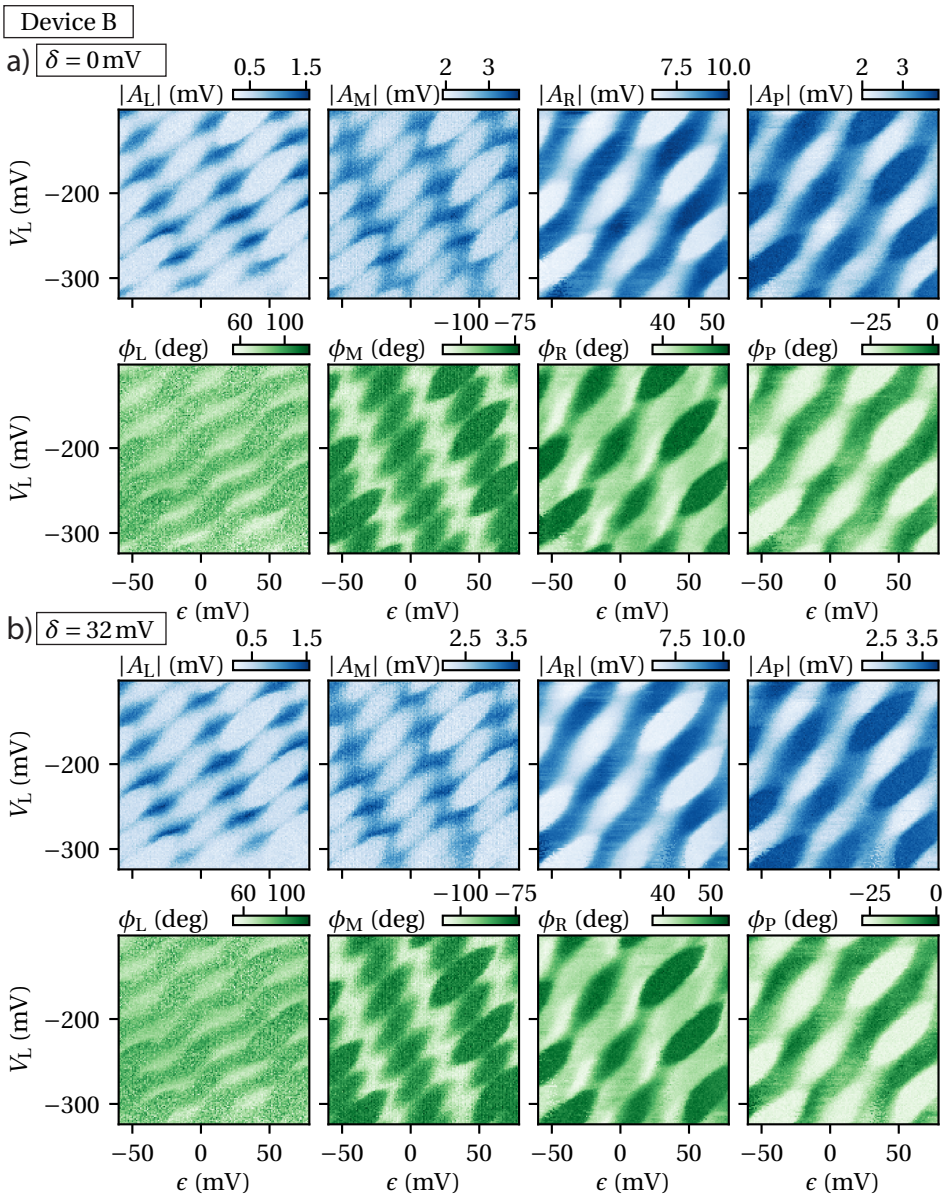


Figure 7.6: The individual resonator responses corresponding the CSDs shown in Fig. 7.3b. Here, $|A_i|$ and $\phi_i = \arg(A_i)$ denote the amplitude and phase response of resonator i. Even though the response of resonator P is not included in the colormap (see Fig. 7.3e), it is added here for completeness. **a**) A slice from the CSD taken at a detuning of $\delta = 0$ mV. **b**) A different slice from the same CSD taken at a detuning of $\delta = 32$ mV.

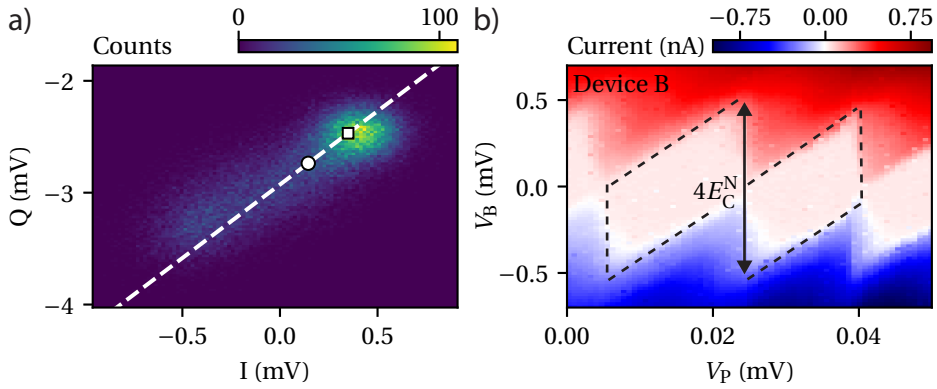


Figure 7.7: **a**) Histogram of the IQ response of the middle resonator, corresponding to the middle panel in Fig. 7.5b. The square marker denotes the most occurring IQ response which we associate with Coulomb blockade while the circle marker denotes the average IQ response. These markers define the dashed line which is used to project the complex-valued data. **b**) Current measurement of Coulomb diamonds for QD P in device B. From the bias axis, we infer $E_C^N = 250\mu eV$.

show that the resonator response indeed falls along the vector $A_1 - A_0$. The data is subsequently projected onto the line defined by A_0 and A_1 and normalized to range from 0 to 1. This procedure is repeated for every resonator individually before they are combined into the same colormap.

Finally, in Fig. 7.7b, we show a Coulomb diamond measurement from which the charging energy of QD P is inferred. Assuming the other normal QDs have the same charging energy, this allows us to convert the voltage axes in Fig. 7.5 to energy, and thereby obtain values for E_C^S and E_0.

8

CONCLUSION & OUTLOOK

We can only see a short distance ahead, but we can see plenty there that needs to be done.

Alan M. Turing [202]

The motivation of the experiments described in this thesis is the realization of a Majorana box qubit. So far, we have put little emphasis on the connection between these experimental results and the box qubit. Therefore, after summarizing the individual chapters, we place the main results of this thesis in the context of the Majorana box qubit and propose follow-up experiments to advance towards a topological qubit.

8.1. CONCLUSION

The goal of this research project is to explore and implement gate-based readout in nanowire quantum dot systems. This particular goal means that the research presented in this thesis is relevant for a multitude of solid-state qubit implementations. Therefore we reiterate and summarize the main results in this section.

In Chapter 4 we have examined dispersive gate sensing in an InAs nanowire double quantum dot. The electron hybridization between the two dots is sufficiently strong to result in a dispersive shift comparable to the resonator linewidth, using low-Q, lumped-element, off-chip resonators. These large resonator shifts are a direct consequence of the large lever arm which we achieved by a wrapped top gate design with a thin ALD dielectric. Indeed, for low measurement power, the size of the dispersive shift directly translates to the magnitude of the tunnel coupling between the quantum dots, see Eq. (2.12). Besides changing the tunnel coupling, we study the effect of readout power and find that the dispersive shift is reduced at high readout power, consistent with driving the double quantum dot to the excited state. Nonetheless, by optimizing power and tunnel coupling, we have obtained a sizable signal-to-noise ratio (SNR) within an integration time of 1 µs. The high SNR confirms gate-based sensing as a versatile readout technology with relevance for a multitude of different mesoscopic quantum devices.

Subsequently, in Chapter 5 we have applied dispersive gate sensing to hybrid quantum dot systems to study the electron hybridization when combined with superconductivity. The superconducting pairing of electrons results in charge transitions involving multiple electrons simultaneously. The exact nature of these transitions is governed by the relative magnitude of the charging energy, superconducting gap, and tunnel coupling. Next, we have shown the ability to distinguish different tunnel coupling strengths arising due to spin effects blocking some of the available electron transitions. Lastly, we have used gate tunable tunnel barriers to inhibit electron tunneling to external electrodes and reach the floating regime. In this regime, we have performed spectroscopy of a superconducting subgap state using solely gate-based sensing without relying on transport data.

In Chapter 6 we have pushed the limits of gate-based sensing. The results of Chapter 4 imply that an increase in SNR is possible using high-Q resonators and quantum-limited amplification. To allow for flexibility in resonator design, we have used on-chip resonators where the resonator-to-feedline coupling is tuned to match the expected dispersive shift. Switching to the gigahertz frequency regime allows the use of a traveling wave parameter amplifier (TWPA). Furthermore, the higher resonator frequency decreases the detuning between the resonator and the double quantum dot transition energies. These factors together culminate in a vast increase in achieved SNR exceeding 15 for a pulsed 1 µs measurement. Next, we have shown the capability for connecting multiple resonators to the same quantum dot system, allowing multiplexed readout of multiple resonators simultaneously. In contrast to transport measurements, dispersive gate sensing measures local electron tunneling which means multiplexed resonator readout allows the spatial correlation of electron tunneling in the nanowire. Besides gate-based sensing, we have presented a quantitative understanding of resonators coupled to the ohmic contacts on the nanowire. With this quantitative understanding, we have extracted the DC conductance through the nanowire without any DC calibration measurements.

Finally, Chapter 7 extends on the research performed in Chapter 5 while applying the resonators described in Chapter 6. The different charge states in the hybrid quantum dot system are identified by correlating the multiplexed resonator responses. We have found a transition that splits individual Cooper pairs into their constituent electrons, pushing them to either side of the superconducting island. Furthermore, we have shown the capability to detect electron parity using a double quantum dot which allows for low infrastructure parity detection. We have presented this capability in a floating quadruple dot system. In this geometry, we have detected the parity switches induced by changing the gate configuration to push an electron into the parity detector.

8.2. READOUT FOR THE MAJORANA BOX QUBIT

In this section, we discuss the relation between the readout of double quantum dots to the Majorana box qubit. As described in Sec. 1.4, the electron hybridization of the connected quantum dots reflects the state of the qubit. Specifically, in the geometry described in Ref. [25], the complex phase of electron tunneling through the superconducting island, $\mathrm{Arg}(t_\gamma)$, is determined by the qubit state, corresponding to the operator σ_z. Interference between this tunneling path and the direct tunneling amplitude, t_0, causes

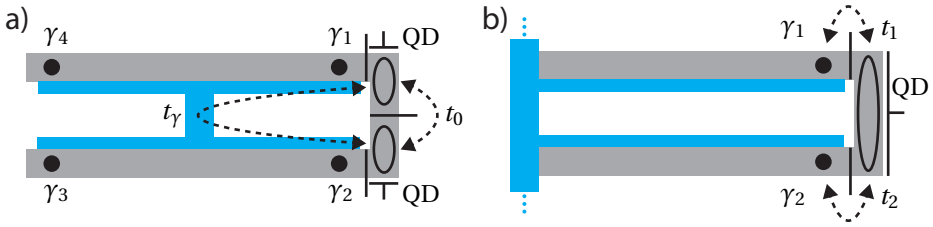


Figure 8.1: **Two schematics of Majorana box qubit proposals. a**) The simplest geometry proposed in Ref. [25]. **b**) A substructure of the geometry proposed in Ref. [26]. The blue regions represent the superconductor, while gray represents the semiconducting geometry. Here, it is assumed that the superconductor induces topological superconductivity in the semiconducting parts resulting in Majorana zero modes at the ends of the topological regions (shown as black dots). The outlined ovals denote the position of quantum dots facilitating the readout of the system, with the relevant tunnel couplings shown by dashed arrows. Figure adapted from Refs. [25] and [26].

this phase difference to modulate the effective tunnel coupling between the two quantum dots, $t_C = t_0 + \sigma_z t_\gamma$, see Fig. 8.1a. Similarly, in the geometry proposed in Ref. [26], the tunnel coupling between the semiconductor quantum dot and the superconducting island is determined by the interference between tunneling into the Majorana zero modes γ_1 and γ_2, see Fig. 8.1b. Although the former geometry uses a double quantum dot as opposed to a single semiconductor quantum dot for the latter geometry, in both cases, measuring the tunnel coupling allows assigning a state to the qubit.

In Chapters 4 and 6, we have shown the ability to detect electron tunneling using dispersive gate sensing. In these chapters, changing from Coulomb blockade to resonance in a double quantum dot gives two different electron tunneling states. These two states serve as a proxy for the states of a qubit system. We show the ability to distinguish these two regimes on microsecond timescales with a high SNR. For a future Majorana box qubit, the relevant quantity is the difference between two finite tunnel couplings rather than the existence of electron tunneling. Fig. 4.3a shows the influence of tunnel coupling on the resonance frequency and thereby the available readout signal. It is important to notice that the two exact values of tunnel coupling to be differentiated will dramatically influence the qubit readout fidelity. So far, there is no firm prediction of the coupling strength between Majorana zero modes and their neighboring quantum dots. Especially for small coupling strengths ($t_\gamma \ll \omega_0$), the geometry shown in Fig. 8.1a has the advantage that tuning the tunnel coupling t_0 transposes the combined tunnel coupling t_C to the most sensitive regime. Since the geometry shown in Fig. 8.1b utilizes only a single quantum dot, the total tunnel coupling cannot be transposed with the same freedom. In either case, the tunnel coupling difference for distinguishing the different qubit states, results in a frequency change that cannot exceed that of the double dot proxy states, since the latter represents the optimal case of distinguishing finite from infinite tunneling rates. The resulting reduction of the SNR notwithstanding, the double dot experiments show the feasibility of dispersive gate sensing for Majorana box qubit readout.

Dispersive gate sensing is not the only method proposed for the readout of Majorana box qubits [25]. One alternative works by operating the two quantum dots as a

charge qubit. The Rabi oscillation frequency of this charge qubit depends on the Majorana box qubit state. Letting the charge qubit oscillate for a fixed amount of time and subsequently measuring the charge residing on either of the quantum dots allows obtaining the Rabi frequency and thereby the Majorana box qubit state. This method requires fabricating additional charge sensors close to the core geometry of the sample, where space will probably be limited. Furthermore, the readout protocol is more complicated than the protocol for dispersive gate sensing, making this method less desirable for the initial experimental verification of this qubit design. Another possibility to obtain the interference between the two paths through the box qubit is to replace the quantum dots with DC contacts and measure the conductance. Measuring the conductance with DC techniques will likely not be fast enough for qubit operation, but RF techniques allow speeding this readout up considerably, see also Sec. 6.3. Either way, this method necessitates connecting the system to external electrodes, introducing the possibility of poisoning the Majorana zero modes with electrons originating in these leads. Therefore, dispersive gate sensing is the most promising method for Majorana box qubit readout.

Finite bias spectroscopy is still a vital measurement technique to aid the investigation of the induced Majorana zero modes and bringing the qubit into the topological regime [203–208]. These measurements are impractical to perform in a floating system, as there is no electron reservoir at a fixed chemical potential. Including ohmic contacts will therefore be beneficial since they naturally serve as electron reservoirs. Nonetheless, after the initial tune-up, gate-induced tunnel barriers should completely pinch off the external contacts to prevent external quasiparticles from reaching the qubit and destroying the quantum state. From the experiments discussed in Chapters 5, 6 and 7 we infer that the number of electrons in a floating quantum dot system can be stable on the timescale of hours. The amount of errors caused by electrons tunneling through the tunnel barriers is likely to be negligible compared to quasiparticles exchanging between the superconducting continuum and the Majorana zero modes. The latter process is estimated to reduce the coherence time of the qubit to below one minute, [209, 210]. Therefore, the additional error correction needed to compensate for external quasiparticles changing the parity of the system is insignificant compared to other noise sources.

Finally, during readout, the quantum dots must have significant coupling to the superconducting island. This coupling also creates the possibility of exchanging a quasiparticle between the superconducting island and the quantum dot. Crucially, this exchange flips the parity of the superconducting island during the readout operation, which constitutes a quasiparticle poisoning event. The double quantum dot geometry can be used to detect parity errors of this type by keeping track of the electron parity on the double dot, which we demonstrate in Sec. 7.5. Conveniently, this method does not require any additional infrastructure, apart from the readout mechanism itself. With the additional tuning flexibility provided by the double quantum dot, we see significant advantages to adding a single extra tunnel gate when realizing the Majorana box qubit.

8.3. QUBIT IMPLEMENTATION

Every device described in this thesis contains only a single nanowire restricting it to a linear device geometry. Crucially, however, a non-linear geometry is essential to fabricate a Majorana box qubit, see Fig. 8.1. There are several ways to implement the necessary

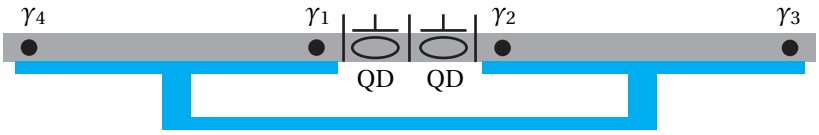


Figure 8.2: **Alternative geometry for the Majorana box qubit.** The advantage of this geometry is that it only needs a single, linear nanowire to realize. Figure adapted from Ref. [26]

qubit geometry, which we discuss in this section.

The first option is to keep the hybrid quantum dot system in a single nanowire. A superconducting structure connecting the two topological sections in the wire then creates the necessary loop in the device [26], see Fig. 8.2. Since this method requires no custom nanowire geometries, flexibility remains to choose the underlying semiconducting material based on compatibility with Majorana zero modes. In principle, the same nanowires used for previous Majorana zero mode experiments are suitable for implementing this geometry.

Fabricating a superconducting loop that induces a hard gap in the semiconductor nanowire without introducing additional local modes on the semi/superconductor interface is non-trivial. The superconducting nanowire sections described in this thesis are evaporated in-situ after the nanowire growth process [80]. Achieving in-situ epitaxial superconductor deposition for the geometry shown in Fig. 8.2 necessitates growing non-linear nanowire networks as described in Ref. [211]. Alternatively, the superconductor can be deposited as a separate fabrication step, as is shown by Ref. [191] on InSb nanowires. However, the usage of InSb as the semiconductor material introduces new challenges since it prohibits processing above room temperature. This temperature bound is especially problematic for the fabrication of the top gates, which ensure the large lever arm between the resonators and the quantum dots, as described in chapters 4 and 6. Specifically, both ALD-based dielectrics and the patterning of top gates at low temperatures are challenging fabrication problems. Using side gates or bottom gates circumvents both problems since the lower lever arm can partially be compensated by increasing readout power and integration time for the gate-based sensing[1].

Although the method outlined above stays very close to known fabrication procedures, it has problems scaling to multiple qubit systems. To apply a quantum computer to interesting problems requires over 100 logical qubits, implying many more physical qubits [212]. Given the large number of qubits needed, depositing individual nanowires for every single qubit is infeasible to achieve a full quantum processor. Therefore, we briefly elucidate two more scalable methods for implementing topological qubits.

The first scalable technique is selective area growth (SAG). With SAG, the nanowire network is grown directly on the substrate, ready for subsequent fabrication steps obviating the manual deposition of the network. The desired nanowire structure is patterned on the wafer using standard lithography techniques before the growth step, allowing flexible network designs [213]. Even though this technique is intrinsically scal-

[1] For bottom gates, lever arms of 0.6 can be achieved as opposed to 0.8 for top gates resulting in a reduction of the signal by approximately a factor of 2.

able, it requires solving extra fabrication challenges. Firstly, the nanowire growth conditions determine the substrate material, which is incompatible with current fabrication recipes for high-Q resonators. Secondly, material quality is paramount for creating stable quantum dots and inducing Majorana zero modes in the system. Finally, SAG is currently incompatible with bottom gates since the nanowire network is grown directly onto the substrate. Using InSb again requires low-temperature fabrication techniques, which hinders the fabrication of top gates. Hence the creation of quantum dots with high lever arm in SAG remains an open problem.

Material platforms based on 2-dimensional electron gasses (2DEGs) provide a second option to improve scalability [192, 193, 214–216]. In this case, electrostatic gates accumulating and depleting the 2DEG define the semiconductor geometry. In terms of material quality, 2DEGs provide the highest electron mobility of the material platforms discussed in this section. However, similar to the SAG case, the 2DEG wafer stack defines the substrate material, hindering the resonator quality factors. Also, the formation of conducting channels is more challenging than the previously discussed materials, where the nanowire shape provides 1D confinement.

Off-chip resonators can circumvent the issue of resonator fabrication for the SAG and 2DEG case. In practice, however, the linewidth of many resonances produced by off-chip resonators, as used in Chapter 4 and 5, is much larger than the optimal value. This limits the resulting SNR as the linewidth —or equivalently, the coupling factor of the resonator to the measurement circuit, κ_{ext}— is an essential factor for magnitude of the readout signal, see Sec. 3.1.1. Furthermore, the resonance frequency of these resonators is in the UHF regime, for which parametric amplification is less flexible than for the SHF regime where TWPAs allow for large bandwidth, low noise amplification. Therefore, developing high-frequency, high-Q off-chip resonators [44, 217] would help provide a readout method independent of the material platform.

Summarizing the different considerations mentioned in this section, for any Majorana box qubit to succeed, it must be possible to induce Majorana zero modes with high reliability and confidence. Therefore, this requirement will likely fully determine the implementation details, while readout and scalability are only of secondary importance. Indeed, the high sensitivity of gate-based readout shown in this thesis leaves space for lowering the SNR necessitated by a potential change of material platform. In terms of scalability, the solid theoretical basis of the Majorana box qubit notwithstanding, providing a firm experimental verification must take precedence as the successful realization of this experiment outweighs any future switching costs to a different material platform.

8.4. OUTLOOK

Between the results presented in this thesis and realizing a Majorana box qubit, there are intermediate experiments to guide towards this goal. Given the complexity of a complete qubit experiment, experiments in the near future should parallelize the different remaining challenges as much as possible. The results of this thesis indicate that dispersive gate sensing is a valuable tool for solving these challenges. Furthermore, we describe a few open questions that emerged from the experimental work in this thesis.

First, an open research question arose while investigating the devices presented in Chapter 7. In the floating double dot regime, with one of the dots superconducting, we

investigate the dispersive shift imparted on the resonator. The charge stability diagram in this regime looks similar to Fig. 5.4b. In contrast to Chapter 5 however, the detuning dependence of the dispersive shift alternates for every subsequent electron tunneling between the dots, as shown in Fig. 8.3a. Strikingly, for device A, each charge transition only causes a single avoided crossing which implies the existence of a state that only decreases in energy when crossing the charge transition. This phenomenon is in stark contrast with the schematic shown in Fig. 2.5 where all transitions are symmetric with respect to the charge degeneracy point. The example shown for device B is less pronounced, but still displays detuning asymmetry with respect to the charge degeneracy, changing direction for the subsequent charge transitions.

To explain the asymmetry in detuning, we hypothesize that there exists a subgap state at an energy of E_0, well separated from the superconducting gap edge at Δ. This hypothesis goes beyond the other models mentioned in this thesis, where only the lowest energy state in the superconductor is taken into account. Specifically, when the number of electrons on the superconductor is even, two different energy transitions are possible to the odd state. In contrast, when the system's ground state is odd, only a single transition to the even occupation exists, as the transition between the subgap state and gap edge does not change the number if electrons in the superconducting island. The available transition energies from the ground state are shown in Fig. 8.3c for both device A and device B by using the methods described in Sec. 2.1.6. Indeed, adding a subgap state to the model causes an asymmetry in the energy transitions, and we see only a single transition crossing the resonator frequency (represented by the black line) for device A. As described in Sec. 2.2.3, roughly speaking, the coupling of the resonator to the charge transition, g_{eff}, depends on the off-diagonal components of the charge number operator, $\hat{N}$. In Fig. 8.3c the different transitions, indexed by k, are colored to represent $|\langle\psi_k|\hat{N}|\psi_0\rangle| \propto |g_{\text{eff}}|$, to indicate where there is significant coupling between the quantum dot system and the resonator. As shown in Fig. 8.3b, we use Input/Output theory described in Sec. 2.2.2 and Ref. [153] to calculate the full resonator response using the transitions shown in Fig. 8.3c. We note that the theoretical simulation shows good agreement with the experimental data giving credence to the stated hypothesis.

The hypothesis of the existence of a subgap state is not in itself unreasonable, e.g. see Chapter. 5, but no supporting data exists for the measurements shown in Fig. 8.3. In principle, the existence of a subgap state can be confirmed by measuring Coulomb diamonds and looking for negative differential conductance [120]. A convenient method to obtain an experimental verification for the value E_0 and Δ is to measure the even-odd spacing at different temperatures, see Fig. 5.4d. Finally, performing two-tone spectroscopy provides an independent measure for t_C [218, 219], which then fixes all parameters needed for the calculation shown in Fig. 8.3. Two-tone spectroscopy also opens the door for many qubit-related experiments where the occupation of the subgap state gives the different qubit states [127, 220].

Secondly, the measurements presented in Chapter 7 in themselves present many experiments worthwhile performing. Primarily, repeating the experiments together with spin readout capabilities allows measuring the spin correlations of electrons forming a Cooper pair. As mentioned in Sec. 7.6, some challenges remain to be solved to successfully perform this experiment, which will not be repeated here. The ability to exe-

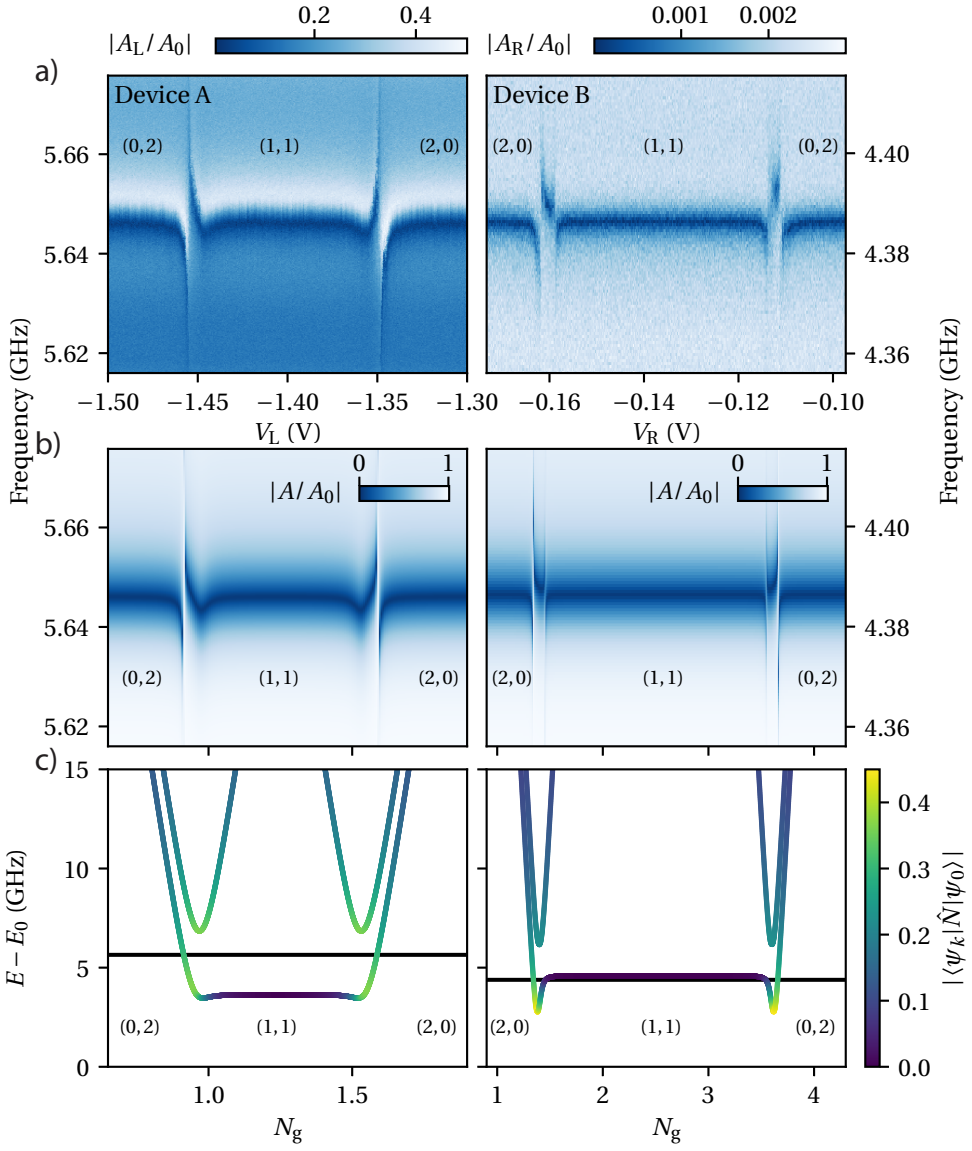


Figure 8.3: **Influence of a subgap state on the resonator response.** **a**) Frequency response of the resonator connected to the normal dot across two charge transitions of a double quantum dot in the floating regime. The left/right panel are taken from experimental data obtained with device A/device B, introduced in Fig. 7.1. **b**) Theoretical simulation showing the effect of a subgap state on the resonator response. The left panel is simulated with the parameters, $E_C^N = 250\,\mu\text{eV}$, $E_C^S = 100\,\mu\text{eV}$, $E_0 = 130\,\mu\text{eV}$, $\Delta = 145\,\mu\text{eV}$ and $t_C = 2.06\,\text{GHz}$. The right panel is simulated with the parameters, $E_C^N = 250\,\mu\text{eV}$, $E_C^S = 350\,\mu\text{eV}$, $E_0 = 50\,\mu\text{eV}$, $\Delta = 69\,\mu\text{eV}$ and $t_C = 1.45\,\text{GHz}$. **c**) The lowest two energy transitions in the system from the ground state. Parameters are identical to panel **b**). The black line denotes the resonator frequency. All points are colored according to $|\langle\psi_k|\hat{N}|\psi_0\rangle| \propto |g_{\text{eff}}|$. As such, the darker points are expected to have minimal dipole moment coupling to the resonator.

cute the spinful Cooper pair splitting experiment opens up the possibility of performing novel follow-up experiments, aiding the research on Majorana zero modes. Specifically, p-wave superconductivity in the superconducting island is a prerequisite for Majorana zero modes. Splitting Cooper pairs in this configuration allows studying this regime and verifying p-wave superconductivity. One advantage of this experiment is that it probes the entire superconducting system rather than only its endpoints where Majorana zero modes are predicted to appear. Therefore, Cooper pair splitting in Majorana compatible geometries is a goal worthwhile to pursue.

Finally, as discussed in the previous section, the ability to induce Majorana zero modes and verify the creation of a topological regime is of paramount importance. For an experiment to achieve this goal, its results must be specific enough to exclude trivial explanations of the obtained data while at the same time it should be simple enough that failure to observe the predicted topological results implies the absence of Majorana zero modes. Even though both criteria are inherently subjective and subject to change based on future theoretical insights, they guide away from local spectroscopy experiments where the plethora of explanations for zero-bias peaks lead to inconclusive results [221, 222]. On the other hand, Majorana qubit experiments are currently not simple enough, given that a lack of topological signal in such experiments is not directly linked to the existence of Majorana zero modes.

One experimental proposal that falls between these two extremes is the measurement of nonlocal conductance [207, 208]. Here, the device consists of a nanowire with a grounded superconducting shell with leads on either end. Crucially, rather than only measuring the local change in current caused by a change in voltage, the current change in the opposite end of the nanowire is measured. Although these measurements do not rely on high-frequency measurement techniques, the rapid measurements enabled by RF techniques allow exploring a much larger parameter space by excluding regimes without states at zero bias. The existence of zero-bias states can either be determined by RF conductance measurements (see Sec. 6.3) or by using dispersive gate sensing by adding quantum dots to either side of the superconducting region (see Chapters 5 and 7). The latter approach has the advantage that a similar geometry with floating superconducting section allows measuring the co-tunneling rate through the Majorana zero modes, a crucial prerequisite for the Majorana box qubit experiment. After identifying potential topological gate regimes, the nonlocal conductance can either be measured using standard lock-in techniques or by using resonators connected to the source and drain electrodes. The RF excitation must be applied from the opposite of the resonator via a weakly capacitively coupled RF contact to obtain the nonlocal components using RF techniques. The superconducting ground on this middle section must be floating in terms of RF and only grounded in DC to prevent signal leaking away to ground.

A

FABRICATION DETAILS

Here, we list the fabrication recipes used for fabricating the samples mentioned in this thesis. The different samples differ slightly in fabricational details, we therefore only write the explicit recipe for Device B in Chapter 7. This recipe was optimized for the Kavli nanolab cleanroom in Delft and many parameters fluctuate over time. Hence, this Appendix is meant as a starting point when developing similar recipes.

1. Sputter a 20 nm global layer of NbTiN
2. Define marker patterns
   - Spin coat with PMMA 495A4 at 4000 rpm
   - Soft bake at 185 °C for 5 min
   - Spin coat with PMMA 950A3 at 4000 rpm
   - Soft bake at 185 °C for 10 min
   - EBL exposure with 2000 $\mu C\,cm^{-2}$
   - Develop with MIBK:IPA 1:3 for 60 s, IPA for 30 s N_2 blow dry
   - Descum with O_2, 200 ml/min and power 600 W for 10 min
   - Evaporate 7 nm Ti
   - Evaporate 83 nm Au
   - Liftoff in 50 °C acetone for 1 h
   - Rinse in IPA for 30 s and N_2 blow dry
3. First dicing step, to pattern individual resonators
   - Spin coat with AZ9260 at 2500 rpm
   - Soft bake at 110 °C for 2 min
   - Dice into chips that can be processed individually
   - Strip resist in 50 °C ultrasound acetone bath for 15 min
   - Rinse in IPA for 30 s and N_2 blow dry

A

4. Etch resonators
    - Spin coat with positive tone CSAR 6200.09 at 4000 rpm
    - Soft bake at 185 °C for 10 min
    - EBL exposure with 300 $\mu C\,cm^{-2}$
    - Develop with Pentylacetate for 60 s, MIBK:IPA 1:3 for 60 s
    - Clean with IPA for 30 s and N_2 blow dry
    - Etch NbTiN in a SF_6/O_2 atmosphere
    - Strip resist with PRS-3000 at 80 °C for 2 h
    - Rinse in H_2O for 15 s, H_2O for 15 s
    - Rinse in IPA for 30 s and N_2 blow dry
    - Descum with O_2, 200 ml/min and power 100 W for 12 min
5. Dice to size of the PCB cavity, see step 3
6. Nanowire deposition
    - Clean using 10 min, 50 °C ultrasound acetone bath
    - Transfer nanowires with micromanipulator [82, 87]
    - Use optical imaging to design the remaining sample features
7. Etch superconducting shell
    - Apply HMDS to pre-heated sample (150 °C for 10 min)
    - Spin coat with PMMA 950A6 at 4000 rpm
    - Soft bake at 185 °C for 5 min
    - EBL exposure with 2000 $\mu C\,cm^{-2}$
    - Develop with MIBK:IPA 1:3 for 60 s, IPA for 30 s N_2 blow dry
    - Etch Al with MF-321 for 70 s, H_2O 5 s, H_2O 10 s, IPA 5 s
    - Strip resist in 50 °C acetone for 1 h
    - Rinse in IPA for 30 s and N_2 blow dry
8. Ohmic contacts
    - Spin coat with PMMA 950A4 spin at 1500 rpm twice
    - Soft bake at 185 °C for 5 min
    - EBL exposure with 1500 $\mu C\,cm^{-2}$
    - Develop with MIBK:IPA 1:3 for 60 s, IPA for 30 s N_2 blow dry
    - In situ argon milling
    - Evaporate 10 nm Ti
    - Evaporate 150 nm Au
    - Strip resist in 50 °C acetone overnight
    - Rinse in IPA for 30 s and N_2 blow dry

9. Deposit local ALD layer, see Fig. 3.3
    Spin coat with PMMA 950A4 spin at 4000 rpm
    Soft bake at 185 °C for 5 min
    EBL exposure with 1400 µC cm^{-2}
    Develop with MIBK:IPA 1:3 for 60 s, IPA for 30 s N_2 blow dry
    Deposit 10 nm Al_2O_3 layer at 105 °C with ALD.
    Spin coat with PMMA 950A6 at 4000 rpm
    Soft bake at 185 °C for 5 min
    EBL exposure with 2000 µC cm^{-2}
    Develop with MIBK:IPA 1:3 for 60 s, IPA for 30 s N_2 blow dry
    Etch Al with MF-321 for 4 min, H_2O 5 s, H_2O 10 s, IPA 5 s
    Liftoff resist in 50 °C acetone overnight
    Rinse in IPA for 30 s and N_2 blow dry
10. Deposit gate layer
    Spin coat with PMMA 950A4 spin at 3500 rpm
    Soft bake at 185 °C for 5 min
    EBL exposure with 900 µC cm^{-2}
    Develop with MIBK:IPA 1:3 for 60 s, IPA for 30 s N_2 blow dry
    Evaporate 10 nm Ti
    Evaporate 150 nm Au
    Liftoff resist in 50 °C acetone overnight
    Rinse in IPA for 30 s and N_2 blow dry

BIBLIOGRAPHY

[1] P. Lenard, *Ueber die lichtelektrische wirkung,* Annalen der Physik **313**, 149 (1902).

[2] A. Einstein, *Über einen die erzeugung und verwandlung des lichtes betreffenden heuristischen gesichtspunkt,* Annalen der Physik **322**, 132 (1905).

[3] G. P. Thomson and A. Reid, *Diffraction of cathode rays by a thin film,* Nature **119**, 890 (1927).

[4] C. J. Davisson and L. H. Germer, *Reflection of electrons by a crystal of nickel,* Proceedings of the National Academy of Sciences **14**, 317 (1928).

[5] N. Bohr, *I. on the constitution of atoms and molecules,* The London, Edinburgh, and Dublin Philosophical Magazine and Journal of Science **26**, 1 (1913).

[6] E. Schrödinger, *Quantisierung als eigenwertproblem,* Annalen der Physik **384**, 361 (1926).

[7] W. Pauli, *Über das wasserstoffspektrum vom standpunkt der neuen quantenmechanik,* Zeitschrift für Physik A Hadrons and nuclei **36**, 336 (1926).

[8] H. Kamerlingh Onnes, *Further experiments with liquid helium. C. On the change of electric resistance of pure metals at very low temperatures etc. IV. The resistance of pure mercury at helium temperatures,* Koninklijke Nederlandsche Akademie van Wetenschappen Proceedings **13**, 1274 (1911).

[9] P. W. Anderson, *More is different,* Science **177**, 393 (1972).

[10] R. P. Feynman, *Simulating physics with computers,* International Journal of Theoretical Physics **21**, 467 (1982).

[11] D. Deutsch, *Quantum theory, the church–turing principle and the universal quantum computer,* Proceedings of the Royal Society of London. A. Mathematical and Physical Sciences **400**, 97 (1985).

[12] M. A. Nielsen and I. L. Chuang, *Quantum Computation and Quantum Information* (Cambridge University Press, 2000).

[13] P. Kuttner, *The rope memory, a permanent storage device,* in *AFIPS Conference Proceedings, Fall Joint Computer Conference,* Vol. 24 (1963) pp. 45–57.

[14] A. L. Hopkins, R. L. Alonso, and H. Blair-Smith, *Logical description for apollo guidance computer (AGC 4),* MIT Instrumentation Laboratory Report R-393 (1963).

[15] W. H. Aldrich and R. L. Alonso, *The "braid" transformer memory,* IEEE Transactions on Electronic Computers **EC-15**, 502 (1966).

[16] C. Nayak, S. H. Simon, A. Stern, M. Freedman, and S. D. Sarma, *Non-abelian anyons and topological quantum computation,* Reviews of Modern Physics **80**, 1083 (2008).

[17] A. Y. Kitaev, *Unpaired majorana fermions in quantum wires,* Physics-Uspekhi **44**, 131 (2001).

[18] M. Leijnse and K. Flensberg, *Introduction to topological superconductivity and majorana fermions,* Semiconductor Science and Technology **27**, 124003 (2012).

[19] R. M. Lutchyn, J. D. Sau, and S. D. Sarma, *Majorana fermions and a topological phase transition in semiconductor-superconductor heterostructures,* Physical Review Letters **105**, 077001 (2010).

[20] Y. Oreg, G. Refael, and F. von Oppen, *Helical liquids and majorana bound states in quantum wires,* Physical Review Letters **105**, 177002 (2010).

[21] V. Mourik, K. Zuo, S. M. Frolov, S. R. Plissard, E. P. A. M. Bakkers, and L. P. Kouwenhoven, *Signatures of majorana fermions in hybrid superconductor-semiconductor nanowire devices,* Science **336**, 1003 (2012).

[22] J. Alicea, Y. Oreg, G. Refael, F. von Oppen, and M. P. A. Fisher, *Non-abelian statistics and topological quantum information processing in 1d wire networks,* Nature Physics **7**, 412 (2011).

[23] T. Hyart, B. van Heck, I. C. Fulga, M. Burrello, A. R. Akhmerov, and C. W. J. Beenakker, *Flux-controlled quantum computation with majorana fermions,* Physical Review B **88**, 035121 (2013).

[24] D. Aasen, M. Hell, R. V. Mishmash, A. Higginbotham, J. Danon, M. Leijnse, T. S. Jespersen, J. A. Folk, C. M. Marcus, K. Flensberg, and J. Alicea, *Milestones toward majorana-based quantum computing,* Physical Review X **6**, 031016 (2016).

[25] S. Plugge, A. Rasmussen, R. Egger, and K. Flensberg, *Majorana box qubits,* New Journal of Physics **19**, 012001 (2017).

[26] T. Karzig, C. Knapp, R. M. Lutchyn, P. Bonderson, M. B. Hastings, C. Nayak, J. Alicea, K. Flensberg, S. Plugge, Y. Oreg, C. M. Marcus, and M. H. Freedman, *Scalable designs for quasiparticle-poisoning-protected topological quantum computation with majorana zero modes,* Physical Review B **95**, 235305 (2017).

[27] P. Bonderson, M. Freedman, and C. Nayak, *Measurement-only topological quantum computation,* Physical Review Letters **101**, 010501 (2008).

[28] M. A. Reed, R. T. Bate, K. Bradshaw, W. M. Duncan, W. R. Frensley, J. W. Lee, and H. D. Shih, *Spatial quantization in gaas–algaas multiple quantum dots,* Journal of Vacuum Science & Technology B: Microelectronics Processing and Phenomena **4**, 358 (1986).

[29] M. A. Reed, *Quantum dots,* Scientific American **268**, 118 (1993).

[30] M. A. Kastner, *Artificial atoms,* Physics Today **46**, 24 (1993).

[31] L. P. Kouwenhoven, C. M. Marcus, P. L. McEuen, S. Tarucha, R. M. Westervelt, and N. S. Wingreen, *Electron transport in quantum dots,* in *Mesoscopic Electron Transport* (Springer Netherlands, 1997) pp. 105–214.

[32] T. Ihn, *Semiconductor Nanostructures: Quantum States and Electronic Transport* (Oxford University Press Inc., 2010).

[33] M. Reed, J. Randall, R. Aggarwal, R. Matyi, T. Moore, and A. Wetsel, *Observation of discrete electronic states in a zero-dimensional semiconductor nanostructure,* Physical Review Letters **60**, 535 (1988).

[34] C. G. Smith, M. Pepper, H. Ahmed, J. E. F. Frost, D. G. Hasko, D. C. Peacock, D. A. Ritchie, and G. A. C. Jones, *The transition from one- to zero-dimensional ballistic transport,* Journal of Physics C: Solid State Physics **21**, L893 (1988).

[35] B. J. van Wees, L. P. Kouwenhoven, C. J. P. M. Harmans, J. G. Williamson, C. E. Timmering, M. E. I. Broekaart, C. T. Foxon, and J. J. Harris, *Observation of zero-dimensional states in a one-dimensional electron interferometer,* Phys. Rev. Lett. **62**, 2523 (1989).

[36] U. Meirav, M. A. Kastner, and S. J. Wind, *Single-electron charging and periodic conductance resonances in GaAs nanostructures,* Physical Review Letters **65**, 771 (1990).

[37] M. Bockrath, D. H. Cobden, P. L. McEuen, N. G. Chopra, A. Zettl, A. Thess, and R. E. Smalley, *Single-electron transport in ropes of carbon nanotubes,* Science **275**, 1922 (1997).

[38] S. J. Tans, M. H. Devoret, H. Dai, A. Thess, R. E. Smalley, L. J. Geerligs, and C. Dekker, *Individual single-wall carbon nanotubes as quantum wires,* Nature **386**, 474 (1997).

[39] S. D. Franceschi, J. A. van Dam, E. P. A. M. Bakkers, L. F. Feiner, L. Gurevich, and L. P. Kouwenhoven, *Single-electron tunneling in InP nanowires,* Applied Physics Letters **83**, 344 (2003).

[40] C. Thelander, T. Mårtensson, M. T. Björk, B. J. Ohlsson, M. W. Larsson, L. R. Wallenberg, and L. Samuelson, *Single-electron transistors in heterostructure nanowires,* Applied Physics Letters **83**, 2052 (2003).

[41] A. Pfund, I. Shorubalko, R. Leturcq, and K. Ensslin, *Top-gate defined double quantum dots in inas nanowires,* Applied Physics Letters **89**, 252106 (2006).

[42] Y. Nakamura, Y. A. Pashkin, and J. S. Tsai, *Coherent control of macroscopic quantum states in a single-cooper-pair box,* Nature **398**, 786 (1999).

[43] J. R. Petta, A. C. Johnson, J. M. Taylor, E. A. Laird, A. Yacoby, M. D. Lukin, C. M. Marcus, M. P. Hanson, and A. C. Gossard, *Coherent manipulation of coupled electron spins in semiconductor quantum dots,* Science **309**, 2180 (2005).

[44] R. J. Schoelkopf, P. Wahlgren, A. A. Kozhevnikov, P. Delsing, and D. E. Prober, *The radio-frequency single-electron transistor (rf-set): A fast and ultrasensitive electrometer,* Science **280**, 1238 (1998).

[45] R. C. Ashoori, H. L. Stormer, J. S. Weiner, L. N. Pfeiffer, S. J. Pearton, K. W. Baldwin, and K. W. West, *Single-electron capacitance spectroscopy of discrete quantum levels,* Physical Review Letters **68**, 3088 (1992).

[46] H. V. Houten, C. W. J. Beenakker, and A. A. M. Staring, *Coulomb-blockade oscillations in semiconductor nanostructures,* in *NATO ASI Series* (Springer US, 1992) pp. 167–216.

[47] P. L. McEuen, E. B. Foxman, J. Kinaret, U. Meirav, M. A. Kastner, N. S. Wingreen, and S. J. Wind, *Self-consistent addition spectrum of a coulomb island in the quantum hall regime,* Phys. Rev. B **45**, 11419 (1992).

[48] W. G. van der Wiel, S. De Franceschi, J. M. Elzerman, T. Fujisawa, S. Tarucha, and L. P. Kouwenhoven, *Electron transport through double quantum dots,* Reviews of Modern Physics **75**, 1 (2002).

[49] D. V. Averin and Y. V. Nazarov, *Macroscopic quantum tunneling of charge and cotunneling,* in *Single Charge Tunneling: Coulomb Blockade Phenomena in Nanostructures*, edited by H. Grabert and M. H. Devoret (Plenum Press and NATO Scientific Affairs Division, New York/London, 1992) pp. 217–247.

[50] W. Meissner and R. Ochsenfeld, *Ein neuer effekt bei eintritt der supraleitfähigkeit,* Die Naturwissenschaften **21**, 787 (1933).

[51] F. London and H. London, *The electromagnetic equations of the supraconductor,* Proceedings of the Royal Society of London. Series A - Mathematical and Physical Sciences **149**, 71 (1935).

[52] *On the theory of superconductivity,* in *Collected Papers of L.D. Landau*, edited by D. TER HAAR (Pergamon, 1965) pp. 546–568.

[53] J. Bardeen, L. N. Cooper, and J. R. Schrieffer, *Microscopic theory of superconductivity,* Physical Review **106**, 162 (1957).

[54] J. Bardeen, L. N. Cooper, and J. R. Schrieffer, *Theory of superconductivity,* Physical Review **108**, 1175 (1957).

[55] J. Bardeen, *Zero-point vibrations and superconductivity,* Physical Review **79**, 167 (1950).

[56] H. Fröhlich, *Theory of the superconducting state. i. the ground state at the absolute zero of temperature,* Physical Review **79**, 845 (1950).

[57] A. Altland and B. D. Simons, *Condensed Matter Field Theory*, 2nd ed. (Cambridge University Press, 2010).

[58] L. N. Cooper, *Bound electron pairs in a degenerate fermi gas,* Physical Review **104**, 1189 (1956).

[59] J. F. Annett, *Superconductivity, superfluids and condensates* (Oxford University Press, United Kingdom, 2004).

[60] M. Tinkham, *Introduction to superconductivity*, 2nd ed. (Dover publications, inc., 1996).

[61] A. Andreev, *The thermal conductivity of the intermediate state in superconductors,* JETP **19**, 1228 (1964).

[62] H. Shiba, *Classical spins in superconductors,* Progress of Theoretical Physics **40**, 435 (1968).

[63] L. YU, *Bound state in superconductors with paramagnetic impurities,* Acta Physica Sinica **21**, 75 (1965).

[64] A. I. Rusinov, *On the Theory of Gapless Superconductivity in Alloys Containing Paramagnetic Impurities,* Soviet Journal of Experimental and Theoretical Physics **29**, 1101 (1969).

[65] J. D. Sau, R. M. Lutchyn, S. Tewari, and S. D. Sarma, *Generic new platform for topological quantum computation using semiconductor heterostructures,* Physical Review Letters **104**, 040502 (2010).

[66] R. Mizuta, R. M. Otxoa, A. C. Betz, and M. F. Gonzalez-Zalba, *Quantum and tunneling capacitance in charge and spin qubits,* Physical Review B **95**, 045414 (2017).

[67] C. W. Groth, M. Wimmer, A. R. Akhmerov, and X. Waintal, *Kwant: a software package for quantum transport,* New Journal of Physics **16**, 063065 (2014).

[68] D. A. Steck, *Quantum and atom optics,* Available online at `http://steck.us/teaching` (revision 0.13.4, 24 September 2020).

[69] M. J. Collett and C. W. Gardiner, *Squeezing of intracavity and traveling-wave light fields produced in parametric amplification,* Physical Review A **30**, 1386 (1984).

[70] C. W. Gardiner and M. J. Collett, *Input and output in damped quantum systems: Quantum stochastic differential equations and the master equation,* Physical Review A **31**, 3761 (1985).

[71] K. D. Petersson, L. W. McFaul, M. D. Schroer, M. Jung, J. M. Taylor, A. A. Houck, and J. R. Petta, *Circuit quantum electrodynamics with a spin qubit,* Nature **490**, 380 (2012).

[72] P. A. M. Dirac, *The Principles of Quantum Mechanics*, 3rd ed. (Clarendon Press, Oxford, 1947).

[73] A. Blais, R.-S. Huang, A. Wallraff, S. M. Girvin, and R. J. Schoelkopf, *Cavity quantum electrodynamics for superconducting electrical circuits: An architecture for quantum computation,* Physical Review A **69**, 062320 (2004).

[74] M. S. Khalil, M. J. A. Stoutimore, F. C. Wellstood, and K. D. Osborn, *An analysis method for asymmetric resonator transmission applied to superconducting devices,* Journal of Applied Physics **111**, 054510 (2012).

[75] C. Deng, M. Otto, and A. Lupascu, *An analysis method for transmission measurements of superconducting resonators with applications to quantum-regime dielectric-loss measurements,* Journal of Applied Physics **114**, 054504 (2013).

[76] H. Guan, M. Dai, Q. He, J. Hu, P. Ouyang, Y. Wang, L. F. Wei, and J. Gao, *Network modeling of non-ideal superconducting resonator circuits,* Superconductor Science and Technology **33**, 075004 (2020).

[77] F. Wilczek and B. Devine, *How asymptotic freedom discovered me,* in *Longing for the Harmonies* (W. W. Norton & company, 1987).

[78] J. M. Hornibrook, J. I. Colless, A. C. Mahoney, X. G. Croot, S. Blanvillain, H. Lu, A. C. Gossard, and D. J. Reilly, *Frequency multiplexing for readout of spin qubits,* Applied Physics Letters **104**, 103108 (2014).

[79] J. Kroll, F. Borsoi, K. van der Enden, W. Uilhoorn, D. de Jong, M. Quintero-Pérez, D. van Woerkom, A. Bruno, S. Plissard, D. Car, E. Bakkers, M. Cassidy, and L. Kouwenhoven, *Magnetic-field-resilient superconducting coplanar-waveguide resonators for hybrid circuit quantum electrodynamics experiments,* Physical Review Applied **11**, 064053 (2019).

[80] P. Krogstrup, N. L. B. Ziino, W. Chang, S. M. Albrecht, M. H. Madsen, E. Johnson, J. Nygård, C. M. Marcus, and T. S. Jespersen, *Epitaxy of semiconductor–superconductor nanowires,* Nature Materials **14**, 400 (2015).

[81] J. Kammhuber, *Spin-Orbit Interaction in Ballistic Nanowire Devices*, Ph.D. thesis, Technische Universiteit Delft (2017).

[82] D. Bouman, *spins in josephson junctions*, Ph.D. thesis, Technische Universiteit Delft (2021).

[83] P. Apte and K. Saraswat, *Correlation of trap generation to charge-to-breakdown (Q_{bd}): a physical-damage model of dielectric breakdown,* IEEE Transactions on Electron Devices **41**, 1595 (1994).

[84] M. D. Groner, F. H. Fabreguette, J. W. Elam, and S. M. George, *Low-temperature Al_2O_3 atomic layer deposition,* Chemistry of Materials **16**, 639 (2004).

[85] I. Reklaitis, E. Radiunas, T. Malinauskas, S. Stanionytė, G. Juška, R. Ritasalo, T. Pilvi, S. Taeger, M. Strassburg, and R. Tomašiūnas, *A comparative study on atomic layer deposited oxide film morphology and their electrical breakdown,* Surface and Coatings Technology **399**, 126123 (2020).

[86] J. Boter, *Scaling Aspects of Silicon Spin Qubits*, Ph.D. thesis, Technische Universiteit Delft (2020).

[87] J. van Veen, *superconducting islands and gate-based readout in semiconductor nanowires*, Ph.D. thesis, Technische Universiteit Delft (2019).

[88] F. Pobell, *Matter and Methods at Low Temperatures*, 3rd ed. (Springer Berlin Heidelberg, 2007).

[89] C. Macklin, K. O'Brien, D. Hover, M. E. Schwartz, V. Bolkhovsky, X. Zhang, W. D. Oliver, and I. Siddiqi, *A near-quantum-limited josephson traveling-wave parametric amplifier,* Science **350**, 307 (2015).

[90] A. Wallraff, D. I. Schuster, A. Blais, L. Frunzio, J. Majer, M. H. Devoret, S. M. Girvin, and R. J. Schoelkopf, *Approaching unit visibility for control of a superconducting qubit with dispersive readout,* Physical Review Letters **95**, 060501 (2005).

[91] A. C. Betz, R. Wacquez, M. Vinet, X. Jehl, A. L. Saraiva, M. Sanquer, A. J. Ferguson, and M. F. Gonzalez-Zalba, *Dispersively detected pauli spin-blockade in a silicon nanowire field-effect transistor,* Nano Letters **15**, 4622 (2015).

[92] J. I. Colless, A. C. Mahoney, J. M. Hornibrook, A. C. Doherty, H. Lu, A. C. Gossard, and D. J. Reilly, *Dispersive readout of a few-electron double quantum dot with fast rf gate sensors,* Physical Review Letters **110**, 046805 (2013).

[93] R. Vijay, D. H. Slichter, and I. Siddiqi, *Observation of quantum jumps in a superconducting artificial atom,* Physical Review Letters **106**, 110502 (2011).

[94] N. J. Lambert, A. A. Esmail, M. Edwards, F. A. Pollock, B. W. Lovett, and A. J. Ferguson, *Quantum capacitance and charge sensing of a superconducting double dot,* Applied Physics Letters **109**, 112603 (2016).

[95] T. Frey, P. J. Leek, M. Beck, A. Blais, T. Ihn, K. Ensslin, and A. Wallraff, *Dipole coupling of a double quantum dot to a microwave resonator,* Physical Review Letters **108**, 046807 (2012).

[96] M. D. Schroer, M. Jung, K. D. Petersson, and J. R. Petta, *Radio frequency charge parity meter,* Physical Review Letters **109**, 166804 (2012).

[97] A. West, B. Hensen, A. Jouan, T. Tanttu, C.-H. Yang, A. Rossi, M. F. Gonzalez-Zalba, F. Hudson, A. Morello, D. J. Reilly, and A. S. Dzurak, *Gate-based single-shot readout of spins in silicon,* Nature Nanotechnology **14**, 437 (2019).

[98] P. Pakkiam, A. V. Timofeev, M. G. House, M. R. Hogg, T. Kobayashi, M. Koch, S. Rogge, and M. Y. Simmons, *Single-shot single-gate rf spin readout in silicon,* Physical Review X **8**, 041032 (2018).

[99] M. Urdampilleta, D. J. Niegemann, E. Chanrion, B. Jadot, C. Spence, P.-A. Mortemousque, C. Bäuerle, L. Hutin, B. Bertrand, S. Barraud, R. Maurand, M. Sanquer, X. Jehl, S. D. Franceschi, M. Vinet, and T. Meunier, *Gate-based high fidelity spin readout in a CMOS device,* Nature Nanotechnology **14**, 737 (2019).

[100] T. Walter, P. Kurpiers, S. Gasparinetti, P. Magnard, A. Potočnik, Y. Salathé, M. Pechal, M. Mondal, M. Oppliger, C. Eichler, and A. Wallraff, *Rapid high-fidelity single-shot dispersive readout of superconducting qubits,* Physical Review Applied **7**, 054020 (2017).

[101] S. Nadj-Perge, S. M. Frolov, E. P. A. M. Bakkers, and L. P. Kouwenhoven, *Spin–orbit qubit in a semiconductor nanowire,* Nature **468**, 1084 (2010).

[102] A. Das, Y. Ronen, Y. Most, Y. Oreg, M. Heiblum, and H. Shtrikman, *Zero-bias peaks and splitting in an al–InAs nanowire topological superconductor as a signature of majorana fermions,* Nature Physics **8**, 887 (2012).

[103] S. M. Albrecht, A. P. Higginbotham, M. Madsen, F. Kuemmeth, T. S. Jespersen, J. Nygård, P. Krogstrup, and C. M. Marcus, *Exponential protection of zero modes in majorana islands,* Nature **531**, 206 (2016).

[104] T. Ota, T. Hayashi, K. Muraki, and T. Fujisawa, *Wide-band capacitance measurement on a semiconductor double quantum dot for studying tunneling dynamics,* Applied Physics Letters **96**, 032104 (2010).

[105] T. Duty, G. Johansson, K. Bladh, D. Gunnarsson, C. Wilson, and P. Delsing, *Observation of quantum capacitance in the cooper-pair transistor,* Physical Review Letters **95**, 206807 (2005).

[106] K. D. Petersson, C. G. Smith, D. Anderson, P. Atkinson, G. A. C. Jones, and D. A. Ritchie, *Charge and spin state readout of a double quantum dot coupled to a resonator,* Nano Letters **10**, 2789 (2010).

[107] M. A. Castellanos-Beltran, K. D. Irwin, G. C. Hilton, L. R. Vale, and K. W. Lehnert, *Amplification and squeezing of quantum noise with a tunable josephson metamaterial,* Nature Physics **4**, 929 (2008).

[108] J. Stehlik, Y.-Y. Liu, C. M. Quintana, C. Eichler, T. R. Hartke, and J. R. Petta, *Fast charge sensing of a cavity-coupled double quantum dot using a josephson parametric amplifier,* Physical Review Applied **4**, 014018 (2015).

[109] F. J. Schupp, F. Vigneau, Y. Wen, A. Mavalankar, J. Griffiths, G. A. C. Jones, I. Farrer, D. A. Ritchie, C. G. Smith, L. C. Camenzind, L. Yu, D. M. Zumbühl, G. A. D. Briggs, N. Ares, and E. A. Laird, *Sensitive radiofrequency readout of quantum dots using an ultra-low-noise SQUID amplifier,* Journal of Applied Physics **127**, 244503 (2020).

[110] I. Ahmed, J. A. Haigh, S. Schaal, S. Barraud, Y. Zhu, C. Lee, M. Amado, J. W. A. Robinson, A. Rossi, J. J. L. Morton, and M. F. Gonzalez-Zalba, *Radio-frequency capacitive gate-based sensing,* Physical Review Applied **10**, 014018 (2018).

[111] S. De Franceschi, L. P. Kouwenhoven, C. Schönenberger, and W. Wernsdorfer, *Hybrid superconductor–quantum dot devices,* Nature Nanotechnology **5**, 703 (2010).

[112] J. A. Van Dam, Y. V. Nazarov, E. P. A. M. Bakkers, S. De Franceschi, and L. P. Kouwenhoven, *Supercurrent reversal in quantum dots,* Nature **442**, 667 (2006).

[113] D. B. Szombati, S. Nadj-Perge, D. Car, S. R. Plissard, E. P. A. M. Bakkers, and L. P. Kouwenhoven, *Josephson ϕ_0-junction in nanowire quantum dots,* Nature Physics **12**, 568 (2016).

[114] L. Hofstetter, S. Csonka, J. Nygård, and C. Schönenberger, *Cooper pair splitter realized in a two-quantum-dot Y-junction,* Nature **461**, 960 (2009).

[115] L. G. Herrmann, F. Portier, P. Roche, A. Levy Yeyati, T. Kontos, and C. Strunk, *Carbon nanotubes as Cooper-pair beam splitters,* Physical review letters **104**, 026801 (2010).

[116] R. S. Deacon, A. Oiwa, J. Sailer, S. Baba, Y. Kanai, K. Shibata, K. Hirakawa, and S. Tarucha, *Cooper pair splitting in parallel quantum dot Josephson junctions,* Nature communications **6**, 7446 (2015).

[117] D. C. Ralph, C. T. Black, and M. Tinkham, *Spectroscopic measurements of discrete electronic states in single metal particles,* Physical review letters **74**, 3241 (1995).

[118] E. J. H. Lee, X. Jiang, M. Houzet, R. Aguado, C. M. Lieber, and S. De Franceschi, *Spin-resolved Andreev levels and parity crossings in hybrid superconductor–semiconductor nanostructures,* Nature nanotechnology **9**, 79 (2014).

[119] M. T. Deng, S. Vaitiekenas, E. B. Hansen, J. Danon, M. Leijnse, K. Flensberg, J. Nygård, P. Krogstrup, and C. M. Marcus, *Majorana bound state in a coupled quantum-dot hybrid-nanowire system,* Science **354**, 1557 (2016).

[120] A. P. Higginbotham, S. M. Albrecht, G. Kiršanskas, W. Chang, F. Kuemmeth, P. Krogstrup, T. S. Jespersen, J. Nygård, K. Flensberg, and C. M. Marcus, *Parity lifetime of bound states in a proximitized semiconductor nanowire,* Nature Phys. **11**, 1017 (2015).

[121] A. Wallraff, D. I. Schuster, A. Blais, L. Frunzio, R.-. S. Huang, J. Majer, S. Kumar, S. M. Girvin, and R. J. Schoelkopf, *Strong coupling of a single photon to a superconducting qubit using circuit quantum electrodynamics,* Nature **431**, 162 (2004).

[122] A. A. Esmail, A. J. Ferguson, and N. J. Lambert, *Cooper pair tunnelling and quasiparticle poisoning in a galvanically isolated superconducting double dot,* Applied Physics Letters **111**, 252602 (2017).

[123] A. J. Landig, J. V. Koski, P. Scarlino, C. Reichl, W. Wegscheider, A. Wallraff, K. Ensslin, and T. Ihn, *Microwave-Cavity-Detected Spin Blockade in a Few-Electron Double Quantum Dot,* Physical Review Letters **122**, 213601 (2019).

[124] M. F. Gonzalez-Zalba, S. Barraud, A. J. Ferguson, and A. C. Betz, *Probing the limits of gate-based charge sensing,* Nature communications **6**, 6084 (2015).

[125] L. E. Bruhat, J. J. Viennot, M. C. Dartiailh, M. M. Desjardins, T. Kontos, and A. Cottet, *Cavity photons as a probe for charge relaxation resistance and photon emission in a quantum dot coupled to normal and superconducting continua,* Physical Review X **6**, 021014 (2016).

[126] L. E. Bruhat, T. Cubaynes, J. J. Viennot, M. C. Dartiailh, M. M. Desjardins, A. Cottet, and T. Kontos, *Circuit QED with a quantum-dot charge qubit dressed by Cooper pairs,* Physical Review B **98**, 155313 (2018).

[127] M. Hays, G. de Lange, K. Serniak, D. J. van Woerkom, D. Bouman, P. Krogstrup, J. Nygård, A. Geresdi, and M. H. Devoret, *Direct microwave measurement of Andreev-bound-state dynamics in a semiconductor-nanowire josephson junction,* Physical review letters **121**, 047001 (2018).

[128] L. Tosi, C. Metzger, M. F. Goffman, C. Urbina, H. Pothier, S. Park, A. Levi Yeyati, J. Nygård, and P. Krogstrup, *Spin-orbit splitting of Andreev states revealed by microwave spectroscopy,* Physical Review X **9**, 011010 (2019).

[129] A. E. Antipov, A. Bargerbos, G. W. Winkler, B. Bauer, E. Rossi, and R. M. Lutchyn, *Effects of gate-induced electric fields on semiconductor Majorana nanowires,* Phys. Rev. X **8**, 031041 (2018).

[130] D. V. Averin and Y. V. Nazarov, *Single-electron charging of a superconducting island,* Physical review letters **69**, 1993 (1992).

[131] B. Van Heck, R. M. Lutchyn, and L. I. Glazman, *Conductance of a proximitized nanowire in the Coulomb blockade regime,* Physical Review B **93**, 235431 (2016).

[132] F. W. J. Hekking, L. I. Glazman, K. A. Matveev, and R. I. Shekhter, *Coulomb blockade of two-electron tunneling,* Physical review letters **70**, 4138 (1993).

[133] M. Esterli, R. M. Otxoa, and M. F. Gonzalez-Zalba, *Small-signal equivalent circuit for double quantum dots at low-frequencies,* Applied Physics Letters **114**, 253505 (2019).

[134] A. Cottet, C. Mora, and T. Kontos, *Mesoscopic admittance of a double quantum dot,* Physical Review B **83**, 121311 (2011).

[135] M. Leijnse and K. Flensberg, *Coupling spin qubits via superconductors,* Physical review letters **111**, 060501 (2013).

[136] P. Lafarge, P. Joyez, D. Esteve, C. Urbina, and M. H. Devoret, *Measurement of the even-odd free-energy difference of an isolated superconductor,* Physical review letters **70**, 994 (1993).

[137] J. Majer, J. M. Chow, J. M. Gambetta, J. Koch, B. R. Johnson, J. A. Schreier, L. Frunzio, D. I. Schuster, A. A. Houck, A. Wallraff, A. Blais, M. H. Devoret, S. M. Girvin, and R. J. Schoelkopf, *Coupling superconducting qubits via a cavity bus,* Nature **449**, 443 (2007).

[138] M. A. Sillanpää, J. I. Park, and R. W. Simmonds, *Coherent quantum state storage and transfer between two phase qubits via a resonant cavity,* Nature **449**, 438 (2007).

[139] P. Scarlino, D. J. van Woerkom, U. C. Mendes, J. V. Koski, A. J. Landig, C. K. Andersen, S. Gasparinetti, C. Reichl, W. Wegscheider, K. Ensslin, T. Ihn, A. Blais, and A. Wallraff, *Coherent microwave-photon-mediated coupling between a semiconductor and a superconducting qubit,* Nature Communications **10**, 3011 (2019).

[140] F. Borjans, X. G. Croot, X. Mi, M. J. Gullans, and J. R. Petta, *Resonant microwave-mediated interactions between distant electron spins,* Nature **577**, 195 (2019).

[141] M. Jerger, S. Poletto, P. Macha, U. Hübner, E. Il'ichev, and A. V. Ustinov, *Frequency division multiplexing readout and simultaneous manipulation of an array of flux qubits,* Applied Physics Letters **101**, 042604 (2012).

[142] E. Jeffrey, D. Sank, J. Mutus, T. White, J. Kelly, R. Barends, Y. Chen, Z. Chen, B. Chiaro, A. Dunsworth, A. Megrant, P. O'Malley, C. Neill, P. Roushan, A. Vainsencher, J. Wenner, A. Cleland, and J. M. Martinis, *Fast accurate state measurement with superconducting qubits,* Physical Review Letters **112**, 190504 (2014).

[143] M. R. Delbecq, V. Schmitt, F. D. Parmentier, N. Roch, J. J. Viennot, G. Fève, B. Huard, C. Mora, A. Cottet, and T. Kontos, *Coupling a quantum dot, fermionic leads, and a microwave cavity on a chip,* Physical Review Letters **107**, 256804 (2011).

[144] G. Puebla-Hellmann and A. Wallraff, *Realization of gigahertz-frequency impedance matching circuits for nano-scale devices,* Applied Physics Letters **101**, 053108 (2012).

[145] T. Hasler, M. Jung, V. Ranjan, G. Puebla-Hellmann, A. Wallraff, and C. Schönenberger, *Shot noise of a quantum dot measured with gigahertz impedance matching,* Physical Review Applied **4**, 054002 (2015).

[146] V. Ranjan, G. Puebla-Hellmann, M. Jung, T. Hasler, A. Nunnenkamp, M. Muoth, C. Hierold, A. Wallraff, and C. Schönenberger, *Clean carbon nanotubes coupled to superconducting impedance-matching circuits,* Nature Communications **6**, 7165 (2015).

[147] X. Mi, J. V. Cady, D. M. Zajac, P. W. Deelman, and J. R. Petta, *Strong coupling of a single electron in silicon to a microwave photon,* Science **355**, 156 (2016).

[148] A. Stockklauser, P. Scarlino, J. Koski, S. Gasparinetti, C. Andersen, C. Reichl, W. Wegscheider, T. Ihn, K. Ensslin, and A. Wallraff, *Strong coupling cavity QED with gate-defined double quantum dots enabled by a high impedance resonator,* Physical Review X **7**, 011030 (2017).

[149] A. J. Landig, J. V. Koski, P. Scarlino, U. C. Mendes, A. Blais, C. Reichl, W. Wegscheider, A. Wallraff, K. Ensslin, and T. Ihn, *Coherent spin–photon coupling using a resonant exchange qubit,* Nature **560**, 179 (2018).

[150] X. Mi, M. Benito, S. Putz, D. M. Zajac, J. M. Taylor, G. Burkard, and J. R. Petta, *A coherent spin–photon interface in silicon,* Nature **555**, 599 (2018).

[151] N. Samkharadze, G. Zheng, N. Kalhor, D. Brousse, A. Sammak, U. C. Mendes, A. Blais, G. Scappucci, and L. M. K. Vandersypen, *Strong spin-photon coupling in silicon,* Science **359**, 1123 (2018).

[152] G. Zheng, N. Samkharadze, M. L. Noordam, N. Kalhor, D. Brousse, A. Sammak, G. Scappucci, and L. M. K. Vandersypen, *Rapid gate-based spin read-out in silicon using an on-chip resonator,* Nature Nanotechnology **14**, 742 (2019).

[153] J. V. Koski, A. J. Landig, M. Russ, J. C. Abadillo-Uriel, P. Scarlino, B. Kratochwil, C. Reichl, W. Wegscheider, G. Burkard, M. Friesen, S. N. Coppersmith, A. Wallraff, K. Ensslin, and T. Ihn, *Strong photon coupling to the quadrupole moment of an electron in a solid-state qubit,* Nature Physics **16**, 642 (2020).

[154] M.-C. Harabula, T. Hasler, G. Fülöp, M. Jung, V. Ranjan, and C. Schönenberger, *Measuring a quantum dot with an impedance-matching on-chip superconducting LC resonator at gigahertz frequencies,* Physical Review Applied **8**, 054006 (2017).

[155] N. Holman, D. Rosenberg, D. Yost, J. L. Yoder, R. Das, W. D. Oliver, R. McDermott, and M. A. Eriksson, *Dispersive measurement of a semiconductor double quantum dot via 3d integration of a high-impedance tin resonator,* (2020), arXiv:2011.08759 [cond-mat.mes-hall] .

[156] A. Ruffino, T.-Y. Yang, J. Michniewicz, Y. Peng, E. Charbon, and M. F. Gonzalez-Zalba, *Integrated multiplexed microwave readout of silicon quantum dots in a cryogenic cmos chip,* (2021), arXiv:2101.08295 [quant-ph] .

[157] V. D. Maman, M. Gonzalez-Zalba, and A. Pályi, *Charge noise and overdrive errors in dispersive readout of charge, spin, and majorana qubits,* Physical Review Applied **14**, 064024 (2020).

[158] S. J. Chorley, J. Wabnig, Z. V. Penfold-Fitch, K. D. Petersson, J. Frake, C. G. Smith, and M. R. Buitelaar, *Measuring the complex admittance of a carbon nanotube double quantum dot,* Physical Review Letters **108**, 036802 (2012).

[159] D. Razmadze, D. Sabonis, F. K. Malinowski, G. C. Ménard, S. Pauka, H. Nguyen, D. M. van Zanten, E. C. O'Farrell, J. Suter, P. Krogstrup, F. Kuemmeth, and C. M. Marcus, *Radio-frequency methods for majorana-based quantum devices: Fast charge sensing and phase-diagram mapping,* Physical Review Applied **11**, 064011 (2019).

[160] S. Probst, F. B. Song, P. A. Bushev, A. V. Ustinov, and M. Weides, *Efficient and robust analysis of complex scattering data under noise in microwave resonators,* Review of Scientific Instruments **86**, 024706 (2015).

[161] J. Gabelli, G. Fève, J.-M. Berroir, B. Plaçais, A. Cavanna, B. Etienne, Y. Jin, and D. C. Glattli, *Violation of kirchhoff's laws for a coherent rc circuit,* Science **313**, 499 (2006).

[162] M. Jung, M. D. Schroer, K. D. Petersson, and J. R. Petta, *Radio frequency charge sensing in InAs nanowire double quantum dots,* Applied Physics Letters **100**, 253508 (2012).

[163] N. Ares, F. Schupp, A. Mavalankar, G. Rogers, J. Griffiths, G. Jones, I. Farrer, D. Ritchie, C. Smith, A. Cottet, G. Briggs, and E. Laird, *Sensitive radio-frequency measurements of a quantum dot by tuning to perfect impedance matching,* Physical Review Applied **5**, 034011 (2016).

[164] D. de Jong, J. van Veen, L. Binci, A. Singh, P. Krogstrup, L. P. Kouwenhoven, W. Pfaff, and J. D. Watson, *Rapid detection of coherent tunneling in an InAs nanowire quantum dot through dispersive gate sensing,* Physical Review Applied **11**, 044061 (2019).

[165] D. Sabonis, E. C. T. O'Farrell, D. Razmadze, D. M. T. van Zanten, J. Suter, P. Krogstrup, and C. M. Marcus, *Dispersive sensing in hybrid InAs/al nanowires,* Applied Physics Letters **115**, 102601 (2019).

[166] A. Crippa, R. Ezzouch, A. Aprá, A. Amisse, R. Laviéville, L. Hutin, B. Bertrand, M. Vinet, M. Urdampilleta, T. Meunier, M. Sanquer, X. Jehl, R. Maurand, and S. D. Franceschi, *Gate-reflectometry dispersive readout and coherent control of a spin qubit in silicon,* Nature Communications **10**, 2776 (2019).

[167] S. Park, C. Metzger, L. Tosi, M. Goffman, C. Urbina, H. Pothier, and A. L. Yeyati, *From adiabatic to dispersive readout of quantum circuits,* Physical Review Letters **125**, 077701 (2020).

[168] T. B. Smith, M. C. Cassidy, D. J. Reilly, S. D. Bartlett, and A. L. Grimsmo, *Dispersive readout of majorana qubits,* PRX Quantum **1**, 020313 (2020).

[169] D. Pozar, *Microwave Engineering, 4th Edition* (Wiley, Hoboken, NJ, 2011).

[170] Z. Tan, D. Cox, T. Nieminen, P. Lähteenmäki, D. Golubev, G. Lesovik, and P. Hakonen, *Cooper pair splitting by means of graphene quantum dots,* Physical Review Letters **114**, 096602 (2015).

[171] G. Ménard, G. Anselmetti, E. Martinez, D. Puglia, F. Malinowski, J. Lee, S. Choi, M. Pendharkar, C. Palmstrøm, K. Flensberg, C. Marcus, L. Casparis, and A. Higginbotham, *Conductance-matrix symmetries of a three-terminal hybrid device,* Physical Review Letters **124**, 036802 (2020).

[172] D. de Jong, C. Prosko, D. M. A. Waardenburg, L. Han, F. K. Malinowski, P. Krogstrup, L. P. Kouwenhoven, J. V. Koski, and W. Pfaff, *Data repository accompanying "rapid microwave-only characterization and readout of quantum dots using multiplexed gigahertz-frequency resonators",* https://doi.org/10.5281/zenodo.5036156 (2021).

[173] D. Loss and D. P. DiVincenzo, *Quantum computation with quantum dots,* Physical Review A **57**, 120 (1998).

[174] G. Lesovik, T. Martin, and G. Blatter, *Electronic entanglement in the vicinity of a superconductor,* The European Physical Journal B **24**, 287 (2001).

[175] A. Einstein, B. Podolsky, and N. Rosen, *Can quantum-mechanical description of physical reality be considered complete?* Physical Review **47**, 777 (1935).

[176] J. S. Bell, *On the einstein podolsky rosen paradox,* Physics Physique Fizika **1**, 195 (1964).

[177] N. M. Chtchelkatchev, G. Blatter, G. B. Lesovik, and T. Martin, *Bell inequalities and entanglement in solid-state devices,* Physical Review B **66**, 161320 (2002).

[178] P. Samuelsson, E. V. Sukhorukov, and M. Büttiker, *Orbital entanglement and violation of bell inequalities in mesoscopic conductors,* Physical Review Letters **91**, 157002 (2003).

[179] P. Recher, E. V. Sukhorukov, and D. Loss, *Andreev tunneling, coulomb blockade, and resonant transport of nonlocal spin-entangled electrons,* Physical Review B **63**, 165314 (2001).

[180] A. Das, Y. Ronen, M. Heiblum, D. Mahalu, A. V. Kretinin, and H. Shtrikman, *High-efficiency cooper pair splitting demonstrated by two-particle conductance resonance and positive noise cross-correlation,* Nature Communications **3**, 1165 (2012).

[181] J. Schindele, A. Baumgartner, and C. Schönenberger, *Near-unity cooper pair splitting efficiency,* Physical Review Letters **109**, 157002 (2012).

[182] I. V. Borzenets, Y. Shimazaki, G. F. Jones, M. F. Craciun, S. Russo, M. Yamamoto, and S. Tarucha, *High efficiency CVD graphene-lead (Pb) cooper pair splitter,* Scientific Reports **6**, 23051 (2016).

[183] S. Baba, C. Jünger, S. Matsuo, A. Baumgartner, Y. Sato, H. Kamata, K. Li, S. Jeppesen, L. Samuelson, H. Q. Xu, C. Schönenberger, and S. Tarucha, *Cooper-pair splitting in two parallel InAs nanowires,* New Journal of Physics **20**, 063021 (2018).

[184] A. Ranni, F. Brange, E. T. Mannila, C. Flindt, and V. F. Maisi, *Real-time observation of cooper pair splitting showing strong non-local correlations,* (2020), arXiv:2012.10373 .

[185] A. Cottet, T. Kontos, and A. L. Yeyati, *Subradiant split cooper pairs,* Physical Review Letters **108**, 166803 (2012).

[186] A. Cottet, *Probing coherent cooper pair splitting with cavity photons,* Physical Review B **90**, 125139 (2014).

[187] D. de Jong, C. G. Prosko, D. M. A. Waardenburg, L. Han, F. K. Malinowski, P. Krogstrup, L. P. Kouwenhoven, J. V. Koski, and W. Pfaff, *Rapid microwave-only characterization and readout of quantum dots using multiplexed gigahertz-frequency resonators,* Physical Review Applied **16**, 014007 (2021).

[188] F. R. Braakman, P. Barthelemy, C. Reichl, W. Wegscheider, and L. M. K. Vandersypen, *Long-distance coherent coupling in a quantum dot array,* Nature Nanotechnology **8**, 432 (2013).

[189] J. van Veen, D. de Jong, L. Han, C. Prosko, P. Krogstrup, J. D. Watson, L. P. Kouwenhoven, and W. Pfaff, *Revealing charge-tunneling processes between a quantum dot and a superconducting island through gate sensing,* Physical Review B **100**, 174508 (2019).

[190] N. J. Lambert, M. Edwards, C. Ciccarelli, and A. J. Ferguson, *A charge parity ammeter,* Nano Letters **14**, 1148 (2014).

[191] S. Heedt, M. Quintero-Pérez, F. Borsoi, A. Fursina, N. van Loo, G. P. Mazur, M. P. Nowak, M. Ammerlaan, K. Li, S. Korneychuk, J. Shen, M. A. Y. van de Poll, G. Badawy, S. Gazibegovic, N. de Jong, P. Aseev, K. van Hoogdalem, E. P. A. M. Bakkers, and L. P. Kouwenhoven, *Shadow-wall lithography of ballistic superconductor–semiconductor quantum devices,* Nature Communications **12**, 4914 (2021).

[192] F. A. Zwanenburg, A. S. Dzurak, A. Morello, M. Y. Simmons, L. C. L. Hollenberg, G. Klimeck, S. Rogge, S. N. Coppersmith, and M. A. Eriksson, *Silicon quantum electronics,* Reviews of Modern Physics **85**, 961 (2013).

[193] M. Kjaergaard, F. Nichele, H. J. Suominen, M. P. Nowak, M. Wimmer, A. R. Akhmerov, J. A. Folk, K. Flensberg, J. Shabani, C. J. Palmstrøm, and C. M. Marcus, *Quantized conductance doubling and hard gap in a two-dimensional semiconductor–superconductor heterostructure,* Nature Communications **7**, 12841 (2016).

[194] R. Hanson, L. P. Kouwenhoven, J. R. Petta, S. Tarucha, and L. M. K. Vandersypen, *Spins in few-electron quantum dots,* Reviews of Modern Physics **79**, 1217 (2007).

[195] Z. Scherübl, A. Pályi, and S. Csonka, *Probing individual split cooper pairs using the spin qubit toolkit,* Physical Review B **89**, 205439 (2014).

[196] K. Ono, *Current rectification by pauli exclusion in a weakly coupled double quantum dot system,* Science **297**, 1313 (2002).

[197] J. M. Elzerman, R. Hanson, L. H. W. van Beveren, B. Witkamp, L. M. K. Vandersypen, and L. P. Kouwenhoven, *Single-shot read-out of an individual electron spin in a quantum dot,* Nature **430**, 431 (2004).

[198] V. N. Golovach, M. Borhani, and D. Loss, *Electric-dipole-induced spin resonance in quantum dots,* Physical Review B **74**, 165319 (2006).

[199] C. Flindt, A. S. Sørensen, and K. Flensberg, *Spin-orbit mediated control of spin qubits,* Physical Review Letters **97**, 240501 (2006).

[200] K. C. Nowack, F. H. L. Koppens, Y. V. Nazarov, and L. M. K. Vandersypen, *Coherent control of a single electron spin with electric fields,* Science **318**, 1430 (2007).

[201] M. D. Schroer, K. D. Petersson, M. Jung, and J. R. Petta, *Field tuning the g Factor in InAs nanowire double quantum dots,* Physical Review Letters **107**, 176811 (2011).

[202] A. M. Turing, *I.—computing machinery and intelligence,* Mind **LIX**, 433 (1950).

[203] K. T. Law, P. A. Lee, and T. K. Ng, *Majorana fermion induced resonant andreev reflection,* Physical Review Letters **103**, 237001 (2009).

[204] K. Flensberg, *Tunneling characteristics of a chain of majorana bound states,* Physical Review B **82**, 180516 (2010).

[205] J. D. Sau, S. Tewari, R. M. Lutchyn, T. D. Stanescu, and S. D. Sarma, *Non-abelian quantum order in spin-orbit-coupled semiconductors: Search for topological majorana particles in solid-state systems,* Physical Review B **82**, 214509 (2010).

[206] E. Prada, P. San-Jose, M. W. A. de Moor, A. Geresdi, E. J. H. Lee, J. Klinovaja, D. Loss, J. Nygård, R. Aguado, and L. P. Kouwenhoven, *From andreev to majorana bound states in hybrid superconductor–semiconductor nanowires,* Nature Reviews Physics **2**, 575–594 (2020).

[207] T. . Rosdahl, A. Vuik, M. Kjaergaard, and A. R. Akhmerov, *Andreev rectifier: A nonlocal conductance signature of topological phase transitions,* Physical Review B **97**, 045421 (2018).

[208] H. Pan, J. D. Sau, and S. D. Sarma, *Three-terminal nonlocal conductance in majorana nanowires: Distinguishing topological and trivial in realistic systems with disorder and inhomogeneous potential,* Physical Review B **103**, 014513 (2021).

[209] C. Knapp, T. Karzig, R. M. Lutchyn, and C. Nayak, *Dephasing of majorana-based qubits,* Physical Review B **97**, 125404 (2018).

[210] T. Karzig, W. S. Cole, and D. I. Pikulin, *Quasiparticle poisoning of majorana qubits,* Physical Review Letters **126**, 057702 (2021).

[211] S. Gazibegovic, D. Car, H. Zhang, S. C. Balk, J. A. Logan, M. W. A. de Moor, M. C. Cassidy, R. Schmits, D. Xu, G. Wang, P. Krogstrup, R. L. M. O. het Veld, K. Zuo, Y. Vos, J. Shen, D. Bouman, B. Shojaei, D. Pennachio, J. S. Lee, P. J. van Veldhoven, S. Koelling, M. A. Verheijen, L. P. Kouwenhoven, C. J. Palmstrøm, and E. P. A. M. Bakkers, *Epitaxy of advanced nanowire quantum devices,* Nature **548**, 434 (2017).

[212] M. Reiher, N. Wiebe, K. M. Svore, D. Wecker, and M. Troyer, *Elucidating reaction mechanisms on quantum computers,* Proceedings of the National Academy of Sciences **114**, 7555 (2017).

[213] P. Aseev, A. Fursina, F. Boekhout, F. Krizek, J. E. Sestoft, F. Borsoi, S. Heedt, G. Wang, L. Binci, S. Martí-Sánchez, T. Swoboda, R. Koops, E. Uccelli, J. Arbiol, P. Krogstrup, L. P. Kouwenhoven, and P. Caroff, *Selectivity map for molecular beam epitaxy of advanced III–v quantum nanowire networks,* Nano Letters **19**, 218 (2018).

[214] F. Nichele, A. C. Drachmann, A. M. Whiticar, E. C. O'Farrell, H. J. Suominen, A. Fornieri, T. Wang, G. C. Gardner, C. Thomas, A. T. Hatke, P. Krogstrup, M. J. Manfra, K. Flensberg, and C. M. Marcus, *Scaling of majorana zero-bias conductance peaks,* Physical Review Letters **119**, 136803 (2017).

[215] C. T. Ke, C. M. Moehle, F. K. de Vries, C. Thomas, S. Metti, C. R. Guinn, R. Kallaher, M. Lodari, G. Scappucci, T. Wang, R. E. Diaz, G. C. Gardner, M. J. Manfra, and S. Goswami, *Ballistic superconductivity and tunable π-junctions in InSb quantum wells,* Nature Communications **10**, 3764 (2019).

[216] H. Ren, F. Pientka, S. Hart, A. T. Pierce, M. Kosowsky, L. Lunczer, R. Schlereth, B. Scharf, E. M. Hankiewicz, L. W. Molenkamp, B. I. Halperin, and A. Yacoby, *Topological superconductivity in a phase-controlled josephson junction,* Nature **569**, 93 (2019).

[217] D. J. Ibberson, T. Lundberg, J. A. Haigh, L. Hutin, B. Bertrand, S. Barraud, C.-M. Lee, N. A. Stelmashenko, G. A. Oakes, L. Cochrane, J. W. Robinson, M. Vinet, M. F. Gonzalez-Zalba, and L. A. Ibberson, *Large dispersive interaction between a CMOS double quantum dot and microwave photons,* PRX Quantum **2**, 020315 (2021).

[218] W. G. van der Wiel, T. Fujisawa, S. Tarucha, and L. P. Kouwenhoven, *A double quantum dot as an artificial two-level system,* Japanese Journal of Applied Physics **40**, 2100 (2001).

[219] D. M. T. van Zanten, D. Sabonis, J. Suter, J. I. Väyrynen, T. Karzig, D. I. Pikulin, E. C. T. O'Farrell, D. Razmadze, K. D. Petersson, P. Krogstrup, and C. M. Marcus, *Photon-assisted tunnelling of zero modes in a majorana wire,* Nature Physics **16**, 663 (2020).

[220] C. Janvier, L. Tosi, L. Bretheau, Ç. . Girit, M. Stern, P. Bertet, P. Joyez, D. Vion, D. Esteve, M. F. Goffman, H. Pothier, and C. Urbina, *Coherent manipulation of andreev states in superconducting atomic contacts,* Science **349**, 1199 (2015).

[221] D. I. Pikulin, J. P. Dahlhaus, M. Wimmer, H. Schomerus, and C. W. J. Beenakker, *A zero-voltage conductance peak from weak antilocalization in a majorana nanowire,* New Journal of Physics **14**, 125011 (2012).

[222] D. E. Liu, E. Rossi, and R. M. Lutchyn, *Impurity-induced states in superconducting heterostructures,* Physical Review B **97**, 161408 (2018).

ACKNOWLEDGEMENTS

The incredible amount of academic collaboration, technical assistance, and unwavering encouragement during my PhD have shaped the work in this thesis, and by extension, me personally. As such, I am indebted to all my colleagues and friends with whom I have interacted during the past few years. I want to take this opportunity to express my gratitude to you all.

First of all, **Leo K.**, thank you for letting me embark on this crazy journey. You have provided the tools, the environment, and the opportunities to develop myself as a scientist and as a person. I have appreciated your hands-off management style combined with cutting-edge physics discussions. I am especially grateful for creating the opportunity to do an internship at Microsoft, Santa Barbara. **Lieven**, thanks for agreeing to be my second promotor. **Wolfgang**, I am very happy that you agreed to join my graduation committee. Your personality has aided in creating a unique team dynamic and a delightful working environment. Your contagious enthusiasm for every experimental success is truly inspirational. I have no doubt amazing stuff will result from your new research group. **Simon**, your approach to the mentor programme should be an example to all! I wish to thank all members of the committee for reading and evaluating this thesis and the work it contains.

I am incredibly thankful to my paranymphs. **Christian M.**, Sorry for distracting you with a copious amount of coffee, but thanks a lot for distracting me back with beer. You are the ideal travel companion. I am very glad we went to San Sebastian together, all-in-all a marvelous experience. I wish you and **Elly** a bright future, wherever life will take you. **Arno**, thank you for the many physics related discussions over the years. I love your explorative nature, investigating physics, salt, or the inside of broom-cupboards. Your dark sense of humor was much appreciated, striking a delicate balance between optimism when possible, and pessimism when needed. I wish you and **Maureen** all the best. Carry on my wayward son.

My PhD started in the fusion team. Working on such a daring project with a great team created an exciting experience that unfortunately did not result in scientific output. Especially in these conditions, I am grateful to the team for sparking motivation and maintaining resolve. **John**, your systematic approach when solving problems combined with an unwavering attention to detail are probably unparalleled. Thank you for supervising the first year of my PhD and helping me to take charge of my research. During this project, there was no lack of fabrication challenges, but thanks to you, **Amrita**, it seemed there never was a lack of solutions to try either. I am very grateful for your cleanroom assistance to the fusion project, and to me personally as well. **Nicolò**, I would have loved to collaborate with you for longer, but I am nonetheless very happy you found your way back in Italy. **Luca**, it was very nice to have you join our team as a Master student, and I am very appreciative of your help characterizing the RF setup. **Jasper**, in working together, you have taught me many essential qualities for completing my PhD. Your

ability to accept setbacks and start over, incorporating the lessons learned, shows your unbelievable character and resilience. Starting the dispersive readout team (we have not really found a better name) with you and Wolfgang has been an incredible experience. I have greatly enjoyed chatting during our morning coffees, whether work-related or some different topic entirely. I wish you and **Hanna** a great time in Nijmegen.

It is great to see how the dispersive readout team has evolved and the exciting research projects that have emanated from the joint effort. First of all, **Christian P.**, it was great fun to discuss experimental results with you, as your flexible thinking allows exploring many hypotheses in rapid succession. I recognize your strive for precision and complete understanding of the underlying physics, forcing me to sharpen my occasional vague explanations. Also, I must concede that sometimes PowerPoint is a better tool for data-analysis than Microsoft paint. **Lin**, seeing you grow in your role as PhD has been wonderful, I am really looking forward to seeing your own thesis. Thanks for introducing me to hotpot. **Filip**, it's great you joined our team. I am really excited to see where your research will lead. Thank you for your sharp input in every physics discussion. **Jonne**, I am very grateful for your supervision and Friday discussions during the last leg of my PhD. Your ability to suggest experiments for investigating the samples is truly amazing. I have enjoyed your extremely knowledgeable input in my research. During the years, it was my pleasure to see several master students join the group. **Daan W.**, your persistence combined with your questioning nature resulted in resonator designs that have led to some fantastic results. **Nejc**, your presentation of scientific results is extremely impressive. It was great having you join from Utrecht and I wish you the best of luck doing your PhD there. **Michael C.**, I am very happy you decided to continue working in the team as a PhD student, and I wish you great results in doing so.

Willemijn, I feel very lucky our time in QuTech coincided and I wish to express my heartfelt gratitude for your support during those years. Thanks for turning every hike into a crazy adventure and making the trips abroad unforgettable. I am curious where life will take you, but I am convinced it is going to be amazing. **Marta**, thanks for your vital assistance making the Denver road trip extraordinary. **Lukas G.**, that Denver skiing trip was absolutely worth it. I wish you the best of luck with your next steps. **Lukas S.**, I am impressed by your industriousness, good luck with your research. **James**, thank you for your guidance during my masters and showing me the ways of an experimental PhD. I greatly enjoyed our discussions on life, the universe and nonsense. **Maja**, I must thank you once more for helping me transition from theoretical to experimental physics and thereby setting me on the path for this PhD project.

Di, I have very fond memories of you joining for the 2018 road trip, good luck finishing your thesis! **Guan**, very exciting results, good luck with the writing process. **Jaap**, thanks for the discussions about input/output theory. I would like to thank Topo-team, **Alberto**, **David van D.**, **Elvedin**, **Greg**, **Ivan**, **Jiyin**, **Nick**, **Prasanna**, **Qing**, **Tom** and **Vukan** for all your questions, interactions and explanations. I feel much gratitude towards the former members of Topo-team, forming it into what it has become, including **Arjan**, **Atilla**, **Dominique**, **Fei**, **Jakob**, **Jie**, **Nikolai**, **Ting** and **Vanessa**. **Michael W.**, **Anton**, **Joe** and **Adriaan**, being a TA for the programming course taught me many valuable lessons about teaching for which I am grateful. **Srijit**, thank you for all discussions on the different facets of the PhD program and scientific direction. I got to learn a lot from you,

especially when our opinions did not align.

I am grateful to all QuTech PhD students before me, whose collective knowledge and experience provided the proverbial shoulders to stand on. **Daniël**, practicing our presentations together was great fun and very helpful. Thanks for depositing all those nanowires and advising me on cleanroom recipes. I hope we will be discussing many more Wednesdays. **Michiel**, being your roommate for the past years has revealed your willingness to discuss any topic. Thanks for all the useful suggestions, creative points of view and taking charge trying to win a pubquiz. **Jouri**, I am very happy we explored the east coast together, good luck with your career at Microsoft. **Alex**, 6d 65 20 6e 65 69 74 68 65 72. To be sure, a debate with you is never dull, here is to many more! **Fokko**, Your work ethic is an inspiration to all. Thanks for the shared coffees, lunches, and *kerstpuzzels*. I am looking forward to seeing where your journey will take you next. **Francesco**, your personality and perseverance were great assets for the lab, I am happy our time in lab overlapped to a great extent. Good luck with your future research. **Florian**, I recognize your moral compass as exemplary, whose directions should be taken to heart at any hour of the day. **Jelmer**, it was great to discover New York together. Finally, I would like to thank **Alessandro**, **Christian D.**, **Guoji**, **Jules**, **Kian**, **Nandini**, **Niels**, **Nodar**, **Norbert**, **Ramiro**, **Sjaak**, **Stijn**, **Thijs** and **Udit** for the shared drinks, dinners and conversations. (Un)fortunately, QuTech has become too large to mention every former and current member individually, but I would like to thank you all, for creating this amazing research institute.

During my PhD, I have benefited from many discussion with my colleagues from the Microsoft lab, **Angela**, **Bas**, **Bernard**, **Chung Kay**, **Lieuwe**, **Marina**, **Pavel**, **Philippe** and **Sebastian**. **David van W.**, thank you for inviting me to the lab to find a master project all those years ago. **Victor**, your passion for smoothing out problems in the lab is a great thing to see. **Mikhail**, thank you for your invaluable programming suggestions. Also, **Gijs**, every discussion with you is bound to get passionate and intense, thanks for those! **Kevin**, thanks for all discussions regarding physics, or video games. I have appreciated our Friday meetings regardless of the contents.

The contributions of the technical support staff to the daily life in the lab cannot be overstated. Our lab would come to a grinding halt without your expertise, experience and onsite repairs. **Jason**, thank your for your work on depositing nanowires on my samples. Mapping out DC lines was definitely more enjoyable with your company. But most of all, thank you for being wherever the need in the lab is highest. **Olaf**, thank you for explaining the ins and outs of dilution refrigeration and the B1 cryostat in particular. **Nico**, I am still in awe of your machining skills. In your hands, the drilling even a single hole changes into a work of art. Thank you for the emergency brackets you were willing to make for us, they were pivotal in advancing our research. **Raymond S.**, your inclination to make every device you design blare, beep or buzz made for uniquely useful devices. Thank you for teaching me all the skills necessary to debug our measurement setup, and find ever more obscure sources of ~~noise~~ interference. **Raymond V.**, thank you for all technical discussions and devising debug strategies with me. **Marijn**, I enjoyed collaborating on the SPI-rack all that time ago. I am looking forward to collaborating with you in the future. **Matt**, your expertise on cold temperature physics and practices will be sorely missed. Thank you for sharing your knowledge and discussing random interesting stuff.

I would also like to thank **Jelle**, **Remco**, **Roy**, **Siebe** and **Spiridon** for keeping essential elements of the lab running. In particular, **Mark**, thank you for your urgency when fixing the UTS. I am grateful to the people at DEMO for providing essential lab equipment. Furthermore, I wish to express my heartfelt gratitude to the entire cleanroom staff. All results in this thesis rely on the capability to turn our designs and ideas into real devices. I would like to thank **Anja** and **Arnold** in particular for your help in getting the most stubborn patterns to write on the e-beam. Furthermore I am indebted to **Marc** and **Marco** for replacing the Au target when my need was highest. Finally, I have appreciated the support of the management staff. In particular **Chantal**, **Csilla**, **Jenny**, **Lydia**, **Marja** and **Simone**, thank you for your efficient help with forms and other practicalities.

Oscar en **Marieke** (en **Charlotte**), dank voor jullie ongeëvenaarde gastvrijheid. Alle gezamenlijke vakanties waren geweldig, net als de meeste burgers. Dat er nog maar vele mogen volgen. **Menno**, ik heb erg veel plezier gehad samen te werken in de simulatiecommissies, veel succes met de volgende stap in je carriere. **Ronnie**, dank voor je gastvrijheid. Je brede algemene kennis maken je een ideale intellectuele sparring-partner. **Rob**, jij hebt de vaardigheid om alles in een chaos te veranderen, dank voor alle onvergetelijke momenten die dat heeft opgeleverd. Ik hoop dat je samen met **Klaske** je draai weet te vinden in Nijmegen. **Richard**, je unieke invalshoeken maken iedere discussie de moeite waard. Fingers crossed voor een mooie vakantie. **Johan**, dank voor je oeverloze voorraad aan slechte muziek en slechtere films. Je toegepaste mindset is een inspiratie. **Joep**, het is geweldig met je over mooie techniek te praten. **Koen**, **Micha** en **Robin**, dank voor alle borrels en proeverijen. En natuurlijk **Arthur**, **Christiaan**, **Daan P.**, **Ian** en **Jan Willem**, dank voor al jullie gezelligheid tijdens de verschillende activiteiten. Jullie als dispuut waren een ideale afwisseling van het promotiewerk. **Miriam**, ik denk met veel plezier terug naar onze tripjes in Californië. Dank voor alles wat ik van je heb kunnen leren in de commissies en daarbuiten. **Lieselotte**, **Michael S.**, **Rosalie** en **Wouter U.**, dank voor de geboden vriendschap de afgelopen jaren, de gezellige etentjes en de borrels. Ik ben mijn vrienden uit het Lorentz tijdperk enorm dankbaar. Met jullie is het altijd makkelijk om de draad weer op te pikken en nieuwe bordspelletjes the ontdekken. Dus **Ellen**, **Elma**, **Frits**, **Jip**, **Lianne**, **Nout** en **Yuri**, dank jullie voor alle weekendjes weg en onvergetelijke vakanties.

Ten slotte wil ik graag mijn familie bedanken. Jullie hebben nu al enige jaren mijn verhalen over kwantummechanica moeten aanhoren, en daarom zou ik graag mijn ooms, tantes, neefjes en nichtjes en oma **Lot** bedanken voor de geïnteresseerde vragen danwel welkome afleiding. **Wouter**, dank je wel dat je me altijd inspireert het beste uit mezelf te halen. Ik waardeer jouw perspectief dat je meebrengt in discussies enorm. **Barbée**, dank voor de gezelligheid die jij altijd lijkt mee te brengen. Ik vind het heel erg leuk om te zien hoe jullie met **Faas** een nieuw gezin vormen. Mijn ouders, **Annelies** en **Frank**, dank dat jullie mij de vrijheid hebben gegeven om mijn eigen weg in het leven te vinden, en nog meer dank voor jullie hulp bij het uitvoeren van de resulterende plannen. Daarmee hebben jullie een belangrijke voedingsbodem voor het uitvoeren van deze promotie gecreëerd.

Damaz de Jong

CURRICULUM VITÆ

Damaz DE JONG

08-09-1991	Born in Veldhoven, The Netherlands.
2004–2010	Secondary School Lorentz Casimir Lyceum, Eindhoven, the Netherlands
2010–2013	Bachelor of Science in Mathematics (cum laude) Bachelor of Science in Physics and Astronomy (cum laude) Honours degree: Trends in experimental physics Utrecht University, Utrecht, the Netherlands *Thesis:* Specific heat of an ultracold bose gas in a harmonic trap *Supervisor:* Prof. dr. P. van der Straten
2013–2016	Master of Science in Physics & Climate Science Utrecht University, Utrecht, the Netherlands *Programme:* Theoretical physics *Thesis:* Rashba spin-orbit interaction in 1-dimensional nanowires *Supervisor:* Dr. M. Wimmer
2016	Research internship Microsoft Station Q, Santa Barbara, United States of America *Supervisor:* Dr. R. M. Lutchyn
2016–2021	PhD research Delft University of Technology, Delft, the Netherlands *Thesis:* Gate-based readout of hybrid quantum dot systems *Promotor:* Prof. dr. ir. L. P. Kouwenhoven

List of Publications

10. **D. de Jong**, C. G. Prosko, L. Han, F. K. Malinowski, Y. Liu, P. Krogstrup, L. P. Kouwenhoven, J. V. Koski, and W. Pfaff, On-demand splitting of single Cooper pairs in hybrid quantum dot systems, in preparation.

9. W. Uilhoorn, J. G. Kroll, **D. de Jong**, D. J. van Woerkom, P. Krogstrup, L. P. Kouwenhoven and M. C. Cassidy, A semiconductor nanowire Josephson laser, in preparation.

8. L. Han, M. Chan, **D. de Jong**, C. G. Prosko, G. Badawy, S. Gazibegovic, E. P. A. M. Bakkers, J. V. Koski, L. P. Kouwenhoven, F. K. Malinowski and W. Pfaff, Anomalous spin-orbit field orientations in an InSb double quantum dot characterized via dispersive gate sensing, in preparation.

7. F. K. Malinowski, L. Han, **D. de Jong**, J.-Y. Wang, C. G. Prosko, G. Badawy, S. Gazibegovic, Y. Liu, P. Krogstrup, E. P. A. M. Bakkers, L. P. Kouwenhoven and J. V. Koski, Radio-frequency C-V measurements with sub-attofarad sensitivity, submitted (arXiv:2110.03257).

6. **D. de Jong**, C. G. Prosko, D. M. A. Waardenburg, L. Han, F. K. Malinowski, P. Krogstrup, L. P. Kouwenhoven, J. V. Koski, and W. Pfaff, Rapid microwave-only characterization and readout of quantum dots using multiplexed gigahertz-frequency resonators, Physical Review Applied **16**, 014007 (2021).

5. J. van Veen, **D. de Jong**, L. Han, C. Prosko, P. Krogstrup, J. D. Watson, L. P. Kouwenhoven, and W. Pfaff, Revealing charge-tunneling processes between a quantum dot and a superconducting island through gate sensing, Physical Review B **100**, 174508 (2019).

4. **D. de Jong**, J. van Veen, L. Binci, A. Singh, P. Krogstrup, L. P. Kouwenhoven, W. Pfaff, and J. D. Watson, Rapid detection of coherent tunneling in an InAs nanowire quantum dot through dispersive gate sensing, Physical Review Applied **11**, 044061 (2019).

3. J. G. Kroll, F. Borsoi, K. L. van der Enden, W. Uilhoorn, **D. de Jong**, M. Quintero-Pérez, D. J. van Woerkom, A. Bruno, S. R. Plissard, D. Car, E. P. A. M. Bakkers, M. C. Cassidy and L. P. Kouwenhoven, Magnetic-Field-Resilient Superconducting Coplanar-Waveguide Resonators for Hybrid Circuit Quantum Electrodynamics Experiments, Physical Review Applied, **11** 064053, (2019)

2. J. G. Kroll, W. Uilhoorn, K. L. van der Enden, **D. de Jong**, K. Watanabe, T. Taniguchi, S. Goswami, M. C. Cassidy and L. P. Kouwenhoven, Magnetic field compatible circuit quantum electrodynamics with graphene Josephson junctions, Nature communications **9**, 4615 (2018).

1. P. C. Bons, R. de Haas, **D. de Jong**, A. Groot and P. van der Straten, Quantum Enhancement of the Index of Refraction in a Bose-Einstein Condensate, Physical review letters **116**, 173602 (2016).